

Lappeenrannan teknillinen yliopisto
Lappeenranta University of Technology

Jussi Sopanen

**STUDIES OF ROTOR DYNAMICS USING A MULTIBODY
SIMULATION APPROACH**

*Thesis for the degree of Doctor of Science
(Technology) to be presented with due
permission for public examination and
criticism in the auditorium 1382 at
Lappeenranta University of Technology,
Lappeenranta, Finland on the 26th of
March, 2004, at noon.*

Acta Universitatis
Lappeenrantaensis
178

- Supervisor Professor Aki Mikkola
Institute of Mechatronics and Virtual Engineering
Department of Mechanical Engineering
Lappeenranta University of Technology
- Reviewers Professor José Luis Escalona Franco
Group of Mechanical Engineering of the Department of Mechanical and
Materials Engineering
University of Seville
Spain
- Professor Rainer Nordmann
Mechatronik und Maschinenakustik
Technische Universität Darmstadt
Germany
- Opponents Professor José Luis Escalona Franco
Group of Mechanical Engineering of the Department of Mechanical and
Materials Engineering
University of Seville
Spain
- Professor Erno Keskinen
Machine Dynamics Laboratory
Tampere University of Technology
Finland

ISBN 951-764-876-6
ISSN 1456-4491

Lappeenrannan teknillinen yliopisto
Digipaino 2004

Abstract

Jussi Sopanen

STUDIES OF ROTOR DYNAMICS USING A MULTIBODY SIMULATION APPROACH

Lappeenranta, 2004

91 p.

Acta Universitatis Lappeenrantaensis 178

Diss. Lappeenranta University of Technology

ISBN 951-764-876-6

ISSN 1456-4491

The non-idealities in a rotor-bearing system may cause undesirable subcritical superharmonic resonances that occur when the rotating speed of the rotor is a fraction of the natural frequency of the system. These resonances arise partly from the non-idealities of the rotor and partly from the non-idealities of the bearings. This study introduces a novel simulation approach that can be used to study the superharmonic vibrations of rotor-bearing systems. The superharmonic vibrations of complex rotor-bearing systems can be studied in an accurate manner by combining a detailed rotor and bearing model in a multibody simulation approach.

The research looks at the theoretical background of the multibody formulations that can be used in the dynamic analysis of flexible rotors. The multibody formulations currently in use are suitable for linear deformation analysis only. However, nonlinear deformation may arise in high-speed rotor dynamics applications due to the centrifugal stiffening effect. For this reason, finite element formulations that can describe nonlinear deformation are also introduced in this work. The description of the elastic forces in the absolute nodal coordinate formulation is studied and improved. A ball bearing model that includes localized and distributed defects is developed in this study. This bearing model could be used in rotor dynamics or multibody code as an interface element between the rotor and the supporting structure. The model includes descriptions of the nonlinear Hertzian contact deformation and the elastohydrodynamic fluid film.

The simulation approaches and models developed here are applied in the analysis of two example rotor-bearing systems. The first example is an electric motor supported by two ball bearings and the second is a roller test rig that consists of the tube roll of a paper machine supported by a hard-bearing-type balancing machine. The simulation results are compared to the results available in literature as well as to those obtained by measuring the existing structure. In both practical examples, the comparison shows that the simulation model is capable of predicting the realistic responses of a rotor system. The simulation approaches developed in this work can be used in the analysis of the superharmonic vibrations of general rotor-bearing systems.

Keywords: Rotor dynamics, flexible multibody systems, ball bearing, tube roll

UDC 621.8 : 004.942 : 534.1

Acknowledgements

This research work was carried out between 1999 and 2004 in the Institute of Mechatronics and Virtual Engineering at Lappeenranta University of Technology. The work was done as a part of the PyöriVÄRE project that was financed by the National Technology Agency of Finland (TEKES). The research related to the Absolute Nodal Coordinate Formulation was partly financed by the Academy of Finland.

I would like to thank all the people who have helped me to complete this research. In particular, I wish to thank the supervisor of this thesis, professor Aki Mikkola, for his valuable advice and the interest he has taken in my research work. I would also like to thank the members of the Institute of Mechatronics and Virtual Engineering for their help.

I wish to thank Dr. Ahmed Shabana for the opportunity to work in his research group at the University of Illinois at Chicago. I also thank Mr. Esa Porkka at Helsinki University of Technology for carrying out the experimental verification measurements used in this work. I am grateful to Mr. Amir Hassan for assisting me in proof-reading this thesis.

I would like to thank the reviewers of the thesis, Professor José Escalona from University of Seville, Spain, and Professor Rainer Nordmann from Technische Universität Darmstadt, Germany, for their valuable comments.

I would like to thank my parents and siblings for the support and encouragement they gave me during this work.

I gratefully acknowledge the financial support provided by Emil Aaltosen säätiö, Jenny ja Antti Wihurin rahasto, Tekniikan edistämissäätiö, Suomen kulttuurirahasto, Lahja ja Lauri Hotisen rahasto and Walter Ahströmin säätiö.

I dedicate this thesis to my wife Mia and to our son Jesse. You have given me the strength to complete this research.

Jussi Sopanen
February, 2004
Lappeenranta, Finland

CONTENTS

1	INTRODUCTION	15
1.1	Scope of the Work and Outline of the Dissertation	17
1.2	Contribution of the Dissertation.....	18
2	ROTOR DYNAMICS AND FLEXIBLE MULTIBODY SYSTEMS.....	19
2.1	Finite Segments Approach.....	19
2.1.1	Generalized Coordinates and Kinematics of a Rigid Body.....	19
2.1.2	Connector Forces.....	20
2.1.3	Equations of Motion.....	21
2.2	Floating Frame of Reference Formulation.....	23
2.2.1	The Kinematics of a Flexible Body.....	23
2.2.2	Solving the Shape Matrix Using Finite Element Method	24
2.2.3	The System's Equations of Motion.....	27
2.3	Large Deformation Formulations in Multibody Simulation.....	31
2.3.1	Large Rotation Vector Formulation	32
2.3.2	Absolute Nodal Coordinate Formulation	33
3	MODELING OF BALL BEARINGS	41
3.1	Modeling Assumptions and Contact Calculation	43
3.2	Ball Bearing Kinematics	46
3.3	Elastic Deformation in Ball Bearings	48
3.4	Ball Bearing Damping	51
3.5	Non-Idealities.....	52
3.5.1	Waviness of the Bearing Rings	53
3.5.2	Localized Defects	53
3.6	Summary	55
4	CASE I: ELECTRIC MOTOR SUPPORTED WITH BALL BEARINGS.....	56
4.1	Studied Structure.....	56
4.2	Simulation Results	58
4.2.1	Effect of Diametral Clearance	58
4.2.2	Waviness of the Rings.....	60
4.2.3	Localized Defects	65
4.3	Summary	67
5	CASE II: SUBCRITICAL VIBRATIONS OF A TUBE ROLL	68
5.1	Studied Structure.....	68
5.2	Simulation Model.....	69
5.2.1	Flexible Tube Roll.....	69
5.2.2	Roll Support.....	72
5.2.3	Interface between the Roll and Support	72
5.2.4	Comparison with Experimental Modal Analysis and Optimization.....	75
5.3	Simulation Results	76
5.3.1	Sensitivity Analysis	76
5.3.2	Effect of Inertia Modeling of Roll.....	82
6	CONCLUSIONS.....	83
	REFERENCES.....	85

NOMENCLATURE

Abbreviations

ADAMS	Automatic Dynamic Analysis of Mechanical Systems
FFT	Fast Fourier Transform
VC	varying compliance frequency
X	rotation speed

Symbols

a_e	semimajor axis of the contact ellipse
a_0, \dots, a_7	polynomial coefficients
A	area of the beam cross-section
A_m, ϕ_m	amplitude and phase angle of the m th order waviness
\mathbf{A}	rotation matrix between the local coordinate and the global coordinate system
\mathbf{A}_ψ	transformation matrices due to centerline rotation
\mathbf{A}_γ	transformation matrices due to shear angle
b_c	semiwidth of the contact
b_e	semiminor axis of the contact ellipse
b_0, \dots, b_7	polynomial coefficients
c_b	bearing damping coefficient
c_c^{\max}	maximum damping constant
c_d	diametral clearance of the bearing
c_k	amplitude of the k th harmonics waviness component
c_0, \dots, c_7	polynomial coefficients
\mathbf{C}	vector of kinematical constraint equations
\mathbf{C}_q	constraint Jacobian matrix
d	ball diameter
d_i	distance between the race surfaces along the line of contact at ball i
d_1	bearing bore diameter
d_c	penetration, when the maximum damping constant c_c^{\max} is achieved
d_m	bearing pitch diameter
\mathbf{d}_b	vector of relative translational displacements of the body i with respect to body j
D	Outer diameter of the ball bearing
D_1, D_2	diameters of the cylinders
\mathbf{D}	displacement gradient
\mathbf{D}_b	damping matrix of the beam element
\mathbf{D}_d	damping matrix in the floating frame of reference formulation
\mathbf{D}_p	modal damping matrix
\mathbf{e}	vector of the nodal coordinates
\mathbf{e}_0	vector of the nodal coordinates in the initial configuration
e_i^r, e_i^a	radial and axial eccentricity of the ball i
e_c	exponent of the force-deflection relationship
E	Young's modulus
E'	effective modulus of elasticity
f_{bpir}	inner ring defect frequency
f_{bpor}	outer ring defect frequency

f_s	rotation speed of the cage
\dot{f}_s	rotation speed of the shaft
\mathbf{f}_g	gravitational force vector
F	contact force
F_{\max}	maximum contact force
F_{nominal}	nominal bearing force
F_{nr}	total force of the needle roller bearing
\mathbf{F}	force vector
F_x, F_y, F_z	bearing force components
g	independent variable in <i>STEP</i> function
g_0, g_1	starting and ending values of the <i>STEP</i> function
G	shear modulus
$\bar{\mathbf{G}}$	matrix that defines the relationship between angular velocities in a local body frame and time derivatives of the orientation coordinates
\bar{G}	dimensionless material parameter
h_0	central film thickness, initial value of the function
h_1	final value of the function
h_{defect}	height of the localized defect
i, j, k	integer coefficients
I	node I
$I_{xx}, I_{yy}, I_{zz}, I_{yz}$	second moments of area of the beam cross-section
\mathbf{I}	identity matrix
$\mathbf{I}^1, \dots, \mathbf{I}^9$	inertia invariants
$\bar{\mathbf{I}}_{\theta\theta}^i$	inertia tensor of the body i
$\bar{\mathbf{I}}_{\theta p}$	inertia shape integral
J	node J
k_e	ellipticity parameter
k_{lin}	linearized bearing stiffness coefficient
k_s	shear correction factor
k_c	stiffness coefficient
k_{needle}	stiffness coefficient for the contact between one needle and both inner and outer race of the bearing
K_c	contact stiffness coefficient
K_c^{tot}	total stiffness coefficient
\mathbf{K}	stiffness matrix
\mathbf{K}_b	stiffness matrix of the Timoshenko beam element
\mathbf{K}_s	stiffness matrix obtained from the finite element model of the structure
l	length of the beam element in the initial configuration
l_r	length of the needle
\mathbf{l}	vector from body j to body i
L	Lagrangian
L_1	length of the cylinder
m_i	mass of node i
m_h	mass of the bearing housing
\mathbf{m}	submatrix of the mass matrix
M	number of modes
M_z	applied external moment
\mathbf{M}	mass matrix
\mathbf{M}_s	mass matrix obtained from the finite element model of the structure

n	integer coefficient
n_f	number of mode shapes
n_m	number of retained mode shapes
\mathbf{n}_k	k th eigenvector calculated from Craig-Bampton representation of the system
N	number of nodes
\mathbf{N}	orthogonal mode shape matrix
L_{defect}	length of the localized defect
p	pressure
\mathbf{p}	vector of modal coordinates
\mathbf{q}_r	vector of generalized coordinates of a rigid body
\mathbf{q}	vector of generalized coordinates of a flexible body
Q_y, Q_z	first moments of area of the beam cross-section
\mathbf{Q}_e	vector of generalized forces
\mathbf{Q}_E	vector of generalized forces including conservative and non-conservative forces.
\mathbf{Q}_f	vector of external generalized forces
\mathbf{Q}_v	vector of quadratic velocity inertia terms
\mathbf{Q}_c	vector that arises by differentiating the constraint equations twice with respect to time
r	race groove radius <i>or</i> ball radius
\mathbf{r}	position vector in a global coordinate system
\mathbf{R}	position vector of the origin of a local coordinate system
R	curvature sum
R_d	curvature difference
R_x	effective radius of curvature in principal x plane
R_y	effective radius of curvature in principal y plane
R_{in}, R_{out}	inner and outer raceway radius
$R(\theta)$	roundness profile of the bearing ring
R_r	race conformity
r_{in}, r_{out}	inner and outer groove radius
S_1, \dots, S_8	shape functions
\mathbf{S}	element shape function matrix
$\bar{\mathbf{S}}_i, \bar{\mathbf{S}}$	inertia shape integrals
t_i	measured shell thickness at node i
t'_i	two-fold shell thickness at node i
T_x, T_y, T_z	bearing torque components
T	kinetic energy
\mathbf{T}	torque vector
u	displacement of point P of the beam in the direction of the X coordinate
u_0	displacement of the beam centerline in the direction of the X coordinate
$\bar{\mathbf{u}}$	position vector of a particle in the local coordinate system
\mathbf{u}	position vector of a particle in the global coordinate system
\mathbf{u}_0	displacement of the beam centerline
$\bar{\mathbf{u}}_0$	position vector which defines the undeformed position of the particle in the local coordinate system
$\bar{\mathbf{u}}_f$	position vector which defines the deformation of the particle in the local coordinate system

U_{in}, U_{out}	surface velocities in ball-inner-race and ball-outer-race contacts
U	strain energy <i>or</i> mean of the surface velocities
\bar{U}	dimensionless speed parameter
UB_1, UB_2	unbalance masses
v	displacement of point P of the beam in the direction of the Y coordinate
v_0	displacement of the beam centerline in the direction of the Y coordinate
V	volume of the element <i>or</i> potential energy
\bar{W}	virtual work
\bar{W}	dimensionless load parameter
x	local coordinate
x_{c0}	contact distance
x_c	distance between contacting bodies
\mathbf{x}	vector of the local element coordinates
y	local coordinate
\mathbf{y}_P	vector defining the beam cross-section
z	local coordinate <i>or</i> number of balls <i>or</i> number of needles
z_F	Stribeck's constant
X	global coordinate
\mathbf{X}	vector of the global coordinates
Y	global coordinate
Z	global coordinate

Greek Letters

α	temperature dependent pressure-viscosity coefficient <i>or</i> attitude angle of the roll
α_1, α_2	angles describing the size of the bearing defect
Λ	rotation matrix
β_i	attitude angle (azimuth angle) of the ball i
ε_{xx}	normal strain in x -direction
ε_{yy}	normal strain in y -direction
ε_{xy}	normal strain in xy -plane
$\boldsymbol{\varepsilon}_m$	Lagrangian strain tensor
δ_0	deflection between the ball and the race
δ_i^{tot}	total elastic deformation of the ball i
δ_r	radial displacement between the inner and the outer race
γ	shear angle
γ_x, γ_y	misalignments between the inner and outer race
δ	physical degrees of freedom
Δ_i^{total}	total deformation of the ball i with non-idealities
Δ_{defect}	deformation caused by the defect
ϕ_i	contact angle of the ball i
ϕ_k	phase angle of the k^{th} harmonics
ϕ_{defect}	position angle of the localized defect
φ	auxiliary angle
$\boldsymbol{\Phi}_k$	k th eigenvector
ψ	rotation angle of the beam centerline

Ψ	rotation vector
Φ	shape matrix
θ	angular coordinate of the bearing ring
Θ	vector of generalized orientation coordinates
Θ_b	vector of relative rotational displacements of the body i with respect to body j
Γ	translational strain measure
κ	rotational strain measure
λ	vector of Lagrange multipliers
η	viscosity of the lubricant
ν	Poisson's ratio
ν_0	kinematic viscosity of the lubricant
ω	angular velocity of the bearing ring
ω_k^2	k th eigenvalue
$\bar{\omega}$	angular velocity vector in a local coordinate system
ω	vector that can be obtained by employing the rotational vector Ψ
ρ	material density
ξ	elliptic integral of the first kind <i>or</i> non-dimensional quantity
η	non-dimensional quantity
ζ	elliptic integral of the second kind <i>or</i> non-dimensional quantity

Sub- and superscripts

B	boundary degrees of freedom
C	constraint i.e. static correction modes.
I	internal degrees of freedom
in	inner ring
out	outer ring
i	ball i <i>or</i> body i <i>or</i> node i
a	solid a
b	solid b
f	elastic coordinates
N	fixed interface normal modes
R	translational coordinates
θ	rotational coordinates
p	modal coordinates
P	particle P
t	differentiation with respect time
\mathbf{q}	partial derivatives with respect to generalized coordinates
x	partial derivative with respect x
y	partial derivative with respect y

1 INTRODUCTION

A complete rotating machine consists of several components, such as the rotor, bearings, rotor support and drive system, as shown in Figure 1.1. All these components influence the dynamical behavior of the system. However, traditionally, different components are studied individually, and thus, the interactions between various elements are not taken into account. In addition, due to manufacturing tolerances, rotor systems include a number of non-idealities, such as the uneven mass and stiffness distribution of the rotor and the waviness of the bearing rings. These kinds of non-idealities are harmful, since they can cause superharmonic resonances in the rotor system. In this case, the natural vibration mode of the rotor is excited when the rotation speed is a fraction of the natural frequency of the system. Superharmonic resonances are sometimes referred to as subcritical resonances, since they occur at the subcritical rotational speed. In some applications, such as in paper machines, $1/2$, $1/3$ and $1/4$ subcritical resonances are of practical significance, since they may be within the operating speed range and can influence the quality of the final product. Furthermore, the subcritical resonance condition can lead to excessive wear or even irreparable damage. In order to study the superharmonic responses of the rotor system, the impulses caused by the bearings and non-idealities of rotor must be taken simultaneously into consideration. In practice, this can be accomplished by studying physical prototypes or through the use of computer simulations. When the computer simulation approach is used, the simulation model must be detailed enough in order to capture the non-idealities of the rotor and bearings as well as the coupling between these elements.

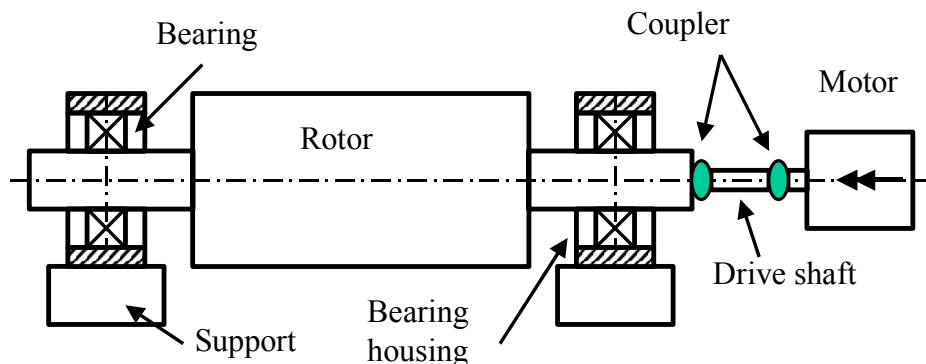


Figure 1.1 The components of a rotating machine.

A number of books oriented towards rotor dynamics provide methods for analyzing rotor-bearing systems [1-4]. The purpose of these methods is the calculation of the critical speeds of a rotor, the stability regions near or between the critical speeds and the steady state responses due to, for example, unbalance excitation. Fundamental rotor dynamics phenomena, such as gyroscopic effects, internal resonance and the dependence of critical speeds on the rotational frequency, can be analyzed using the Jeffcott rotor model, as is done, for example, in [5]. The Jeffcott rotor includes a disk carried by massless flexible shaft that is supported by linear bearings. Simple rotor-bearing models can be studied analytically employing partial differential equations. More complex systems can be analyzed using the transfer matrix method or the finite element method, which leads to a matrix representation of the rotor system. In the transfer matrix method, the rotor is divided into rigid shaft segments that are coupled using transfer matrices [1]. The finite element formulation has been successfully applied to rotor dynamics analysis, as for example, in

References [6, 7]. Using the finite element formulation, the flexibility of rotors can be described in an accurate manner. Other important issues such as rotary inertia, gyroscopic moments, the shear deformation of the shaft and the asymmetry of the rotor and the bearings can be straightforwardly taken into account when using the finite element approach. The solution of steady state responses is usually performed in a frequency domain, which requires the linearization of the nonlinear bearing components. For transient analysis, the finite element equations of motion are solved directly or by employing modal synthesis methods [3, 8, 9] that can be used to decrease the degrees of freedom of the system.

It is important to identify the critical speeds and stability regions of the rotor at an early design phase; however, only few studies have focused on the superharmonic vibrations of rotor systems. A well-known twice-running-speed (2X) response arises from the rotor asymmetry in horizontally mounted rotors. In this case, the bending stiffness variation, together with gravity, excites the symmetrical natural modes of the rotor. This phenomenon is discussed, for example, in References [1-3, 7, 10]. The superharmonic or subharmonic resonance conditions that arise from the non-idealities of the bearings are rarely studied. This may be caused by the fact that nonlinear bearings are complicated to analyze when the finite element approach or the transfer matrix approach is used. Childs [11] included bearing ellipticity in the analysis and showed that the ellipticity of the bearing leads to a twice-running-speed (2X) response over a broad running speed range. Ehrich [12] studied a rotor that operates eccentrically within the bearing clearance and in local contact with the stator. Ehrich concluded that a rotor system that is excited by unbalance at a subcritical speed, which is a fraction of the natural frequency, will respond by bouncing at its natural frequency. Ehrich referred to this phenomenon as subcritical superharmonic response, which is related to the more studied supercritical subharmonic response [13, 14]. In supercritical subharmonic resonance, the system will respond when its natural frequency is a fraction of the rotating speed. Childs [13] explained the fractional frequency oscillations of one half and one third of the Jeffcott rotor by the nonsymmetric clearance effects of the bearings.

In order to accurately study the superharmonic vibrations caused by the bearings, a nonlinear transient analysis that uses detailed simulation models must be used. It is only recently that the interactions of the rotor and the bearings have been studied [15, 16]. El-Saeidy [15] studied rotating shafts subjected to an axially moving load using the finite element formulation. The shafts were supported by nonlinear rolling element bearings. Hu *et al.* [16] studied crank shaft dynamics using substructures of the shaft and support; the substructures were connected using nonlinear springs that describe the journal bearings.

Multibody simulation provides a novel approach for the analysis of rotor dynamics. Multibody simulation uses a general methodology that can describe the machine members that undergo large relative translational and rotational displacements. In the multibody approach, numerical methods are used to solve the nonlinear equations of motion with respect to time. The obtained transient results can be post-processed in order to study the superharmonic responses of the rotor system in the frequency domain. In multibody simulation, the mechanical system under consideration is modeled in the form of discrete bodies; these bodies can be coupled together using forces and/or constraint equations. The forces acting on the discrete bodies can be nonlinear functions of the system parameters. This makes it possible to describe the bearings as interface force elements applied between the rotor and the supporting structure. In order to describe the bearings as nonlinear forces, analytical bearing models, which can be found in the bearing literature, must be employed. Typically, analytical bearing models need to be modified in order to make them suitable for the multibody description of a non-ideal bearing component. Using the multibody

simulation approach, the interaction between the rolling element bearings and the rotor can be studied. It is important to consider the coupling between the bearings and the rotor, for example, in electric motors and paper machines. Furthermore, several other modeling issues, such as the flexibility of the rotor, can be taken into account in a straightforward manner.

Multibody simulation is not often utilized in analysis of rotor dynamics applications. Brown and Shabana [17] applied flexible multibody formulations to rotating shaft problems. Al-Bedoor [18] studied coupled torsional and lateral vibrations of unbalanced rotors. The equations of motion were obtained using Lagrangian dynamics, and multibody approach was used to describe orientations of shafts. The results showed inertial coupling between the lateral and torsion vibration responses. Keskiniva [19] presented a semidefinite modal coordinate approach for balancing of flexible rotors. In this method, the kinematics of the rotor is described using vibration modes of an unconstrained rotor. Bearings were modeled using interface elements, which can be linear or nonlinear. However, in Keskiniva's approach, the rigid body motion and elastic deformation of the rotor were uncoupled. This approach should be used with care in three-dimensional cases, since, in some high-speed and lightweight applications, the coupling terms between the reference motion and deformation play an important role [20, 21].

1.1 Scope of the Work and Outline of the Dissertation

In this work, the multibody simulation approach is used for the dynamic analysis of rotor-bearing applications. The work focuses on the superharmonic vibrations that are caused by the dynamical interaction between the flexible rotor and non-ideal bearings. Thus, not all important issues in rotor dynamics are covered. Aspects, such as rotor balancing or internal resonances, are not addressed here. In order to study superharmonic vibrations, the bearings and the rotor must be described in detail. This work concentrates on the detailed modeling of rolling element bearings, particularly on modeling of ball bearings.

Chapter 2 discusses the flexible multibody formulations that can be used in rotor dynamics analysis. These formulations include methods that can describe linear deformations and large nonlinear reference motions of the rotor. Nonlinear deformation may occur in a high-speed rotor system due to the centrifugal stiffening effect. For this reason, formulations that can describe nonlinear deformation are also described in Chapter 2.

The ball bearing model, which includes descriptions for localized and distributed defects, is presented in Chapter 3. The model has six degrees of freedom and can be used in general rotor dynamics or multibody computer code as an interface element between the rotor and the housing. In Chapter 4, an electric motor supported by ball bearings is analyzed. The simulated results are compared with the reported measurements and analytical results available in literature.

In Chapter 5, the roll of a paper machine on a balancing machine support is modeled and analyzed using the multibody simulation approach. The modeling aspects and techniques used in the roll model are discussed. The simulated results are compared to measured results obtained from the existing roll test rig. A sensitivity analysis is performed to study the effect of the input data on the twice-running-speed superharmonic response. Chapter 6 includes the summation of the work and the most important results.

1.2 Contribution of the Dissertation

The following original contributions are developed in this dissertation:

1. This study introduces a novel simulation approach that can be used to study the superharmonic vibrations of rotor-bearing systems. As shown in this study, the superharmonic vibrations of complex rotor-bearing systems can be studied accurately by combining a detailed rotor model and a bearing model in the multibody simulation approach. Superharmonic vibrations arise partly from the non-idealities of the rotor and partly from the non-idealities of the bearings.
2. A ball bearing model, which includes localized and distributed defects, is developed in this study. This bearing model could be used in rotor dynamics or multibody code as an interface element between the rotor and the supporting structure. The model includes descriptions of nonlinear Hertzian contact deformation and elastohydrodynamic fluid film. The geometry, material properties and diametral clearance of the bearing are given as the input to the proposed model. The bearing force and torque components are calculated from the relative displacements and velocities between the bearing rings.
3. This study improves the description of elastic forces in the absolute nodal coordinate formulation. The absolute nodal coordinate formulation is a very promising method for the analysis of nonlinear deformable bodies in multibody systems. The formulation can be used for the analysis of high-speed rotor applications.

2 ROTOR DYNAMICS AND FLEXIBLE MULTIBODY SYSTEMS

Traditional research into rotor dynamics is concerned mainly with the stability and natural frequencies of rotor systems [1-3]. As demonstrated by Brown and Shabana [17], the equations of motion in traditional rotor dynamics are usually derived using simplifying assumptions, which limit the use of these equations in more general cases. In traditional rotor dynamics equations, the angular velocity of the rotor is typically assumed to be constant. Furthermore, traditional formulations do not take into account the vibration that results from bearing clearance, bearing ring waviness or bearing defects.

A more general approach for rotor dynamics can be obtained using the multibody simulation approach. This approach does not suffer from the above-mentioned limitations, which makes it possible to analyze complete systems that include flexible rotors, bearings and the drive system. In the multibody approach, the flexibility of a body is usually described using the finite element method. It is crucial for success that finite element formulation be able to accurately describe the inertia properties of a body as well as an arbitrary rigid body motion.

Multibody formulations that can be used in the modeling and analysis of flexible rotors are reviewed in the following sections. In Section 2.1, the finite segments approach is briefly reviewed. This approach employs equations of rigid-body multibody systems. The treatment of large rotations in a general three-dimensional analysis is often a source of problems when applying finite element formulations in multibody simulation. Several methods, which can describe an arbitrary rigid body motion including finite rotations, have been developed for the analysis of flexible multibody systems. In the floating frame of reference formulation described in Section 2.2, a large reference motion is described using a reference frame, and the deformation is described relative to this frame. One important property of this method is that the number of variables that describe the deformation can be reduced using component mode synthesis. This, in turn, reduces the computational effort significantly without a noteworthy loss in accuracy. Usually, linear modes are used in the component mode synthesis and, as a result, the deformations of a body are assumed to be linear. In some high-speed rotor dynamics applications, the assumption of linear deformations is not valid due to the centrifugal stiffening effect. For this reason, two nonlinear finite element formulations are discussed in Section 2.3. In the large rotation vector formulation and the absolute nodal coordinate formulation, the configuration of the finite element is described directly in a global inertial frame. These methods include all the geometrically nonlinear terms and, therefore, can be used in the nonlinear analysis of high-speed rotors. It is important to point out that nonlinear modes can be used in the floating frame of reference formulation to model nonlinear deformations, as shown in [22].

2.1 Finite Segments Approach

In the finite segments approach, a flexible body is divided into discrete mass points that are connected to each other by spring-damper elements. The mass points are treated as rigid bodies, in which case the equations of motion can be obtained by employing multibody formulation.

2.1.1 Generalized Coordinates and Kinematics of a Rigid Body

The motion of each mass point of the system is described using generalized coordinates. For body i , the vector of generalized coordinates, \mathbf{q}_r^i , can be written as [23]

$$\mathbf{q}_r^i = \begin{bmatrix} \mathbf{R}^{iT} & \boldsymbol{\theta}^{iT} \end{bmatrix}^T, \quad (2.1)$$

where \mathbf{R}^i is the position vector of the origin of a local coordinate system of the body and $\boldsymbol{\theta}^i$ is the vector of generalized orientation coordinates. The orientation of the body can be described using, for example, Euler angles, Rodriguez parameters or Euler parameters. By using generalized coordinates, the global position of an arbitrary particle, P , on body i can be expressed in the following form:

$$\mathbf{r}^i = \mathbf{R}^i + \mathbf{A}^i \bar{\mathbf{u}}^i, \quad (2.2)$$

where \mathbf{A}^i is a rotation matrix that describes the rotation of the local coordinate system with respect to the global coordinate system and $\bar{\mathbf{u}}^i$ is the position vector of a particle in the local coordinate system. The velocity of an arbitrary particle can be obtained by differentiating Equation (2.2) with respect to time as follows:

$$\dot{\mathbf{r}}^i = \dot{\mathbf{R}}^i + \dot{\mathbf{A}}^i \bar{\mathbf{u}}^i, \quad (2.3)$$

where $\dot{\mathbf{A}}^i \bar{\mathbf{u}}^i$ can be written as

$$\dot{\mathbf{A}}^i \bar{\mathbf{u}}^i = -\mathbf{A}^i \tilde{\mathbf{u}}^i \bar{\mathbf{G}}^i \dot{\boldsymbol{\theta}}^i, \quad (2.4)$$

where $\tilde{\mathbf{u}}^i$ is the skew symmetric matrix of vector $\bar{\mathbf{u}}^i$. Matrix $\bar{\mathbf{G}}^i$ defines the relationship between the angular velocities in the local body frame and the time derivatives of the orientation coordinates as follows:

$$\bar{\boldsymbol{\omega}}^i = \bar{\mathbf{G}}^i \dot{\boldsymbol{\theta}}^i \quad (2.5)$$

It is important to point out that the expressions of the rotation matrix, \mathbf{A}^i , and matrix $\bar{\mathbf{G}}^i$ depend on the selected generalized orientation coordinates.

2.1.2 Connector Forces

In the finite segments approach, the connector forces, i.e. spring forces, can be calculated from the relative displacements and velocities of the adjoined mass points. For beam structures, the forces can be formulated using the Timoshenko beam theory. The local forces, $\bar{\mathbf{F}}^{ij}$, and moments, $\bar{\mathbf{T}}^{ij}$, acting on body i due to interaction with body j can be calculated as follows:

$$\begin{bmatrix} \bar{\mathbf{F}}^{ij} \\ \bar{\mathbf{T}}^{ij} \end{bmatrix} = -\mathbf{K}_b \begin{bmatrix} \mathbf{d}_b \\ \boldsymbol{\theta}_b \end{bmatrix} - \mathbf{D}_b \begin{bmatrix} \dot{\mathbf{d}}_b \\ \dot{\boldsymbol{\theta}}_b \end{bmatrix}, \quad (2.6)$$

where \mathbf{d}_b and $\boldsymbol{\theta}_b$ are the relative translational and rotational displacements of body i with respect to body j and \mathbf{K}_b is the stiffness matrix that can be found in Appendix A. In Equation (2.6), \mathbf{D}_b is the damping matrix that can be approximated by multiplying the stiffness matrix with a damping ratio. The local forces acting on body j due to interaction with body i can be written as [24]

$$\bar{\mathbf{F}}^{ji} = -\bar{\mathbf{F}}^{ij} \quad (2.7)$$

$$\bar{\mathbf{T}}^{ji} = -\bar{\mathbf{T}}^{ij} - \mathbf{1} \times \bar{\mathbf{F}}^{ij}, \quad (2.8)$$

where $\mathbf{1}$ is the vector from body j to body i .

The externally applied forces must be defined as generalized forces that affect the system's generalized coordinates. Using the principle of the virtual work, the generalized forces caused by locally applied forces and moments can be expressed as [23]

$$\left(\mathbf{Q}_e\right)_R = \mathbf{A}^i \bar{\mathbf{F}}^{ij} \quad (2.9)$$

$$\left(\mathbf{Q}_e\right)_\theta = \left(\mathbf{A}^i \bar{\mathbf{G}}^i\right)^T \left(\mathbf{A}^i \tilde{\mathbf{u}}_p^i \mathbf{A}^i \bar{\mathbf{F}}^{ij} + \mathbf{A}^i \bar{\mathbf{T}}^{ij}\right), \quad (2.10)$$

where $\left(\mathbf{Q}_e\right)_R$ and $\left(\mathbf{Q}_e\right)_\theta$ are the vectors of the generalized forces associated with the translational and rotational generalized coordinates of body i , respectively. Vector $\tilde{\mathbf{u}}_p^i$ defines the working point of the force in the local coordinate system.

2.1.3 Equations of Motion

The dynamics of a multibody system can be calculated using the Lagrangian method. The Lagrangian method relies upon Lagrange's equations that can be derived using the concepts of generalized coordinates, virtual work and generalized forces while employing D'Alembert's principle. By using Lagrange's equation and an augmented formulation for the kinematic constraints, the system equation of motion can be written as follows [21]

$$\mathbf{M}\ddot{\mathbf{q}} + \mathbf{C}_q^T \boldsymbol{\lambda} = \mathbf{Q}_e + \mathbf{Q}_v, \quad (2.11)$$

where \mathbf{M} is the mass matrix, \mathbf{C}_q the constraint Jacobian matrix, $\boldsymbol{\lambda}$ the vector of Lagrange multipliers, \mathbf{Q}_e the vector of generalized forces and \mathbf{Q}_v the vector of the quadratic velocity inertia forces. The mass matrix of body i can be obtained from the expression of the kinetic energy as follows:

$$\mathbf{T}^i = \frac{1}{2} \int_{V^i} \rho^i \dot{\mathbf{r}}^{iT} \dot{\mathbf{r}}^i dV^i = \frac{1}{2} \dot{\mathbf{q}}_r^{iT} \mathbf{M}^i \dot{\mathbf{q}}_r^i, \quad (2.12)$$

where V^i is the volume of body i . The mass matrix, \mathbf{M}^i , can be written as follows:

$$\mathbf{M}^i = \begin{bmatrix} \mathbf{m}_{RR}^i & \mathbf{m}_{R\theta}^i \\ \text{symm.} & \mathbf{m}_{\theta\theta}^i \end{bmatrix}. \quad (2.13)$$

The submatrices can be written as follows

$$\mathbf{m}_{RR}^i = \int_{V^i} \rho^i \mathbf{1} dV^i = m^i \mathbf{1} \quad (2.14)$$

$$\mathbf{m}_{R\theta}^i = -\mathbf{A}^i \left[\int_{V^i} \rho^i \tilde{\mathbf{u}}^i dV^i \right] \bar{\mathbf{G}}^i \quad (2.15)$$

$$\mathbf{m}_{\theta\theta}^i = \int_{V^i} \rho^i \bar{\mathbf{G}}^{iT} \tilde{\mathbf{u}}^i \tilde{\mathbf{u}}^i \bar{\mathbf{G}}^i dV^i = \bar{\mathbf{G}}^{iT} \bar{\mathbf{I}}_{\theta\theta}^i \bar{\mathbf{G}}^i, \quad (2.16)$$

where \mathbf{I} is a 3×3 identity matrix and $\bar{\mathbf{I}}_{\theta\theta}^i$ the inertia tensor of the body i . If the local coordinate system of the body is attached to the center of mass of the same body, matrix $\mathbf{m}_{R\theta}^i$ is a null matrix.

The kinematical constraint equations are functions of the system's generalized coordinates and can be expressed as follows:

$$\mathbf{C}(\mathbf{q}_r, t) = \mathbf{0} \quad (2.17)$$

The constraint Jacobian matrix can be obtained by differentiating the constraint equations with respect to the generalized coordinates as follows:

$$\mathbf{C}_q = \frac{\partial \mathbf{C}(\mathbf{q}_r, t)}{\partial \mathbf{q}_r} \quad (2.18)$$

The vector of quadratic velocity inertia forces, which contains the terms that are quadratic in the velocities, such as the gyroscopic and Coriolis terms, can be expressed as follows [23]:

$$\mathbf{Q}_v^i = \left[(\mathbf{Q}_v^i)_R \quad (\mathbf{Q}_v^i)_\theta \right]^T, \quad (2.19)$$

where vectors $(\mathbf{Q}_v^i)_R$ and $(\mathbf{Q}_v^i)_\theta$ can be written as

$$(\mathbf{Q}_v^i)_R = -\mathbf{A}^i (\tilde{\boldsymbol{\omega}}^i)^2 \left[\int_{V^i} \rho^i \tilde{\mathbf{u}}^i dV^i \right] + \mathbf{A}^i \left[\int_{V^i} \rho^i \tilde{\mathbf{u}}^i dV^i \right] \dot{\mathbf{G}}^i \dot{\boldsymbol{\theta}}^i \quad (2.20)$$

$$(\mathbf{Q}_v^i)_\theta = -\bar{\mathbf{G}}^{iT} \left[\tilde{\boldsymbol{\omega}}^i \bar{\mathbf{I}}_{\theta\theta}^i \tilde{\boldsymbol{\omega}}^i + \bar{\mathbf{I}}_{\theta\theta}^i \dot{\mathbf{G}}^i \dot{\boldsymbol{\theta}}^i \right] \quad (2.21)$$

Equation (2.11) represents the dynamic equations of the constrained system. These differential algebraic equations (DAE) are nonlinear. For this reason, Equation (2.11) is often solved through the use of the numerical integration approach of ordinary differential equations (ODE). To accomplish this, the constraint equations are differentiated twice with respect to time as follows [21]:

$$\mathbf{C}_q \ddot{\mathbf{q}}_r = -\mathbf{C}_{tt} - (\mathbf{C}_q \dot{\mathbf{q}}_r)_q \dot{\mathbf{q}}_r - 2\mathbf{C}_{qt} \dot{\mathbf{q}}_r \quad (2.22)$$

By defining the vector \mathbf{Q}_c as

$$\mathbf{Q}_c = -\mathbf{C}_{tt} - (\mathbf{C}_q \dot{\mathbf{q}}_r)_q \dot{\mathbf{q}}_r - 2\mathbf{C}_{qt} \dot{\mathbf{q}}_r, \quad (2.23)$$

Equations (2.11) and (2.23) can be combined into one matrix equation as

$$\begin{bmatrix} \mathbf{M} & \mathbf{C}_q^T \\ \mathbf{C}_q & \mathbf{0} \end{bmatrix} \begin{bmatrix} \ddot{\mathbf{q}}_r \\ \boldsymbol{\lambda} \end{bmatrix} = \begin{bmatrix} \mathbf{Q}_e + \mathbf{Q}_v \\ \mathbf{Q}_c \end{bmatrix} \quad (2.24)$$

The acceleration vector and the vector of Lagrange multipliers can then be solved from Equation (2.24). Nonlinear deformations can be described using the finite segments

approach, if the flexible body is divided into a large number of discrete mass points while the deformations between the mass points remain linear. The finite segments approach is suitable for the analysis of beam-like structures; however, a detailed description of the flexibility of the structure leads to a large number of degrees of freedom. In Chapter 4, the finite segments approach is used to describe the flexibility of the rotor of an electric motor.

2.2 Floating Frame of Reference Formulation

The most commonly used method in the analysis of flexible multibody structures is the floating frame of reference formulation [21]. In this method, a flexible body motion is separated into a reference motion and deformation. The deformation of the body can be described using shape functions or assumed modes. Usually, the deformation of the body is described by the superposition of the vibration modes that are obtained from a finite element solution.

2.2.1 The Kinematics of a Flexible Body

In a mathematical sense, a flexible body consists of particles the locations of which can be described using a local coordinate system. The local coordinate system is attached to the body, and the deformation of the body is defined with respect to the local coordinate system. The local coordinate system can undergo large nonlinear translation and rotation in relation to the fixed global coordinate system. Figure 2.1 describes the vectors that define the global position of a particle. The global position of an arbitrary particle, P , in the flexible body i can be expressed in the following form [21]:

$$\mathbf{r}^i = \mathbf{R}^i + \mathbf{A}^i \bar{\mathbf{u}}^i = \mathbf{R}^i + \mathbf{A}^i (\bar{\mathbf{u}}_0^i + \bar{\mathbf{u}}_f^i), \quad (2.25)$$

where $\bar{\mathbf{u}}_0^i$ is the position vector that defines the undeformed position of the particle and $\bar{\mathbf{u}}_f^i$ is the position vector that defines the deformation of the particle.

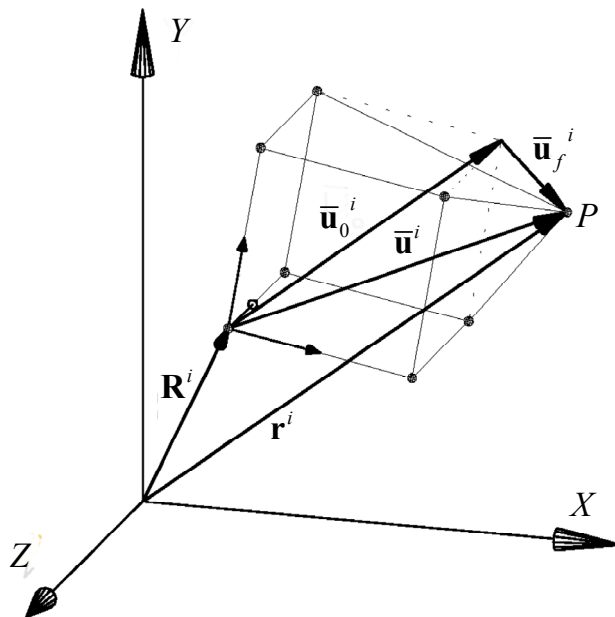


Figure 2.1 The global position of an arbitrary particle, P .

Flexible bodies have an infinite number of degrees of freedom that define the position of every particle of a body. For computational reasons, the deformation vector must be

defined using a finite number of coordinates. This approximation can be carried out using the Rayleigh-Ritz or finite element method. Using matrix formulation, the approximation can be expressed as follows:

$$\bar{\mathbf{u}}_f^i = \mathbf{\Phi}^i \mathbf{p}^i, \quad (2.26)$$

where $\mathbf{\Phi}^i$ is a shape matrix and \mathbf{p}^i is the vector of elastic coordinates. In practice, the shape matrix, $\mathbf{\Phi}^i$, can be most conveniently obtained using the finite element method, as will be explained in Section 2.2.2. The vector of generalized coordinates of the flexible body i can be written as follows:

$$\mathbf{q} = \begin{bmatrix} \mathbf{R}^{iT} & \boldsymbol{\theta}^{iT} & \mathbf{p}^{iT} \end{bmatrix}^T. \quad (2.27)$$

The velocity of an arbitrary particle, P , can be obtained by differentiating Equation (2.25) with respect to time as follows:

$$\dot{\mathbf{r}}^i = \dot{\mathbf{R}}^i + \dot{\mathbf{A}}^i \bar{\mathbf{u}}^i + \mathbf{A}^i \dot{\bar{\mathbf{u}}}^i, \quad (2.28)$$

where the time derivative of the position vector in the local coordinate system can be written as

$$\dot{\bar{\mathbf{u}}}^i = \mathbf{\Phi} \dot{\mathbf{p}} \quad (2.29)$$

Using Equation (2.4), the velocity vector can be written in partitioned form as follows:

$$\dot{\mathbf{r}}^i = \begin{bmatrix} \mathbf{I} & -\mathbf{A}^i \bar{\mathbf{u}}^i \bar{\mathbf{G}}^i & \mathbf{A}^i \mathbf{\Phi}^i \end{bmatrix} \begin{bmatrix} \dot{\mathbf{R}}^i \\ \dot{\boldsymbol{\theta}}^i \\ \dot{\mathbf{p}}^i \end{bmatrix} \quad (2.30)$$

2.2.2 Solving the Shape Matrix Using Finite Element Method

The shape matrix $\mathbf{\Phi}^i$ in Equation (2.26) can be constructed using the finite element shape functions [21]. However, in most engineering applications, the structure under analysis is rather complex and the finite element model of the entire structure may contain a large number of nodal variables. For this reason, it is not practical, from the computational perspective, to perform a dynamic analysis based on the complete finite element model. Methods, such as substructuring or component mode synthesis, have been developed to overcome this problem.

In component mode synthesis, the vibration modes are often solved from the finite element model. The vibration modes and frequencies can be obtained by solving the standard eigenvalue problem as follows:

$$(\mathbf{K}_s - \omega_k^2 \mathbf{M}_s) \boldsymbol{\phi}_k = \mathbf{0}, \quad (2.31)$$

where \mathbf{K}_s and \mathbf{M}_s are the stiffness and mass matrices obtained from the finite element model of the structure, when the boundary conditions consistent with the floating frame reference conditions are applied, and ω_k^2 and $\boldsymbol{\phi}_k$ are the k th eigenvalue and eigenvector, respectively. The dimensionality of the problem can be reduced by retaining only n_m mode

shapes of a total of n_f mode shapes, where $n_m < n_f$. The vibration modes can be solved using the matrices of the constrained or unconstrained structure. A generally used approach is to use the vibration modes of an unconstrained system. One drawback to this approach is the description of the local deformations that are caused by the constraint forces or externally applied forces. An accurate description of the local deformation requires a large number of unconstrained vibration modes. To capture local deformations, many researchers [25-27] have used additional static correction modes.

A commonly used substructuring method is the Craig-Bampton method [28] in which the structure is divided into interior and boundary degrees of freedom. In the partitioned form, the stiffness matrix, \mathbf{K}_s , and mass matrix, \mathbf{M}_s , of the structure can be written as follows:

$$\mathbf{K}_s = \begin{bmatrix} \mathbf{K}^{BB} & \mathbf{K}^{BI} \\ \mathbf{K}^{IB} & \mathbf{K}^{II} \end{bmatrix}, \quad (2.32)$$

$$\mathbf{M}_s = \begin{bmatrix} \mathbf{M}^{BB} & \mathbf{0} \\ \mathbf{0} & \mathbf{M}^{II} \end{bmatrix} \quad (2.33)$$

where superscripts B and I refer to the boundary and interior, respectively. The component normal modes can be classified as fixed-interface normal modes when the interface degrees of freedom are fixed and the normal modes are obtained by solving the following eigenvalue problem:

$$\left[\mathbf{K}^{II} - (\omega_k^N)^2 \mathbf{M}^{II} \right] \boldsymbol{\phi}_k^N = \mathbf{0} \quad (2.34)$$

The matrix of the fixed-interface normal modes can be obtained using retained eigenvectors, as follows:

$$\boldsymbol{\Phi}^N = \left[\boldsymbol{\phi}_1^N \quad \cdots \quad \boldsymbol{\phi}_{n_m}^N \right] \quad (2.35)$$

Constraint modes, i.e. static correction modes, are the mode shapes of the interior degrees of freedom due to the successive unit displacements of the boundary degrees of freedom. The constraint modes are obtained from the static force equilibrium, Equation (2.36), by setting all the forces \mathbf{F}^I at the interior degrees of freedom to zero, which yields Equation (2.37).

$$\begin{bmatrix} \mathbf{F}^B \\ \mathbf{F}^I \end{bmatrix} = \begin{bmatrix} \mathbf{K}^{BB} & \mathbf{K}^{BI} \\ \mathbf{K}^{IB} & \mathbf{K}^{II} \end{bmatrix} \begin{bmatrix} \boldsymbol{\delta}^B \\ \boldsymbol{\delta}^I \end{bmatrix} \quad (2.36)$$

$$\boldsymbol{\delta}^I = -(\mathbf{K}^{II})^{-1} \mathbf{K}^{IB} \boldsymbol{\delta}^B = \boldsymbol{\Phi}^C \boldsymbol{\delta}^B, \quad (2.37)$$

where $\boldsymbol{\delta}^I$ and $\boldsymbol{\delta}^B$ are the physical displacements of the interior and boundary nodes, respectively. Matrix $\boldsymbol{\Phi}^C$ is the matrix of the constraint modes.

The coordinate transformation that relates the substructure's final, i.e. modal, coordinates $\hat{\mathbf{p}}$ to the substructure's initial, i.e. physical, coordinates is [28]:

$$\mathbf{u}_f = \begin{bmatrix} \boldsymbol{\delta}^B \\ \boldsymbol{\delta}^I \end{bmatrix} \cong \begin{bmatrix} \mathbf{I} & \mathbf{0} \\ \boldsymbol{\Phi}^C & \boldsymbol{\Phi}^N \end{bmatrix} \begin{bmatrix} \hat{\mathbf{p}}^C \\ \hat{\mathbf{p}}^N \end{bmatrix} = \hat{\boldsymbol{\Phi}} \hat{\mathbf{p}} \quad (2.38)$$

By using the generalized mode shape matrix, $\hat{\Phi}$, the generalized stiffness and mass matrix of the substructure are obtained as follows

$$\hat{\mathbf{K}} = \hat{\Phi}^T \mathbf{K}_s \hat{\Phi} \quad (2.39)$$

$$\hat{\mathbf{M}} = \hat{\Phi}^T \mathbf{M}_s \hat{\Phi}. \quad (2.40)$$

These generalized matrices are the Craig-Bampton representation of the original system. It is important to emphasize that the mode shapes in Equation (2.38) are not orthogonal with respect to the mass and stiffness matrices. As a result, the generalized stiffness and mass matrices contain non-zero off-diagonal terms. For this reason, the coupling between the generalized elastic coordinates cannot be removed.

In the floating frame of reference formulation, the reference frame describes the large reference motions of a body. For this reason, the deformation modes cannot contain any rigid body motions, i.e. motions in which displacements occur without deformation. Unconstrained vibration modes have six rigid body modes that represent translations and small rotations. These modes can be identified and removed from the eigenmode basis. Another option is to use the vibration modes of a fully constrained structure, such as the cantilever modes of beams. The selection of the deformation modes influences the motion that the reference coordinate system describes. In the case of unconstrained vibration modes, the reference coordinate system is not rigidly attached to any physical point on a body, and the reference motion is the mean rigid body motion. This leads to the mean axis frame, which is chosen in such a way that the linear and angular momentum due to deformation are zero [29, 30]. When constrained mode shapes are used, the reference coordinate system is rigidly attached to a specific physical point on a body. An important issue in selecting the deformation modes and reference coordinate system is that the modes defined in one reference coordinate system should not be used in another coordinate system [31]. This might cause difficulties when combining vibration modes and static correction modes, since these modes may be defined using different reference conditions.

The Craig-Bampton modes described above cannot be used directly in the floating frame of reference formulation, since they contain rigid body modes and the vibration and the constraint modes may be defined using different reference frames. However, the modes can be orthogonalized [24] by solving the eigenvalues from the Craig-Bampton representation of the structure as follows:

$$\left[\hat{\mathbf{K}} - \hat{\omega}_k^2 \hat{\mathbf{M}} \right] \mathbf{n}_k = \mathbf{0} \quad (2.41)$$

The new orthogonal mode shape matrix can be defined as

$$\mathbf{N} = \left[\mathbf{n}_1 \quad \cdots \quad \mathbf{n}_{n_{CB}} \right], \quad (2.42)$$

where n_{CB} is the number of Craig-Bampton modes. The final mode shapes and physical degrees of freedom can be expressed as follows:

$$\Phi = \hat{\Phi} \mathbf{N} \quad (2.43)$$

$$\bar{\mathbf{u}}_f \cong \Phi \mathbf{p} \quad (2.44)$$

As a result of the orthogonalization procedure, the stiffness and mass matrices become diagonal

$$\mathbf{K}_p = \mathbf{\Phi}^T \hat{\mathbf{K}} \mathbf{\Phi} = \text{diag}(\hat{\omega}_1^2, \dots, \hat{\omega}_{n_{CB}}^2), \quad (2.45)$$

$$\mathbf{M}_p = \mathbf{\Phi}^T \hat{\mathbf{M}} \mathbf{\Phi} = \mathbf{I} \quad (2.46)$$

A useful side effect of this orthogonalization procedure is that all the modes have an associated frequency in order for their frequency contribution to the dynamic system to be identified [24]. However, the physical meaning of the static correction modes is lost in the orthogonalization procedure. The orthogonalized mode shapes include approximate free-free modes and the vibration modes of boundary degrees of freedom.

2.2.3 The System's Equations of Motion

A number of general-purpose computer applications for multibody dynamics are based on the Lagrangian method. When the constraint equations are taken into account using Lagrange multipliers, the Lagrangian equation can be written in the following form:

$$\frac{d}{dt} \left(\frac{\partial L}{\partial \dot{\mathbf{q}}} \right) - \left(\frac{\partial L}{\partial \mathbf{q}} \right) + \mathbf{C}_q^T \boldsymbol{\lambda} = \mathbf{Q}_e, \quad (2.47)$$

where \mathbf{C}_q is the Jacobian matrix calculated using generalized coordinates, \mathbf{q} , $\boldsymbol{\lambda}$ is the vector of Lagrange multipliers and \mathbf{Q}_e is the vector of the generalized external forces. The Lagrangian, L , is defined as follows

$$L = T - V, \quad (2.48)$$

where T and V denote the kinetic and potential energy, respectively. Substituting the kinetic energy as well as potential energy into the Lagrangian Equation (2.47) gives the equations of the constrained motion of a flexible multibody system:

$$\mathbf{M}\ddot{\mathbf{q}} + \dot{\mathbf{M}}\dot{\mathbf{q}} - \frac{1}{2} \left[\frac{\partial}{\partial \mathbf{q}} (\dot{\mathbf{q}}^T \mathbf{M} \dot{\mathbf{q}}) \right]^T + \mathbf{K}\mathbf{q} + \mathbf{f}_g + \mathbf{D}_d \dot{\mathbf{q}} + \mathbf{C}_q^T \boldsymbol{\lambda} = \mathbf{Q}_e, \quad (2.49)$$

where \mathbf{f}_g is the gravitational force. The stiffness matrix, \mathbf{K} , and the damping matrix, \mathbf{D}_d , can be written as

$$\mathbf{K} = \begin{bmatrix} \mathbf{0} & \mathbf{0} & \mathbf{0} \\ \mathbf{0} & \mathbf{0} & \mathbf{0} \\ \mathbf{0} & \mathbf{0} & \mathbf{K}_p \end{bmatrix}, \quad \mathbf{D}_d = \begin{bmatrix} \mathbf{0} & \mathbf{0} & \mathbf{0} \\ \mathbf{0} & \mathbf{0} & \mathbf{0} \\ \mathbf{0} & \mathbf{0} & \mathbf{D}_p \end{bmatrix}, \quad (2.50)$$

where $\mathbf{0}$ are null matrices and matrix \mathbf{D}_p contains modal damping ratios. Using the following expressions

$$\mathbf{Q}_v = -\dot{\mathbf{M}}\dot{\mathbf{q}} + \frac{1}{2} \left[\frac{\partial}{\partial \mathbf{q}} (\dot{\mathbf{q}}^T \mathbf{M} \dot{\mathbf{q}}) \right]^T, \quad (2.51)$$

$$\mathbf{Q}_E = \mathbf{Q}_e - \mathbf{K}\mathbf{q} - \mathbf{f}_g - \mathbf{D}_d\dot{\mathbf{q}}, \quad (2.52)$$

the equation of constrained motion takes the following form:

$$\mathbf{M}\ddot{\mathbf{q}} + \mathbf{C}_q^T \boldsymbol{\lambda} = \mathbf{Q}_E + \mathbf{Q}_v, \quad (2.53)$$

where \mathbf{Q}_v is a vector of the quadratic velocity inertia forces that includes the gyroscopic and Coriolis forces. The vector of the quadratic velocity inertia forces is a nonlinear function of the system's generalized coordinates and velocities. The force vector, \mathbf{Q}_E , includes the descriptions of both conservative and non-conservative forces.

Mass Matrix The mass matrix in Equation (2.49) is a complex function of the rotational coordinates and deformation of the flexible body. The mass matrix can be written using nine submatrices as follows:

$$\mathbf{M} = \begin{bmatrix} \mathbf{m}_{RR} & \mathbf{m}_{R\theta} & \mathbf{m}_{Rp} \\ & \mathbf{m}_{\theta\theta} & \mathbf{m}_{\theta p} \\ \text{symm.} & & \mathbf{m}_{pp} \end{bmatrix}, \quad (2.54)$$

where subscripts R , θ and p refer to the translational, rotational and modal coordinates, respectively. The submatrices can be written as

$$\mathbf{m}_{RR} = \int_V \rho \mathbf{I} dV = \mathbf{I}^1 \mathbf{I} \quad (2.55)$$

$$\mathbf{m}_{R\theta} = -\int_V \rho \mathbf{A} \tilde{\mathbf{u}} \bar{\mathbf{G}} dV = -\mathbf{A} \tilde{\mathbf{I}}_{R\theta} \bar{\mathbf{G}}, \quad (2.56)$$

where $\mathbf{I}_{R\theta} = \mathbf{I}^2 + \sum_{j=1}^M \mathbf{I}_j^3 p_j$ and M is the number of modal coordinates.

$$\mathbf{m}_{Rp} = \int_V \rho \mathbf{A} \Phi dV = \mathbf{A} \mathbf{I}^3 \quad (2.57)$$

$$\begin{aligned} \mathbf{m}_{\theta\theta} &= \int_V \rho \bar{\mathbf{G}}^T \tilde{\mathbf{u}}^T \tilde{\mathbf{u}} \bar{\mathbf{G}} dV \\ &= \bar{\mathbf{G}}^T \left[\mathbf{I}^7 - \sum_{j=1}^M (\mathbf{I}_j^8 + \mathbf{I}_j^{8T}) p_j - \sum_{j=1}^M \sum_{k=1}^M \mathbf{I}_{jk}^9 p_j p_k \right] \bar{\mathbf{G}} \end{aligned} \quad (2.58)$$

$$\mathbf{m}_{\theta p} = -\int_V \rho \bar{\mathbf{G}}^T \tilde{\mathbf{u}}^T \Phi dV = \bar{\mathbf{G}}^T \left[\mathbf{I}^4 + \sum_{j=1}^M \mathbf{I}_j^5 p_j \right] \quad (2.59)$$

$$\mathbf{m}_{pp} = \int_V \rho \Phi^T \Phi dV = \mathbf{I}^6 \quad (2.60)$$

The components of the mass matrix can be partitioned into time-dependent and time-independent terms. The time-invariant terms can be calculated once before the time integration of the equations of motion. The time-invariants can be calculated as volume integrals or, in case of lumped masses, as summations. In the latter case, the invariants are calculated from N nodes of the finite element model using each node's mass, m_i , undeformed location, $\bar{\mathbf{u}}_{0i}$, and contribution to the modes, Φ_i [24]. Note that matrix Φ_i only contains the terms that correspond to the translational degrees of freedom of node i . The contribution of the rotational degrees of freedom is excluded, since usually in lumped

mass formulation, the rotation inertias of the nodes are neglected. The nine invariants appearing in the mass matrix can be expressed as follows: Invariant \mathbf{I}^1 is the total mass of the body

$$\mathbf{I}^1 = \int_V \rho dV \cong \sum_{i=1}^N m_i \quad (2.61)$$

Invariant \mathbf{I}^2 is a 3×1 vector containing the first moments of mass of a flexible body in an undeformed state

$$\mathbf{I}^2 = \int_V \rho \bar{\mathbf{u}}_0 dV \cong \sum_{i=1}^N m_i \bar{\mathbf{u}}_{0i} \quad (2.62)$$

Invariant \mathbf{I}^3 is a $3 \times M$ matrix that includes correction terms for the first moments of mass due to deformation. Column j of \mathbf{I}^3 describes the contribution of modal coordinate p_j to the movement of the center of mass. Column j of \mathbf{I}^3 can be calculated as follows:

$$\mathbf{I}_j^3 = \int_V \rho \boldsymbol{\varphi}_j dV \cong \sum_{i=1}^N m_i \boldsymbol{\varphi}_{ij}, \quad (2.63)$$

where $\boldsymbol{\varphi}_j$ is j th mode and $\boldsymbol{\varphi}_{ij}$ contribution of node i to mode j . Invariant \mathbf{I}^4 is a $3 \times M$ matrix that includes cross-coupling terms between rotation and deformation.

$$\mathbf{I}^4 = \int_V \rho \tilde{\mathbf{u}}_0 \boldsymbol{\Phi} dV \cong \sum_{i=1}^N m_i \tilde{\mathbf{u}}_{0i} \boldsymbol{\Phi}_i \quad (2.64)$$

Invariant \mathbf{I}^5 is a second-order correction for the cross-coupling between deformation and rotation and consists of M number $3 \times M$ matrices. The term that corresponds to mode j can be calculated as follows:

$$\mathbf{I}_j^5 = \int_V \rho \tilde{\boldsymbol{\varphi}}_j \boldsymbol{\Phi} dV \cong \sum_{i=1}^N m_i \tilde{\boldsymbol{\varphi}}_{ij} \boldsymbol{\Phi}_i \quad (2.65)$$

Invariant \mathbf{I}^6 is a generalized mass matrix, i.e. the modal mass, of the flexible body. The dimensions of \mathbf{I}^6 are $M \times M$, and it can be calculated as follows:

$$\mathbf{I}^6 = \int_V \rho \boldsymbol{\Phi}^T \boldsymbol{\Phi} dV \cong \sum_{i=1}^N m_i \boldsymbol{\Phi}_i^T \boldsymbol{\Phi}_i \quad (2.66)$$

Invariant \mathbf{I}^7 is a 3×3 inertia tensor of the flexible body and can be calculated as follows:

$$\mathbf{I}^7 = \int_V \rho \tilde{\mathbf{u}}_0^T \tilde{\mathbf{u}}_0 dV \cong \sum_{i=1}^N m_i \tilde{\mathbf{u}}_{0i}^T \tilde{\mathbf{u}}_{0i} \quad (2.67)$$

Invariants \mathbf{I}^8 and \mathbf{I}^9 are the first- and second-order corrections of the inertia tensor due to deformation, respectively. Invariant \mathbf{I}^8 consists of M number of 3×3 matrices that can be calculated as follows:

$$\mathbf{I}_j^8 = \int_V \rho \tilde{\mathbf{u}}_0 \tilde{\Phi}_j dV \cong \sum_{i=1}^N m_i \tilde{\mathbf{u}}_{0i} \tilde{\Phi}_{ij} \quad (2.68)$$

Accordingly, invariant \mathbf{I}^9 consists of M^2 number of 3×3 matrices that can be calculated as follows:

$$\mathbf{I}_{jk}^9 = \int_V \rho \tilde{\Phi}_j \tilde{\Phi}_k dV \cong \sum_{i=1}^N m_i \tilde{\Phi}_{ij} \tilde{\Phi}_{ik} \quad (2.69)$$

Quadratic Velocity Inertia Forces The vector of the quadratic velocity inertia forces, \mathbf{Q}_v , contains the gyroscopic and Coriolis force components. In component form, it can be written as

$$\mathbf{Q}_v = \left[(\mathbf{Q}_v)_R^T \quad (\mathbf{Q}_v)_\theta^T \quad (\mathbf{Q}_v)_p^T \right]^T \quad (2.70)$$

In a three dimensional analysis, the components can be written as [21]

$$\begin{aligned} (\mathbf{Q}_v)_R &= -\mathbf{A} \left[\tilde{\omega}^2 \bar{\mathbf{S}}_t + 2\tilde{\omega} \bar{\mathbf{S}} \dot{\mathbf{p}} \right] \\ (\mathbf{Q}_v)_\theta &= -2\dot{\bar{\mathbf{G}}}^T \bar{\mathbf{I}}_{\theta\theta} \bar{\omega} - 2\dot{\bar{\mathbf{G}}}^T \bar{\mathbf{I}}_{\theta p} \dot{\mathbf{p}} - \dot{\bar{\mathbf{G}}}^T \bar{\mathbf{I}}_{\theta\theta} \bar{\omega}, \\ (\mathbf{Q}_v)_p &= -\int_V \rho \left\{ \Phi^T \left[\tilde{\omega}^2 \bar{\mathbf{u}} + 2\tilde{\omega} \Phi \dot{\mathbf{p}} \right] \right\} dV \end{aligned} \quad (2.71)$$

where $\bar{\mathbf{S}}_t = \int_V \rho \bar{\mathbf{u}} dV$, $\bar{\mathbf{S}} = \int_V \rho \Phi dV$, $\bar{\mathbf{I}}_{\theta\theta} = \int_V \rho \tilde{\mathbf{u}}^T \tilde{\mathbf{u}} dV$ and $\bar{\mathbf{I}}_{\theta p} = \int_V \rho \tilde{\mathbf{u}}^T \Phi dV$.

Generalized External Forces The virtual work of the external forces acting on a body can be written as

$$\delta W_e = \mathbf{F}^T \delta \mathbf{r}_p, \quad (2.72)$$

where \mathbf{F} is an external force vector applied at point \mathbf{r}_p . The virtual change of \mathbf{r}_p can be written in partitioned form as

$$\delta \mathbf{r}_p = \begin{bmatrix} \mathbf{I} & -\mathbf{A} \tilde{\mathbf{u}}_p \bar{\mathbf{G}} & \mathbf{A} \Phi_p \end{bmatrix} \begin{bmatrix} \delta \mathbf{R} \\ \delta \boldsymbol{\theta} \\ \delta \mathbf{p} \end{bmatrix}, \quad (2.73)$$

where $\bar{\mathbf{u}}_p$ is the position vector of point P and Φ_p are the modes shapes corresponding to point P . Using the expression of virtual work, the generalized forces affecting the translation, rotation and modal coordinates can be written as follows:

$$(\mathbf{Q}_e)_R^T = \mathbf{F}^T \quad (2.74)$$

$$(\mathbf{Q}_e)_\theta^T = -\mathbf{F}^T \mathbf{A} \tilde{\mathbf{u}}_p \bar{\mathbf{G}} \quad (2.75)$$

$$(\mathbf{Q}_e)_p^T = -\mathbf{F}^T \mathbf{A} \Phi_p \quad (2.76)$$

The floating frame of reference formulation can be used to analyze flexible rotors. The nonidealities of the rotor, such as unideal mass and stiffness distribution, can be taken into account in the finite element model of the rotor. The bearing forces can be included in the analysis in the form of external forces; therefore, the interactions between the flexible rotor and a nonideal bearing can be taken into consideration. However, one limitation in using linear modes in the component mode synthesis is that the deformations are assumed to be small and linear. In high-speed rotor dynamic applications, a nonlinear phenomenon called stress stiffening or centrifugal stiffening should be taken into account. Nonlinear effects are included in the large rotation vector formulation or in the absolute nodal coordinate formulation, which will be discussed in the next section. It is important to point out that nonlinear deformations can be modeled in the floating frame of reference formulation by dividing the flexible body into substructures or by using nonlinear stiffness terms as in [22, 32]. However, in these cases, the floating frame of reference formulation becomes cumbersome.

2.3 Large Deformation Formulations in Multibody Simulation

There are three finite element formulations that can be used in the large rotation and deformation analysis of flexible multibody systems. These are the co-rotational procedure, the large rotation vector formulation and the absolute nodal coordinate formulation. All these formulations have been applied to three-dimensional beams, plates and shells. However, the discussion in this section is focused on beam elements.

Co-rotational finite element procedures [33, 34] are developed for non-isoparametric elements, in which infinitesimal rotations are used as the nodal coordinates. The basic idea in these techniques is to separate rigid body motion and strain-producing deformation from the global displacement field. Large displacements are described by small increments between time or load steps. The increments are chosen in such a way that the rotation of an element between two consecutive configurations is small, and the local element shape functions and local nodal coordinates can be used to describe this rotation. The maximum rotation in one step must be less than 30° [35, 36]. The selection of the correct increment step is, thus, very important for the convergence of the solution. The benefit of this method is that it can be easily implemented in existing finite element formulations. The limitation of the co-rotational procedure is that it may not lead to an exact rigid-body inertia representation due to the early linearization of the equations of motion [37]. Co-rotational formulations are not widely used in multibody applications and are, thus, not considered in detail here. The interested reader can find more information in the review articles by Shabana [38] and Wasfy and Noor [39] and in the references cited therein. In addition, a comparison between the incremental co-rotational procedure and the absolute nodal coordinate formulation is performed in Reference [35].

The large rotation vector formulation [40-48] has been the subject of extensive research for over two decades. The formulation has been successfully applied into nonlinear analysis of, for example, lightweight space structures. In the large rotation vector formulation, the rotations of the cross-section and global displacements of the centerline of an element are used as the nodal coordinates. Beams are described as one-dimensional lines, i.e. they are parametrized using only longitudinal coordinates. In three-dimensional cases, six independent nodal coordinates are sufficient per node to describe the configuration of the element. The nodal coordinates in the large rotation vector formulation have a clear physical meaning, since they describe the translations and rotations relative to the global inertial coordinate system. The cross-section rotation within an element is approximated through the use of interpolation polynomials. The finite element interpolation of the

rotations must be carefully handled, since it can lead to frame-indifferent and path-dependent elements, as described in [47]. Moreover, the use of rotations as the nodal coordinates often leads to excessive shear forces, which produces a phenomenon known as shear locking. This problem can be alleviated using a reduced numerical integration procedure. In some cases, reduced numerical integration can produce an ill-conditioned stiffness matrix, which leads to spurious zero energy modes. In the large rotation vector formulation, the rigid body motion and deformation of the beam element are expressed directly in a fixed inertial frame. This simplifies the description of the inertia of the element. It is important to note, however, that, in a three-dimensional case, the large rotation vector formulation does not lead to a constant mass matrix.

The absolute nodal coordinate formulation is a recently developed method based on the finite element formulation [21] and is designed for large deformation multibody analysis; the absolute nodal coordinate formulation has been applied to three-dimensional beams [49, 50] and shells [51]. In the absolute nodal coordinate formulation, slopes and displacements are used as the nodal coordinates instead of infinitesimal or finite rotations. This helps avoid the cumbersome interpolation of rotational coordinates. By using slopes instead of rotations, no assumptions are made with regard to the magnitude of the deformation within the element. The absolute nodal coordinate formulation uses a displacement field that is linear in the nodal coordinates. In addition, the shape function matrix, together with the nodal coordinates, is able to describe arbitrary rigid body motion. For these reasons, the absolute nodal coordinate formulation leads to a constant mass matrix in two- and three-dimensional cases. The constant mass matrix simplifies the nonlinear equations of motion and, consequently, accelerates the time integration of the nonlinear equations of motion. The absolute nodal coordinate formulation can be used in the framework of a non-incremental solution procedure.

2.3.1 Large Rotation Vector Formulation

The large rotation vector formulation [40-48] is based on the large displacement and rotation theory. In this formulation, a vector field defines the position of the centerline of the element. The cross-section of the beam is defined by a moving frame, which is oriented by an orthogonal matrix, i.e. a rotation matrix. In the large rotation vector formulation, it is assumed that the cross-section remains plane and maintains its area, as well as its shape, during deformation. This formulation expresses rigid body motion and the deformation of the beam element directly in the fixed inertial frame. The configuration of the beam is described completely by vector \mathbf{R} that defines the centerline of the beam and the rotation matrix, $\mathbf{\Lambda}$, as follows:

$$\mathbf{r}(x, y, z) = \mathbf{R}(x) + \mathbf{\Lambda}(x) \begin{bmatrix} 0 & y & z \end{bmatrix}^T, \quad (2.77)$$

where x is a coordinate along the centerline of the beam and y and z are coordinates on the cross-section. The rotation matrix can be parameterized by using the rotational vector as follows [46]

$$\mathbf{\Lambda} = \exp \tilde{\boldsymbol{\psi}} = \mathbf{I} + \frac{\sin |\boldsymbol{\psi}|}{|\boldsymbol{\psi}|} \tilde{\boldsymbol{\psi}} + \frac{1 - \cos |\boldsymbol{\psi}|}{|\boldsymbol{\psi}|^2} \tilde{\boldsymbol{\psi}}^2, \quad (2.78)$$

where $\tilde{\boldsymbol{\psi}}$ is the skew-symmetric matrix associated with the rotational vector $\boldsymbol{\psi} = [\psi_1 \quad \psi_2 \quad \psi_3]^T$.

During the solution procedure, the rotation matrix must be updated. The relationship between the rotation matrices in two consecutive configurations, k and $k+1$, of the element can be defined using the rotational vector as follows:

$$\Lambda^{k+1} = \exp \tilde{\Psi} \Lambda^k \quad (2.79)$$

In the large rotation vector formulation, strains are defined through the use of a body-attached frame. This can be accomplished by defining translational Γ and rotational κ strain measures using the current configuration of the beam element, (\mathbf{R}, Λ) , as follows:

$$\Gamma = \Lambda^T \mathbf{R}' - [1 \ 0 \ 0]^T \quad (2.80)$$

$$\kappa = \Lambda^T \boldsymbol{\omega}, \quad (2.81)$$

where the vector $\boldsymbol{\omega}$ can be obtained by employing the rotational vector. In Equation (2.80), \mathbf{R}' is a derivation of vector \mathbf{R} with respect to x . In the large rotation vector formulation, it is difficult to establish the relationship between finite rotations and strains [46]. The representation of the three-dimensional rotation of a moving frame with respect to the inertial frame is not linear, while the finite rotations are, in general, not commutative. The interpolation of the rotations along the beam length becomes, thus, nontrivial and must be handled carefully. As pointed out by Jelenić and Crisfield [47], the interpolation of the rotation coordinates of the beam element can lead to frame-indifferent and path-dependent elements. In the large rotation vector formulation, the strain measures may not be invariant under rigid body motion and the strains may be dependent on the history of the deformation. In order to overcome these drawbacks, Jelenić and Crisfield [47] proposed the interpolation of local rotations in a co-rotational manner.

Another approach for three-dimensional beam formulation was proposed by Avello and García de Jalón [43]. They used orthogonal unit vectors to describe the cross-section of the beam. The components of these vectors are used as nodal variables, and finite element interpolation is applied to these vectors instead of to the rotational degrees of freedom. Constraint equations are used to obtain orthonormality and the unit length conditions of the vectors that define the cross-section of the beam. This method causes the mass matrix of the beam element to become constant and singular. It must be noted that the singularity of the mass matrix is not a problem, since the equations of motion are solved using the Newmark procedure, which does not require the inverse of the mass matrix.

In [52], it was shown analytically that the kinematical description of the large rotation vector formulation provides consistent dynamic formulation for rotating Timoshenko beams including gyroscopic terms. However, the large rotation vector formulation is not a very attractive method for transient rotor dynamics analysis, since the mass matrix, as well as the stiffness matrix, is a nonlinear function of the system's rotational coordinates. Furthermore, difficulties in interpolations of the rotation coordinates may cause problems in high-speed rotor dynamic applications. On the other hand, the absolute nodal coordinate formulation leads to a constant mass matrix and there is no need to interpolate infinitesimal or finite rotations.

2.3.2 Absolute Nodal Coordinate Formulation

The Kinematics of an Element In the absolute nodal coordinate formulation, the global position vector, \mathbf{r} , of an arbitrary point on a three-dimensional element can be written as

$$\mathbf{r} = \mathbf{S}(x, y, z)\mathbf{e}, \quad (2.82)$$

where \mathbf{S} is the element shape function matrix, x , y and z are the local coordinates of the element and \mathbf{e} is the vector of the nodal coordinates. The shape function matrix and vector of the nodal coordinates must be selected in such a way that they represent both arbitrary rigid body motion and element deformation. The displacement field of a three-dimensional beam element can be obtained using the following polynomial expression [50]:

$$\mathbf{r} = \begin{bmatrix} r_1 \\ r_2 \\ r_3 \end{bmatrix} = \begin{bmatrix} a_0 + a_1x + a_2y + a_3z + a_4xy + a_5xz + a_6x^2 + a_7x^3 \\ b_0 + b_1x + b_2y + b_3z + b_4xy + b_5xz + b_6x^2 + b_7x^3 \\ c_0 + c_1x + c_2y + c_3z + c_4xy + c_5xz + c_6x^2 + c_7x^3 \end{bmatrix} \quad (2.83)$$

In Equation (2.83), the element is described as being a continuous volume, which makes the deformation of the cross-section possible. The assumed displacement field in Equation (2.83) includes 24 unknown polynomial coefficients. For a two-noded beam element (I, J), 12 nodal coordinates can be used for each node. The coordinates of node I , \mathbf{e}_I , can be written as

$$\mathbf{e}_I = \left[\mathbf{r}_I^T \quad \frac{\partial \mathbf{r}_I^T}{\partial x} \quad \frac{\partial \mathbf{r}_I^T}{\partial y} \quad \frac{\partial \mathbf{r}_I^T}{\partial z} \right]^T, \quad (2.84)$$

where vector \mathbf{r}_I defines the global position of node I and vectors $\partial \mathbf{r}_I / \partial x$, $\partial \mathbf{r}_I / \partial y$ and $\partial \mathbf{r}_I / \partial z$ are the slopes at node I . A physical interpretation of the slope coordinates is given in a simple example in References [53, 54]. Using the interpolating polynomial introduced in Equation (2.83) and the nodal coordinates, the element shape function matrix, \mathbf{S} , can be expressed as follows:

$$\mathbf{S} = [\mathbf{S}_1\mathbf{I} \quad \mathbf{S}_2\mathbf{I} \quad \mathbf{S}_3\mathbf{I} \quad \mathbf{S}_4\mathbf{I} \quad \mathbf{S}_5\mathbf{I} \quad \mathbf{S}_6\mathbf{I} \quad \mathbf{S}_7\mathbf{I} \quad \mathbf{S}_8\mathbf{I}], \quad (2.85)$$

where \mathbf{I} is a 3 x 3 identity matrix and

$$\begin{aligned} S_1 &= 1 - 3\xi^2 + 2\xi^3, & S_2 &= l(\xi - 2\xi^2 + \xi^3), & S_3 &= l\eta(1 - \xi), & S_4 &= l\zeta(1 - \xi), \\ S_5 &= 3\xi^2 - 2\xi^3, & S_6 &= l(-\xi^2 + \xi^3), & S_7 &= l\xi\eta, & S_8 &= l\xi\zeta. \end{aligned}$$

The non-dimensional quantities, ξ , η , ζ , are defined as

$$\xi = \frac{x}{l}, \quad \eta = \frac{y}{l}, \quad \zeta = \frac{z}{l}, \quad (2.86)$$

where l is the length of the beam element in the initial configuration. The values of the slope coordinates at any arbitrary point on the element can be interpolated with the use of nodal coordinates. The interpolation of the slope coordinates, unlike that of infinite or finite rotations, is straightforward.

Mass matrix The mass matrix of the element can be obtained using the following expression for the kinetic energy

$$T = \frac{1}{2} \int_V \rho \dot{\mathbf{r}}^T \dot{\mathbf{r}} dV = \frac{1}{2} \int_V \rho \dot{\mathbf{e}}^T \mathbf{S}^T \mathbf{S} \dot{\mathbf{e}} dV = \frac{1}{2} \dot{\mathbf{e}}^T \left[\int_V \rho \mathbf{S}^T \mathbf{S} dV \right] \dot{\mathbf{e}} = \frac{1}{2} \dot{\mathbf{e}}^T \mathbf{M} \dot{\mathbf{e}}, \quad (2.87)$$

where ρ is the density of the element, V is the volume of the element and $\dot{\mathbf{r}}$ is the absolute velocity vector. The mass matrix, \mathbf{M} , is constant, because it depends only on the inertia properties and dimensions of the element. As a result of the constant mass matrix, the centrifugal and Coriolis forces are identically equal to zero. For a three-dimensional beam element, the mass matrix can be written as follows [50]

$$\mathbf{M} = \begin{bmatrix} \frac{13}{35} m \mathbf{I} & \frac{11}{210} l m \mathbf{I} & \frac{7}{20} \rho l Q_z \mathbf{I} & \frac{7}{20} \rho l Q_y \mathbf{I} & \frac{9}{70} m \mathbf{I} & -\frac{13}{420} l m \mathbf{I} & \frac{3}{20} \rho l Q_z \mathbf{I} & \frac{3}{20} \rho l Q_y \mathbf{I} \\ & \frac{1}{105} l^2 m \mathbf{I} & \frac{1}{20} \rho l^2 Q_z \mathbf{I} & \frac{1}{20} \rho l^2 Q_y \mathbf{I} & \frac{13}{420} l m \mathbf{I} & -\frac{1}{140} l^2 m \mathbf{I} & \frac{1}{30} \rho l^2 Q_z \mathbf{I} & \frac{1}{30} \rho l^2 Q_y \mathbf{I} \\ & & \frac{1}{3} \rho l I_{zz} \mathbf{I} & \frac{1}{3} \rho l I_{yz} \mathbf{I} & \frac{3}{20} \rho l Q_z \mathbf{I} & -\frac{1}{30} \rho l^2 Q_z \mathbf{I} & \frac{1}{6} \rho l I_{zz} \mathbf{I} & \frac{1}{6} \rho l I_{yz} \mathbf{I} \\ & & & \frac{1}{3} \rho l I_{yy} \mathbf{I} & \frac{3}{20} \rho l Q_y \mathbf{I} & \frac{1}{30} \rho l^2 Q_y \mathbf{I} & \frac{1}{6} \rho l I_{yz} \mathbf{I} & \frac{1}{6} \rho l I_{yy} \mathbf{I} \\ & & & & \frac{13}{35} m \mathbf{I} & -\frac{11}{210} l m \mathbf{I} & \frac{7}{20} \rho l Q_z \mathbf{I} & \frac{7}{20} \rho l Q_y \mathbf{I} \\ & & & & & \frac{1}{105} l^2 m \mathbf{I} & -\frac{1}{20} \rho l^2 Q_z \mathbf{I} & -\frac{1}{20} \rho l^2 Q_y \mathbf{I} \\ & & & & & & \frac{1}{3} \rho l I_{zz} \mathbf{I} & \frac{1}{3} \rho l I_{yz} \mathbf{I} \\ & & & & & & & \frac{1}{3} \rho l I_{yy} \mathbf{I} \end{bmatrix}, \quad (2.88)$$

symm.

where ρ is the density of the element, \mathbf{I} a 3×3 identity matrix, m the mass of the element and

$$Q_y = \int_A z dA, \quad Q_z = \int_A y dA, \quad I_{yy} = \int_A z^2 dA, \quad I_{zz} = \int_A y^2 dA, \quad I_{yz} = \int_A yz dA$$

are the first and second moments of area.

Externally Applied Forces

The principle of virtual work can be used to develop the vector of the generalized forces [21]. The virtual work caused by the external force vector acting on an arbitrary point on the element can be written as

$$\delta W = \mathbf{F}^T \delta \mathbf{r} = \mathbf{F}^T \mathbf{S} \delta \mathbf{e} = \mathbf{Q}_f^T \delta \mathbf{e}, \quad (2.89)$$

where \mathbf{r} is the position vector of the point of the applied force and $\mathbf{Q}_f = \mathbf{S}^T \mathbf{F}$ the vector of the generalized forces associated with the nodal coordinates. The virtual work caused by distributed forces, such as gravity forces, can be obtained by integrating Equation (2.89) over the volume of the element [55].

In the absolute nodal coordinate formulation, the generalized external forces associated to the external moments are functions of the nodal coordinates. This is because slopes, instead of rotations, are used to define the orientation of the element. The generalized external forces caused by the applied moments can be defined using virtual work. Two formulations are proposed for generalized external moments. Söponen and Mikkola [53]

proposed a coordinate transformation procedure and Sugiyama *et al.* [56] defined an orthogonal triad to the element and derived expressions for the virtual rotations.

Elastic Forces The elastic forces in the absolute nodal coordinate formulation can be derived using a continuum mechanics approach as proposed in References [50, 55, 57]. The continuum mechanics approach is based on the displacement gradient that can be written as follows:

$$\mathbf{D} = \frac{\partial \mathbf{r}}{\partial \mathbf{x}} \left(\frac{\partial \mathbf{X}}{\partial \mathbf{x}} \right)^{-1} = \frac{\partial (\mathbf{S}\mathbf{e})}{\partial \mathbf{x}} \left[\frac{\partial (\mathbf{S}\mathbf{e}_0)}{\partial \mathbf{x}} \right]^{-1}, \quad (2.90)$$

where \mathbf{S} is the shape function matrix, \mathbf{X} the vector of the global coordinates, \mathbf{x} the vector of the local element coordinates and \mathbf{e} and \mathbf{e}_0 are the vectors of the nodal coordinates in the deformed and initial configuration, respectively. The Lagrangian strain tensor, $\boldsymbol{\varepsilon}_m$, can be defined using the right Cauchy-Green deformation tensor as follows [21]:

$$\boldsymbol{\varepsilon}_m = \frac{1}{2} (\mathbf{D}^T \mathbf{D} - \mathbf{I}), \quad (2.91)$$

where \mathbf{I} is a 3×3 identity matrix. The strain energy of the element can be defined using the strain tensor, while the elastic forces can be obtained by using the expression of the strain energy. The continuum mechanics approach is a straightforward method for defining elastic forces. However, in order to achieve accurate results, the finite element should be uniform in all directions, which means that the interpolation functions should be of the same polynomial order in all dimensions. This is not the case in the absolute nodal coordinate beam element. Cubic interpolation is used in the x -direction, while linear interpolation is used in the y - and z -directions.

Recently, Sapanen and Mikkola [53, 54] investigated the accuracy and usability of a continuum mechanics approach in description of the elastic forces of a three-dimensional beam element. They presented three linearized elastic force models that were based on the continuum mechanics approach. A brief description of these models is shown in Table 2.1. It was shown, with the linearized models, that the continuum mechanics description of the elastic forces suffers from the following inaccuracies:

1. The element exhibits a locking phenomena called Poisson's locking or thickness locking in bending. This locking phenomena is described, for instance, in Reference [58]. The locking is caused by the residual transverse normal stresses that contribute to the axial strain. The result is that the element predicts overly small displacements, as shown in Figure 2.2, where the results of the bending convergence test of a tip-loaded cantilever beam are shown.
2. Transverse shear strain distribution over the cross-section is constant, and therefore, a shear correction factor, k_s , must be used.
3. The bending moment distribution along longitudinal coordinate, x , is constant, although a cubic polynomial is used along x .

Table 2.1 Descriptions of the linear elastic force models.

<i>Linear Model I</i>	<i>Linear Model II</i>	<i>Linear Model III</i>
Pure continuum mechanics approach using a linearized strain tensor, in which the quadratic terms are neglected.	Like Model I, but <ul style="list-style-type: none"> – Poisson’s effect is removed, which alleviates the problem of Poisson’s locking – transverse shear correction factors are used to obtain the correct shear strain energy 	Like Model II, but uses <i>Residual Bending Flexibility Correction</i> [48], i.e. a modified shear correction factor, as well. This improves the linear behavior of the element in bending.

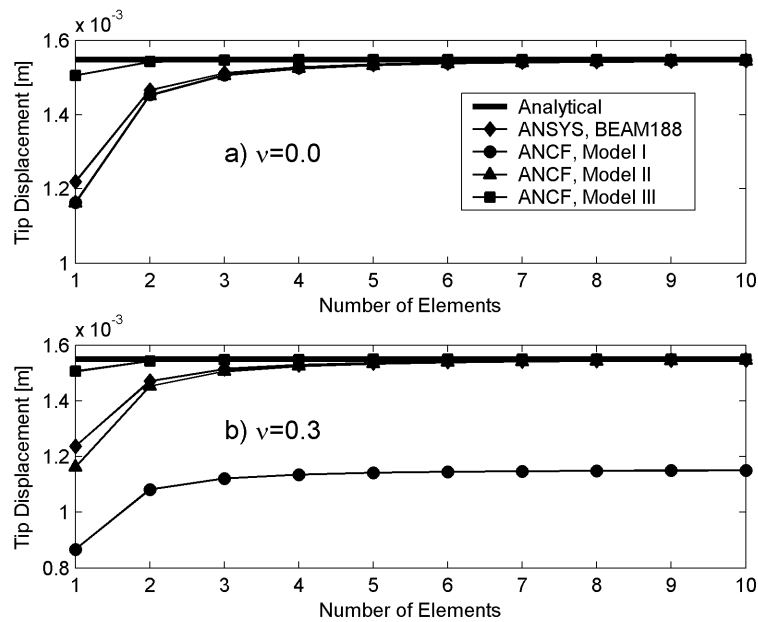


Figure 2.2 The convergence of the different beam models in a tip-loaded cantilever beam model, a) a Poisson’s ratio of 0.0, b) a Poisson’s ratio of 0.3 [53, 54].

The proposed linear elastic force models were verified using several numerical examples. The results were in agreement with the analytical results as well as with the solutions obtained using existing finite element formulation. The reference finite element solutions were obtained using a commercial finite element code ANSYS [36]. The used element type was BEAM188, which is a linear beam element based on a formulation proposed by Simo and Vu-Quoc [41] and Ibrahimbegović [45]. Furthermore, it was shown that the beam element based on the absolute nodal coordinate formulation does not suffer from a phenomenon called shear locking.

It was shown in References [53, 54] that the description of the elastic forces in the absolute nodal coordinate formulation should be modified in order to achieve accurate results. Accuracy can be improved using the proposed linear elastic force models; however, in these models a local element coordinate system must be defined, which complicates the expression of the elastic forces. Furthermore, these models could not totally correct the constant bending moment deficiency.

An accurate expression of the elastic forces in a two-dimensional shear deformable beam is proposed recently by Dufva *et al.* [59]. In the proposed element, a continuum mechanics approach is applied to the exact displacement field of the shear deformable beam. With the

help of Figure 2.3, the displacement of an arbitrary point, P , on the beam can be expressed as

$$\mathbf{u}_P = \mathbf{u}_0 + \mathbf{A}_\psi \mathbf{A}_\gamma \mathbf{y}_P - \mathbf{y}_P, \quad (2.92)$$

where \mathbf{u}_0 is the displacement of the centerline and \mathbf{A}_ψ and \mathbf{A}_γ are the transformation matrices due to the rotation of the centerline and shear angle, respectively. It is assumed that the beam is initially not curved and coincident with the global coordinate system.

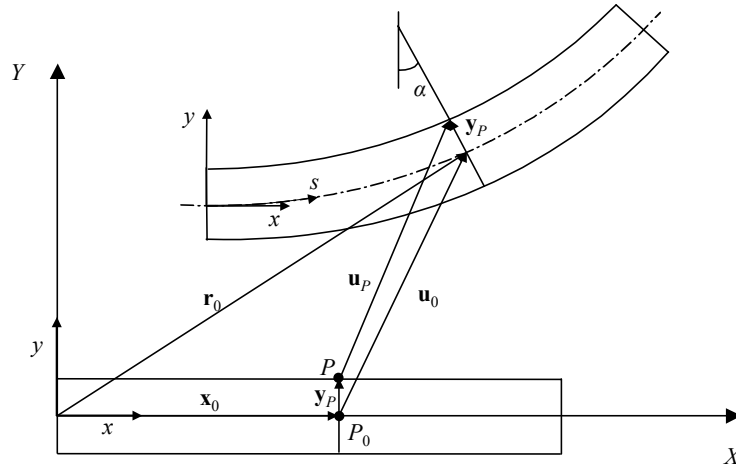


Figure 2.3 The description of an arbitrary point, P , on the beam [59].

The shear angle, γ , can be assumed to be small, $\gamma \ll 1$, as a result of which $\cos \gamma$ can be set to be equal to 1. Using this assumption, the exact displacement field can be written in a simplified form as follows:

$$u = u_0 - y(\sin \psi + \cos \psi \sin \gamma), \quad (2.93)$$

$$v = v_0 + y(\cos \psi - \sin \psi \sin \gamma) - y, \quad (2.94)$$

where ψ is the rotation angle of the centerline. The exact displacement field is rarely used in the finite element formulations of beams. This is simply due to the fact that rotations are used as nodal coordinates and, as a consequence, sine and cosine terms are difficult to describe exactly. On the other hand, the sine and cosine terms that appear in the displacement field can be described by using the absolute nodal coordinate formulation.

In the absolute nodal coordinate formulation, the displacement of the beam centerline can be expressed as follows:

$$\mathbf{u}_0 = \begin{bmatrix} u_0 \\ v_0 \end{bmatrix} = \mathbf{S}(x, 0) \mathbf{e} - \begin{bmatrix} x \\ 0 \end{bmatrix}. \quad (2.95)$$

The shape function matrix, \mathbf{S} , which contains cubic terms in x and linear terms in y , can be found in References [55, 59]. The rotations of the beam centerline can be described using the displacements of the centerline as follows:

$$\cos \psi = \frac{1 + u'_0}{\sqrt{(1 + u'_0)^2 + v'_0{}^2}}, \quad (2.96)$$

$$\sin \psi = \frac{v'_0}{\sqrt{(1 + u'_0)^2 + v'_0{}^2}}, \quad (2.97)$$

where $(-)'$ denotes differentiation with respect to x . Shear deformation is expressed in the displacement field using $\sin \gamma$, which can be expressed using the slope vectors, as follows:

$$\sin \gamma = -\frac{\mathbf{r}_x^T \mathbf{r}_y}{|\mathbf{r}_x| |\mathbf{r}_y|}, \quad (2.98)$$

where $\mathbf{r}_\alpha = \partial \mathbf{r} / \partial \alpha$, $\alpha = x, y$. However, the use of Equation (2.98) leads to a constant bending strain distribution along the longitudinal coordinate x . Therefore, a mixed interpolation technique is used for shear deformation to achieve the linear distribution of the bending strain. It follows that

$$\sin \gamma \approx (\sin \gamma)_I (1 - \xi) + (\sin \gamma)_J \xi, \quad (2.99)$$

where $(\sin \gamma)_I$ and $(\sin \gamma)_J$ are the displacements of the shear strains at the nodal points I and J of the element, respectively.

If the beam is initially not curved and coincident with the global coordinate system, the axial and shear strain components, including the nonlinear terms, can be expressed as

$$\varepsilon_{xx} = \frac{\partial u}{\partial x} + \frac{1}{2} \left[\left(\frac{\partial u}{\partial x} \right)^2 + \left(\frac{\partial v}{\partial x} \right)^2 \right], \quad (2.100)$$

$$\varepsilon_{xy} = \frac{1}{2} \left(\frac{\partial u}{\partial y} + \frac{\partial v}{\partial x} + \frac{\partial u}{\partial x} \frac{\partial u}{\partial y} + \frac{\partial v}{\partial x} \frac{\partial v}{\partial y} \right). \quad (2.101)$$

In the beam elements based on the absolute nodal coordinate formulation, the cross-section is allowed to deform. For this reason, the transverse normal strain must be defined; however, the simplest form of strain is used:

$$\varepsilon_{yy} = (1 - \xi) \mathbf{r}_y|_{x=0} + \xi \mathbf{r}_y|_{x=l} - 1, \quad (2.102)$$

By using the above strain definitions and neglecting the Poisson's effect, the strain energy can be written as

$$U = \frac{1}{2} \int_V \left(E \varepsilon_{xx}^2 + E \varepsilon_{yy}^2 + 4k_s G \varepsilon_{xy}^2 \right) dV, \quad (2.103)$$

where E is Young's modulus, G the shear modulus and k_s the shear correction factor. The vector of the elastic forces, \mathbf{Q}_e , can be defined using the strain energy, U , as follows:

$$\mathbf{Q}_e = -\left(\frac{\partial U}{\partial \mathbf{e}}\right)^T \quad (2.104)$$

As shown in Reference [59], this element is capable of accurately predict the nonlinear deformations and does not seem to suffer from shear locking or Poisson's locking. The capability of the element to model highly nonlinear behavior was demonstrated in an example, in which a cantilever beam was bent into a full circle with a moment load. A full circle was achieved using only four elements, as is shown in Figure 2.4. Due to the nonlinear description of strain, the nonlinear geometric stiffening terms are automatically included in this formulation.

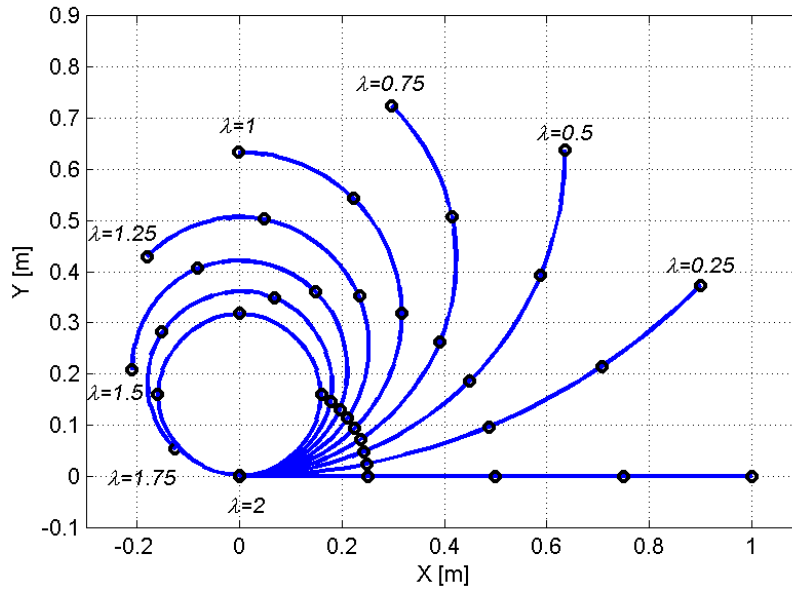


Figure 2.4 A cantilever beam subjected to a tip moment. The external moment, M_z , applied at the end of the beam is $\lambda\pi EI_{zz}/l$.

The absolute nodal coordinate formulation is a very promising method for the analysis of the nonlinear deformation in multibody systems. The elastic forces of a three-dimensional shear deformable beam should be derived using the exact displacement field and the nonlinear strain tensor. Efficient time integration methods and material nonlinearity are topics that warrant further research. In conclusion, it can be stated that the absolute nodal coordinate formulation is a potential method for the geometrical and material nonlinear analysis of high-speed rotors.

3 MODELING OF BALL BEARINGS

Rolling element bearings generate vibrations, even when the geometry of bearing elements is ideal. Varying compliance vibration is caused by the varying orbital position of the balls; this movement leads to fluctuations in the stiffness of the bearing. Aktürk *et al.* [60] studied vibrations of a geometrically perfect angular contact ball bearing using a three-degree-of-freedom model. They showed that in the case of an ideal bearing, the vibrations occur at the ball passage frequency. They reported that the amplitudes of these vibrations are considerably reduced when the number of balls and the preload of the bearing are properly selected. They also pointed out that the system might resonate at a fraction of its natural frequency. This can be explained by the ball passage frequency that is defined as the cage speed times the number of rolling elements. Tiwari *et al.* [61, 62] studied the effect of the ball bearing clearance on the dynamic response of a rigid rotor. In [61], the varying compliance effect was the only excitation in the simulation model. In [62], the effect of the unbalance of the rigid rotor was also included in the simulation model. Tiwari *et al.* noticed that the stiffness of the bearing increases as the clearance decreases. They also noted that the nonlinearity of the ball bearing rotor system increases when the bearing clearance increases. They, furthermore, discovered that the nonlinearity of the system results in subharmonic frequencies as well as in sum and difference combinations of the rotational and varying compliance frequencies.

The main source of bearing-induced vibration are defects in the bearing components. Bearing defects can be classified as being distributed and localized defects. Distributed defects, such as surface roughness, waviness and misaligned races, are caused by the manufacturing process or improper installation. Localized defects, such as cracks, pits and spalls, are caused by fatigue damage on the rolling surfaces. When a localized defect passes its mating surface, a short force pulse is generated. Under a constant rotation speed, these pulses are generated at a nominal defect frequency [63].

The waviness of the rolling surfaces has been studied by several authors [64-70]. Gupta [64] studied the effect of the out-of-roundness of the bearing elements on the performance of ball bearings. He concluded that the amplitude of out-of-roundness has to be large before notable changes can be observed in the performance of a bearing; however, bearing-induced vibrations were not considered in Gupta's study. Wardle [65, 66] studied the vibrations caused by waviness in a thrust-loaded ball bearing and used a simplified approximation of Hertzian contact instead of a fully nonlinear contact model. Moreover, the applied radial loads were assumed to be negligible in comparison to the thrust load. Wardle concluded that not all waviness orders generate vibrations. For outer ring waviness, waviness orders, equal to integer multiples times the number of balls (nz), generate axial vibration, and waviness orders of $nz \pm 1$ generate radial vibration at the ball passage outer ring frequency and its multiples. Inner ring waviness leads to a more complex spectrum than does outer ring waviness. Axial vibration occurs at the ball inner ring passage frequency f_{bpir} , while radial vibration occurs at frequencies $f_{bpir} \pm f_s$, where f_s is the shaft frequency. Wardle also found that waviness on two or more component surfaces interacts and generates sideband frequencies. Yhland [67] developed a linear stiffness matrix for ball bearings and described waviness in the form of external forces. The bearing under investigation was assumed to operate at moderate speeds and, thus, the centrifugal forces of the balls were ignored. Yhland listed the frequencies that were excited by the different orders of waviness of the rolling surfaces. Aktürk [68] studied inner ring waviness and found that for relatively low wave orders, the predominant vibration occurs at the frequency that is the number of waves times the rotational speed of the inner ring. In

detailed waviness studies, the contact stiffness coefficient was considered to be constant and linear. Furthermore, the bearings were preloaded in order to ensure continuous contact between all the balls and the raceways. Lynagh *et al.* [69] studied the spindle vibrations in a machine tool both experimentally and analytically. The spindle was supported by two pairs of angular contact ball bearings. The proposed analytical bearing model ignored the lubricant film and angular misalignments. The model included the waviness of the inner and outer ring as well as the waviness of the balls. Also, off-sized balls were taken into account in the analytical model that was able to predict the principal bearing-induced vibration frequencies as well as the sidebands caused by the interaction of the outer race waviness, ball size or waviness and inner race waviness. Some of these sideband frequencies corresponded to the experimental spectrum, but the authors noted that a broader spectral analysis should be carried out to pinpoint the exact cause of these vibrations. Jang and Jeong [70] presented a nonlinear model of a ball bearing for the analysis of waviness. They presented a five-degree-of-freedom general rotor bearing system where a rigid rotor was supported by two or more angular contact ball bearings. They reported harmonic frequencies arising from the nonlinear load-deflection characteristics of the ball bearing. Sideband frequencies resulting from the nonlinearity of the waviness interaction between the axial and radial directions were also observed.

Tandon and Choudbury [71] studied the ball bearing vibrations caused by a localized defect. Their model included flexural rings that were modeled using the mode summation method. The defects were described using finite width pulses. The results showed that in the case of both axial and radial loads, outer race defects generate vibrations in the outer race defect frequency and its multiples. In the case of axial loads, inner race defects cause vibrations at the inner race defect frequency and its multiples. When radial loading is considered, the frequency spectrum has sidebands at frequencies $i \cdot f_{bpir} \pm j \cdot f_s$, where i and j are integers ($i, j = 1, 2, \dots$). In other words, the sidebands are distributed around the inner ring defect frequency and its integer multiples in such a way that the sidebands are integer multiples of the shaft frequency. However, in the case of inner race defects, this model could not predict the peaks at the shaft frequency and its multiples. These peaks are found in the experimental spectrum [72]. Tandon and Choudbury concluded that the amplitude level of the vibrations increases when the load increases. They also noted that the amplitude is affected by the shape of the generated pulse.

Lee and Lee [73] studied misalignments in a ball bearing shaft system. They found that a misalignment affects the whirling orbits of the rotor. They found, both analytically and experimentally, that the natural frequency of a misaligned rotor system in the direction of misalignment increases, i.e. the stiffness of the bearing in that direction increases.

The above-mentioned bearing models considered only a simple bearing system, made up of either only one bearing or a simple rotor with two bearings. However, general ball bearing modules, which can be used in general-purpose multibody or rotor dynamics computer codes, are not usually available. Keskiniva [19] proposed a ball bearing model which includes five degrees of freedom; he did not, however, consider any non-idealities or the effect of the bearing clearance. The effect of the low-order waviness of the bearing rings is not often considered in ball bearing literature. Waviness orders of 2, 3 and 4 can lead to subcritical superharmonic resonances. In this case, the natural vibration mode of the rotor is excited when the rotation speed is a fraction of the natural frequency of the system. In some applications, such as paper machines, 1/2, 1/3, and 1/4 subcritical resonances are of practical significance, since they can influence process quality. In order to study the 2X, 3X, and 4X superharmonic behavior of the roll, the impulses caused by bearings must be taken into consideration.

The objective of this section of the study is to present a general-purpose ball bearing model that acts as an interface element between the rotor and the supporting structure. Ball bearings are usually components in an assembly that can consist of flexible and rigid bodies. These components interact with each other dynamically, which should be accounted for. The proposed ball bearing model has six degrees of freedom and incorporates nonlinear Hertzian contact deformation as well as the thickness of the lubricant film between the balls and races. The waviness of the rings and local defects in the inner and outer ring can be incorporated into the ball bearing model as non-idealities. The analytical model of the ball bearing is presented in this section. In Chapter 4, the simulation results for an electric motor supported by two ball bearings are presented and discussed.

3.1 Modeling Assumptions and Contact Calculation

Modeling Assumptions A single ball bearing consists of a number of parts. Describing each component can lead to simulation models that have a large number of degrees of freedom. However, the ball bearing calculation should be computationally efficient enough in order for it to be used in simulations of complete machines. Therefore, the proposed ball bearing model has been simplified as follows:

1. The centrifugal forces acting on the balls are neglected.
2. The cage of the bearing is assumed to be ideal; i.e. it holds the balls in their predefined positions.
3. The bending deformation in the rings is assumed to be negligible. It is assumed that only local deformation occurs in the contact area.
4. The movement of the cage is based on the geometrical dimensions of the bearing; therefore, it is assumed that no slipping or sliding occurs between the components of the bearing.

The proposed ball bearing model calculates the bearing forces and moments caused by the relative movement and velocity between the inner and outer ring. Regardless of the above-mentioned simplifications, the force-deflection relationship of the proposed ball bearing model is fairly complex.

Elliptical Contact Conjunction Two solids that have different radiuses of curvature in two directions (x and y in Figure 3.1) are in point contact when no load is applied to them. When the two solids are pressed together by a force F , the contact area is elliptical. In the case of ball bearings, the contact conjunction is elliptical, as shown in Figure 3.1. The radius of the contact curvature is defined as being positive when the surface is convex and negative when the surface is concave.

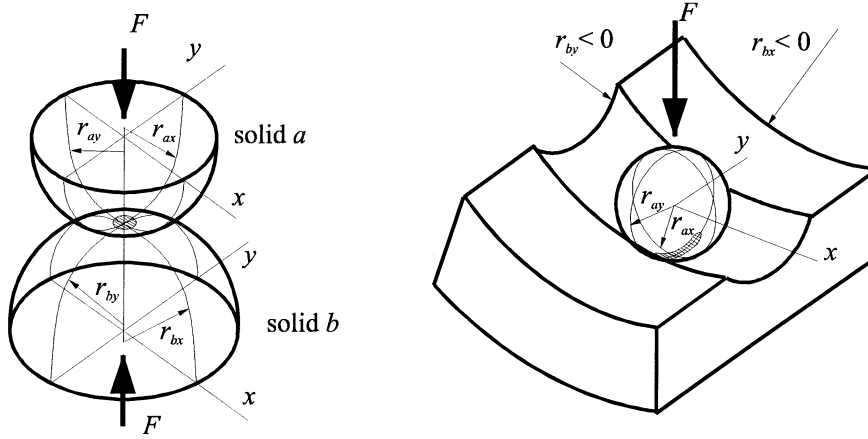


Figure 3.1 Elliptical contact conjunctions [19].

The geometry between two solids (a and b), which are in contact with each other, can be expressed in terms of the curvature sum, R , and difference, R_d , as follows [74]

$$\frac{1}{R} = \frac{1}{R_x} + \frac{1}{R_y} \quad (3.1)$$

$$R_d = R \left(\frac{1}{R_x} - \frac{1}{R_y} \right), \quad (3.2)$$

where

$$\frac{1}{R_x} = \frac{1}{r_{ax}} + \frac{1}{r_{bx}} \quad (3.3)$$

$$\frac{1}{R_y} = \frac{1}{r_{ay}} + \frac{1}{r_{by}} \quad (3.4)$$

Variables R_x and R_y represent the effective radiuses of the curvatures in the principal x and y planes. When a normal load is applied to the two solids, the point expands to an ellipse with a_e being the semimajor and b_e the semiminor axis. The ellipticity parameter can be defined as [75]

$$k_e = \frac{a_e}{b_e} \quad (3.5)$$

The ellipticity parameter can be written as a function of the curvature difference, R_d , and the elliptic integrals of the first and second kind, ξ and ζ respectively, as follows [74]:

$$k_e = \left[\frac{2\xi - \zeta(1 + R_d)}{\zeta(1 - R_d)} \right]^{1/2}, \quad (3.6)$$

where

$$\xi = \int_0^{\pi/2} \left[1 - \left(1 - \frac{1}{k_e^2} \right) \sin^2 \varphi \right]^{-1/2} d\varphi, \quad (3.7)$$

$$\zeta = \int_0^{\pi/2} \left[1 - \left(1 - \frac{1}{k_e^2} \right) \sin^2 \varphi \right]^{1/2} d\varphi, \quad (3.8)$$

where φ is an auxiliary angle. It can be seen from Equations (3.6) - (3.8) that the solution of the ellipticity parameter and elliptic integrals requires an iteration procedure. For this reason, Brewe and Hamrock [76] used one-point numerical iteration and curve fitting techniques and obtained the following approximation formulae for the ellipticity parameter, k_e , and elliptical integrals of the first and second kind, ξ and ζ respectively, as shown below:

$$\bar{k}_e = 1.0339 \left(\frac{R_y}{R_x} \right)^{0.6360}, \quad (3.9)$$

$$\bar{\xi} = 1.0003 + 0.5968 \frac{R_x}{R_y}, \quad (3.10)$$

$$\bar{\zeta} = 1.5277 + 0.6023 \ln \left(\frac{R_y}{R_x} \right). \quad (3.11)$$

The contact stiffness coefficient for the elliptical contact conjunction can be calculated using the fitted expressions for the elliptic integrals and ellipticity parameter as follows:

$$K_c = \pi \bar{k}_e E' \sqrt{\frac{R \bar{\xi}}{4.5 \bar{\zeta}^3}}, \quad (3.12)$$

where the effective modulus of elasticity, E' , is defined as

$$\frac{1}{E'} = \frac{1}{2} \left(\frac{1 - \nu_a^2}{E_a} + \frac{1 - \nu_b^2}{E_b} \right), \quad (3.13)$$

where E is the modulus of elasticity, ν Poisson's ratio and subscripts a and b refer to solids a and b , respectively.

Elastohydrodynamic (EHL) Lubrication

The theory of elastohydrodynamic (EHL) lubrication must be taken into account when modeling ball bearings that run at high operational speeds. In ball bearings, a lubricant film forms between the contacting solids. The thickness of the film depends on the surface velocities, geometries and material properties of the solids as well as on the properties of the lubricant. The thickness of the film also depends on the applied pressure; however, this dependency is infinitesimal. Typically, it is assumed that the lubricant film is as stiff as the contacting solids. Therefore, hydrodynamics and contact elasticity are strongly coupled when considering the dynamic performance of ball bearings. The solution of the elastohydrodynamic contact problem requires the simultaneous solution of the elasticity problem and the Reynolds equation. The proposed ball bearing model requires information on the thickness of the lubricant film in contact. Hamrock and Dowson [77] have developed equations for the minimum and central film thickness; in their study, the minimum film thickness was found to be at the outlet zone of the rolling contact. It is important to identify the minimum film thickness in

order to guarantee adequate lubrication; however, the proposed model is based on the use of the central film thickness which, for the elliptical contact problem, can be approximated as

$$h_0 = 2.69R_x\bar{U}^{0.67}\bar{G}^{0.53}\bar{W}^{-0.067}\left(1 - 0.61e^{-0.73\bar{k}_c}\right), \quad (3.14)$$

where $\bar{U} = (\eta_0 U)/(2E'R_x)$ is a dimensionless speed parameter, U the mean of the surface velocities, $\bar{G} = \alpha E'$ a dimensionless material parameter and $\bar{W} = F/(E'R_x^2)$ a dimensionless load parameter.

High pressures in elastohydrodynamic contact change the viscosity properties of the lubricant. For isothermal conditions, this variation can be described by the Barus formula as follows [74]:

$$\eta = \eta_0 e^{\alpha p}, \quad (3.15)$$

where p is the pressure in N/m^2 and η_0 the absolute viscosity at zero pressure in a constant temperature in Ns/m^2 . Parameter α is a temperature-dependent pressure-viscosity coefficient in m^2/N .

3.2 Ball Bearing Kinematics

Figure 3.2 shows the key dimensions of a deep groove ball bearing. The bearing pitch diameter is the mean of the inner and outer race contact diameters and can be defined as

$$d_m = R_{in} + R_{out} \quad (3.16)$$

Correspondingly, the diametral clearance is defined as

$$c_d = 2(R_{out} - R_{in} - d). \quad (3.17)$$

The diametral clearance can be seen as the maximum distance that one race can move freely diametrically. In practice, both the inner and outer race radii are often unknown. On the other hand, the pitch diameter and diametral clearance are usually known. For this reason, the pitch diameter and diametral clearance are given as input data for the proposed model; consequently, the race contact radii are calculated from these parameters.

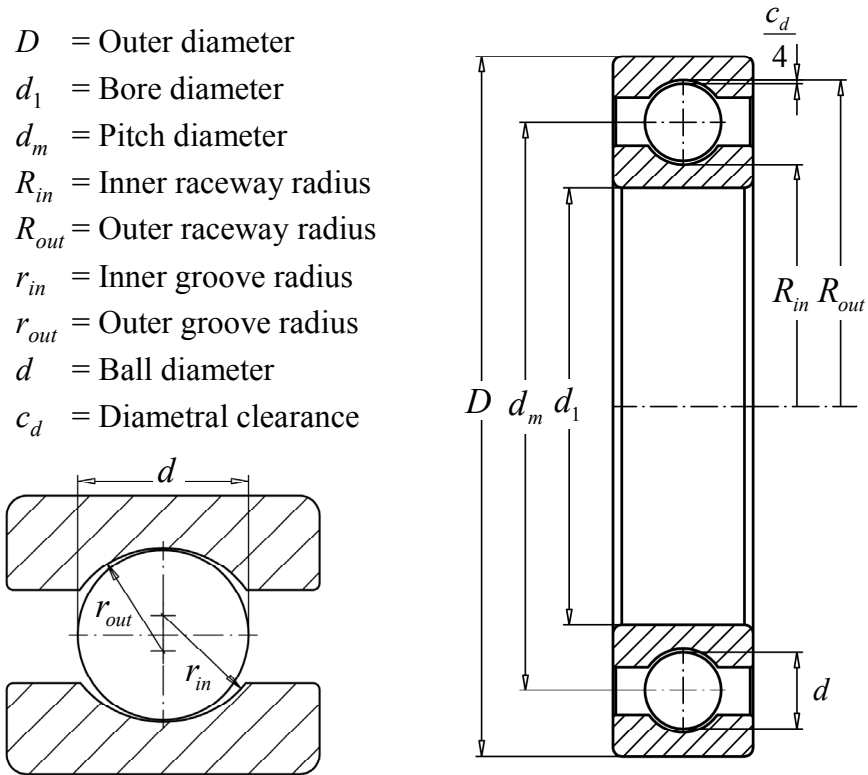


Figure 3.2 The dimensions of a ball bearing.

Race conformity is a measure of the geometrical conformity of the race and the ball in a plane that passes through the center of the bearing and is transverse to the race (shown in Figure 3.2). Race conformity is defined as the ratio between the race groove radius and ball diameter, as follows:

$$R_r = \frac{r}{d} \quad (3.18)$$

One can note that perfect conformity is equal to 0.5. In general, good conformity between the race and the ball reduces the maximum contact pressure. Reducing the contact pressure reduces fatigue damage to the rolling surfaces; however, good conformity increases the generation of frictional heat. For these reasons, race conformity in modern ball bearings ranges between 0.51...0.54, with 0.52 being the most common value. Since the contact radius in the circumferential direction in the inner race (R_{in}) is smaller than the radius in the outer race (R_{out}), the race conformity ratio for the outer race is usually designed to be slightly larger than that for the inner race. This is done in order for the curvature sum of the inner race to be approximately equal to that of the outer race. This, in turn, leads to similar maximum contact stresses in the inner and outer race [74].

The elliptical contact conjunction can be described by the curvature sum, R , and difference, R_d , as discussed in the previous section. For ball bearings, these quantities can be calculated from the dimensions shown in Figure 3.2. The radiuses of the curvature for the ball-inner-race contact can be written as

$$r_{ax}^{in} = r_{ay}^{in} = \frac{d}{2}, \quad (3.19)$$

$$r_{bx}^{in} = \frac{d_m - \left(d + \frac{c_d}{2}\right) \cos \phi}{2 \cos \phi} \approx \frac{d_m - \left(d + \frac{c_d}{2}\right)}{2} = R_m, \text{ when } \phi \approx 0, \quad (3.20)$$

$$r_{by}^{in} = -r_{in} = -R_r^{in} d, \quad (3.21)$$

where ϕ is the contact angle of the bearing. In deep groove ball bearings, the contact angle is usually close to zero, and therefore, the effect of the contact angle on the contact radiuses can be neglected without a significant loss in accuracy. The radiuses of curvature for the ball-outer-race contact can be written as

$$r_{ax}^{out} = r_{ay}^{out} = \frac{d}{2}, \quad (3.22)$$

$$r_{bx}^{out} = -\frac{d_m + \left(d + \frac{c_d}{2}\right) \cos \phi}{2 \cos \phi} \approx -\frac{d_m + \left(d + \frac{c_d}{2}\right)}{2} = -R_{out}, \text{ when } \phi \approx 0, \quad (3.23)$$

$$r_{by}^{out} = -r_{out} = -R_r^{out} d. \quad (3.24)$$

By substituting these radiuses into Equations (3.1) to (3.4), the curvature sum and difference can be obtained.

3.3 Elastic Deformation in Ball Bearings

In a single ball element, the total deflection is the sum of the contact deflections between the ball and the inner and outer races. The deflection between the ball and the race can be approximated as [19]

$$\delta_0 = \left(\frac{F}{K_c}\right)^{\frac{2}{3}}, \quad (3.25)$$

where F is the normal load and K_c is defined by Equation (3.12). The total stiffness coefficient, K_c^{tot} , involves both the inner and outer race contacts and can be, thus, expressed as

$$K_c^{tot} = \left[\left(K_c^{in}\right)^{-\frac{2}{3}} + \left(K_c^{out}\right)^{-\frac{2}{3}} \right]^{-\frac{3}{2}}. \quad (3.26)$$

Ball bearing forces can be calculated from the relative displacements between the rings. In Figure 3.3, the shaft, i.e. inner race, is given eccentricities e_x and e_y in the X - and Y -directions. Thus, the corresponding radial eccentricity in the direction of ball i can be stated as

$$e_i^r = e_x \cos \beta_i + e_y \sin \beta_i, \quad (3.27)$$

where β_i is the attitude angle (azimuth angle) of ball i . The axial displacement at ball i is defined as

$$e_i^a = e_z - \left(-\gamma_x \sin \beta_i + \gamma_y \cos \beta_i\right) \left(R_{in} + r_{in}\right), \quad (3.28)$$

where e_z is the axial shift and γ_x and γ_y are the misalignments between the inner and outer race, respectively.

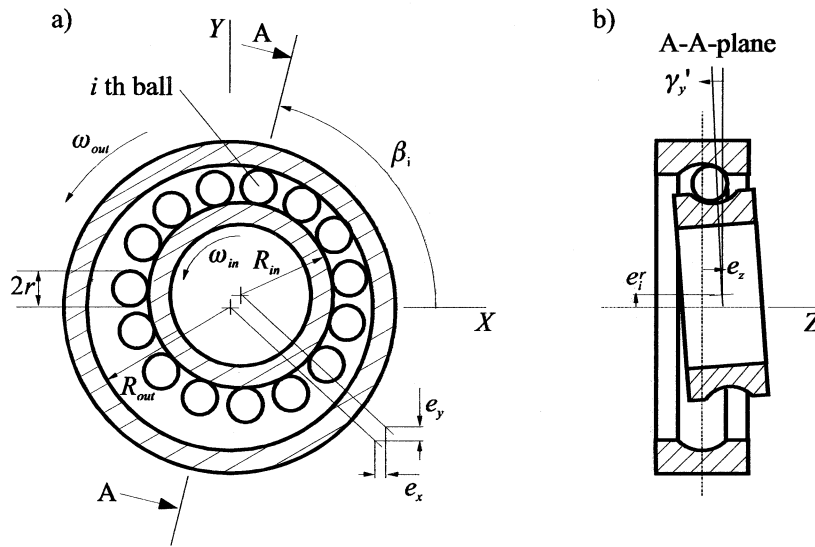


Figure 3.3 (a) The axial and (b) transverse cross-section in the A-A-plane of a ball bearing [19].

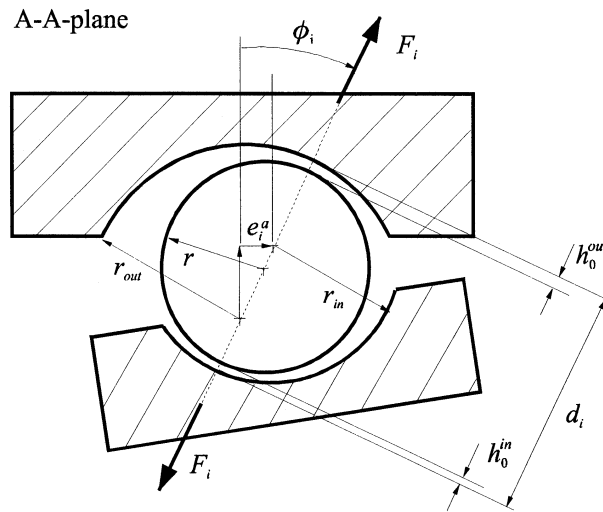


Figure 3.4 The cross-section of a ball bearing in the A-A-plane [19].

Figure 3.4 shows the cross-section of a ball bearing in the A-A-plane (Figure 3.3). The contact angle in each roller element can be defined as

$$\phi_i = \tan^{-1} \left(\frac{e_i^a}{R_{in} + r_{in} + e_i^r - R_{out} + r_{out}} \right) \quad (3.29)$$

Using Figure 3.4, the distance between the race surfaces along the line of contact can be expressed as

$$d_i = r_{out} + r_{in} - \frac{R_{in} + r_{in} + e_i^r - R_{out} + r_{out}}{\cos \phi_i} \quad (3.30)$$

The total elastic deformation can be calculated as follows

$$\delta_i^{tot} = 2r + h_0^{in} + h_0^{out} - d_i, \quad (3.31)$$

where h_0^{in} and h_0^{out} are the lubricant film thicknesses between the contact surfaces. Note that this equation holds for a bearing with perfect geometry only. The contact force acting on ball i can be obtained as follows:

$$F_i = K_c^{tot} (\delta_i^{tot})^{1.5}, \quad (3.32)$$

where the total stiffness coefficient is determined by Equation (3.26). The resultant bearing forces acting upon the shaft in the X -, Y - and Z -directions can be summarized as follows:

$$F_X = - \sum_{i=1}^z F_i \cos \phi_i \cos \beta_i, \quad (3.33)$$

$$F_Y = - \sum_{i=1}^z F_i \cos \phi_i \sin \beta_i, \quad (3.34)$$

$$F_Z = - \sum_{i=1}^z F_i \sin \phi_i, \quad (3.35)$$

and, accordingly, the bearing moments can be written as

$$T_X = - \sum_{i=1}^z F_i (R_{in} + r) \sin \phi_i \sin \beta_i, \quad (3.36)$$

$$T_Y = - \sum_{i=1}^z F_i (R_{in} + r) \sin \phi_i (-\cos \beta_i). \quad (3.37)$$

Summation i includes only those balls in which elastic compression occurs, i.e. $\delta_i^{tot} > 0$.

Because the film thickness is a function of the contact force, it is not directly solvable. On the other hand, it can be seen from Equation (3.14) that the film thickness is practically independent of the load. For example, if the load increases by 50 % and the other parameters in Equation (3.14) are kept constant, the film thickness decreases by only 2.8 %. This means that the error in the film thickness is small, even if an approximate value of the contact force is used in the calculation. Keskiniva [19] proposed that the film thickness be regarded as a constant with respect to the applied load. Using this approach, the film thickness can be determined from the maximum contact force under a nominal load. The maximum contact force in a ball bearing can be obtained from Stribeck's equation as follows:

$$F_{max} = \frac{z_F}{z} F_{nominal}, \quad (3.38)$$

where z is the number of rolling elements. In Stribeck's approach, the constant z_F is assumed to be 4.37 under a purely radial load and zero clearance. For a nominal bearing

clearance, the constant z_F is usually approximated to be 5 [78]. In the proposed model, the nominal load is replaced by the magnitude of the total bearing force which varies according to time. This differs from Keskiniva's approach in which a constant load is used for F_{nominal} .

The film thickness depends mainly on the surface velocities between the mating surfaces. In the case of pure rolling, the velocity at which the ball surface and inner race surface, as well as the ball surface and outer race surface, move with respect to each other can be written as [79]

$$U_{in} = U_{out} = \frac{d_m^2 - d^2}{4d_m} |\omega_{out} - \omega_{in}| \quad (3.39)$$

It should be noted that the attitude angle of a roller element is not constant but changes while the inner race rotates with respect to the outer race. This change can be described as follows:

$$\beta_i = \beta_i^0 + \frac{\theta_{in} R_{in} + \theta_{out} R_{out}}{2(r + R_{in})}, \quad (3.40)$$

where θ_{in} and θ_{out} are the rotation angles of the inner and outer races, respectively, and β_i^0 is the initial attitude angle of ball i . This equation leads to a nonlinear force-displacement relation that is also known as the varying compliance effect.

Using the above-introduced equations, three bearing force components, F_X , F_Y , F_Z , and torques T_X and T_Y around the X - and Y -axes can be calculated from the relative displacement and angular velocity of the rings. However, the proposed model has six degrees of freedom and the remaining torque around bearings rotation axis is caused by friction. In general, the friction forces of ball bearings are complex to model analytically. Therefore, this work adopts an empirical approach to friction torque that is described in References [78, 80]. In this method, the total friction torque consists of viscous friction torque, load-dependent friction torque and seal friction. A detailed description of the bearing friction torque used in the model can be found in Reference [81].

3.4 Ball Bearing Damping

Dietl *et al.* [82] studied the damping of rolling element bearings both experimentally and theoretically. They listed major sources of bearing damping as follows:

- Lubricant film damping in rolling contacts.
- Material damping due to the Hertzian deformation of the rolling bodies.
- Damping in the interface between the outer ring and the bearing housing. This damping increases when the clearance between the outer ring and the bearing housing increases.

Experimental measures showed that bearing damping decreases when the rotation speed increases. They found that the damping coefficients for angular contact ball bearings of type 7309 ranged between 0.4 and 0.8 Ns/mm. Mitsuya *et al.* [83] experimentally studied the damping of a type 6200 ball bearing. The experimental damping ratios ranged between 2 and 4 % and the damping coefficients between 0.15 and 0.35 Ns/mm. Aini *et al.* [84] studied the vibrations of a spindle that was supported by two lubricated angular contact ball bearings. The ball-to-race contacts were modeled using nonlinear spring-dampers. The damping contribution to the bearing model was derived from the squeeze action of the

lubricant film. The results were compared with those obtained from dry-contact models. The damping of the lubricant film was found to be moderate. The damping ratio of the spindle system was found to be 0.0035. According to Krämer [2], the damping of rolling element bearings ranges between

$$c_b = (0.25 \dots 2.5) \cdot 10^{-5} k_{lin}, \quad (3.41)$$

where k_{lin} is the linearized stiffness of the bearing in N/ μ m. Simple linear viscous damping is adopted in the proposed ball bearing model. Figure 3.5 shows the damping coefficient of a type 6010 ball bearing as a function of the applied radial load. The damping values are obtained by multiplying the linearized stiffness values by a constant, $0.25 \cdot 10^{-5}$, in accordance with Equation (3.41). Due to the fact that the damping of the bearing is relatively small, a constant damping value, which is based on the average load, is used in the proposed model.

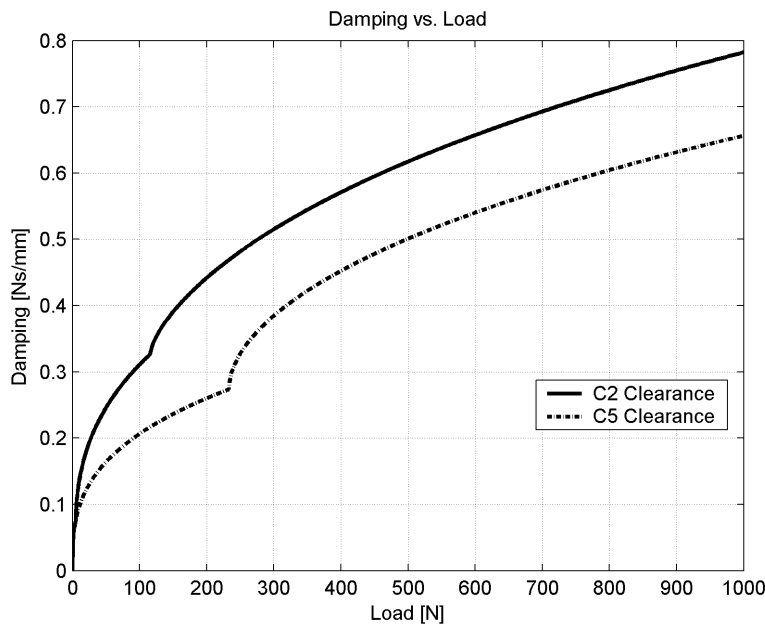


Figure 3.5 The damping coefficient of a type 6010 ball bearing with C2 and C5 clearances. The rotation speed used in the calculation is 15 Hz, while the other parameters can be found in Table 4.2.

3.5 Non-Idealities

Bearing-induced vibration is caused mainly by the non-idealities of the bearing, such as the waviness of the rings, misalignments and bearing defects. In order to study the vibration responses caused by these non-idealities, they must be properly accounted for in the model. Bearing non-idealities are modeled as a variation in the deformation of each ball-race contact. This approach enables combinations of various non-idealities to be modeled; nevertheless, bearing misalignments do not require any modifications to be made to the proposed bearing model. Because the calculation of the bearing forces is based on the relative displacements and rotations between the rings, the misalignments can be modeled by defining the initial offset to the relative displacements. The modeling of the waviness and localized defects of the rings is described in the following sections.

3.5.1 Waviness of the Bearing Rings

The roundness profile of a bearing ring can be presented as a Fourier cosine series, as follows:

$$R(\theta) = \sum_{m=1}^n A_m \cos(m\theta + \phi_m), \quad (3.42)$$

where A_m is the amplitude, ϕ_m the phase angle of m^{th} -order waviness and θ the angular coordinate of the bearing ring. The amplitudes and phase angles of the harmonic waviness components can be obtained from measurements by analyzing the results with the FFT (Fast Fourier Transform).

The effect of the waviness of the bearing ring can be included in the elastic deformation of ball i , Equation (3.31), as follows:

$$\Delta_i^{total} = \delta_i^{tot} + \sum_{m=1}^n A_m^{in} \cos[m(\beta_i - \theta_{in}) + \phi_m^{in}] + \sum_{m=1}^n A_m^{out} \cos[m(\beta_i - \theta_{out}) + \phi_m^{out}], \quad (3.43)$$

where the first summation describes the waviness of the inner ring and second summation that of the outer ring.

3.5.2 Localized Defects

In the proposed model, the defects of the bearing are added to the total deformation of the ball. To this end, the shape of the defect is described using two parameters; the length (L_{defect}) and height (h_{defect}) of the defect. A bearing defect generates a pulse when the ball passes over it. This means that a variation in the total deformation occurs when the attitude angle of ball i is equal to that of the defect in a ring. This can be expressed as follows:

$$\beta_i - \theta_{in} - \phi_{defect} = -n2\pi, \quad n = 0, 1, \dots, \quad (3.44)$$

where ϕ_{defect} is the position angle of the defect. In order to trigger this condition, the properties of the tangent and *STEP* functions are used. The *STEP* function approximates a Heaviside step function with cubic polynomials. The *STEP* function is continuous for first derivatives and can be written as [24]

$$STEP(g, g_0, h_0, g_1, h_1) = \begin{cases} h_0 & ; g \leq g_0 \\ h_0 + \Delta h \cdot \Delta g^2 (3 - 2\Delta g) & ; g_0 < g < g_1, \\ h_1 & ; g \geq g_1 \end{cases} \quad (3.45)$$

where $\Delta h = h_1 - h_0$ and $\Delta g = (g - g_0)/(g_1 - g_0)$. Variable g is an independent variable, while g_0 and g_1 are the starting and ending values of the step. Correspondingly, h_0 and h_1 are the initial and final values of the function. A bearing defect alters the total deformation of ball i and can be calculated by substituting the following values into the *STEP* function:

$$\Delta_{defect} = STEP(g, g_0, h_0, g_1, h_1), \quad (3.46)$$

where

$$g = - \left| \tan \left(\frac{1}{2} (\beta_i - \theta_{in} - \phi_{defect}) \right) \right|, \quad (3.47)$$

$$g_0 = - \left| \tan \left(\frac{L_{defect}}{4R_{in}} \right) \right|, \quad h_0 = 0, \quad (3.48)$$

$$g_1 = - \left| \tan \left(\frac{L_{defect}}{8R_{in}} \right) \right|, \quad h_1 = -h_{defect}, \quad (3.49)$$

During the analysis, the attitude angle of ball i and the rotation angle of the ring increases continuously, i.e. these angles are not limited to the range of $0 \dots 2\pi$. The value of the tangent function passes through zero at angle π and its integer multiples. By multiplying the absolute value of the tangent by -1 , one can obtain a peak that can be triggered by the *STEP* function. By using the length of the defect and the radius of the ring, one can calculate the angle occupied by the defect on the ring. Figure 3.6 shows an example of the shape of an inner ring defect. In Figure 3.6, the bearing type used is 6010 and the length and height of the defect are 10.0 mm and 50 μm , respectively. The defect is located at an angle of -90° and the deformation of the ball, which is initially at an angle of 0° , is studied. The inner ring rotates almost half a revolution before the defect coincides with the ball. Angles α_1 and α_2 in Figure 3.6 can be calculated using the following equation:

$$\alpha_1 = 2\alpha_2 = \frac{L_{defect}}{R_{in}} \cdot \frac{2(r + R_{in})}{2r + R_{in}} \quad (3.50)$$

The duration of the pulse generated by defect is, thus, longer than the actual angle it occupies. This is due to the fact that the inner ring and the cage move in same direction. The defect in the outer ring is generated by replacing θ_{in} with θ_{out} in Equation (3.47). This approach is valid either in the case of a stationary or rotating outer ring.

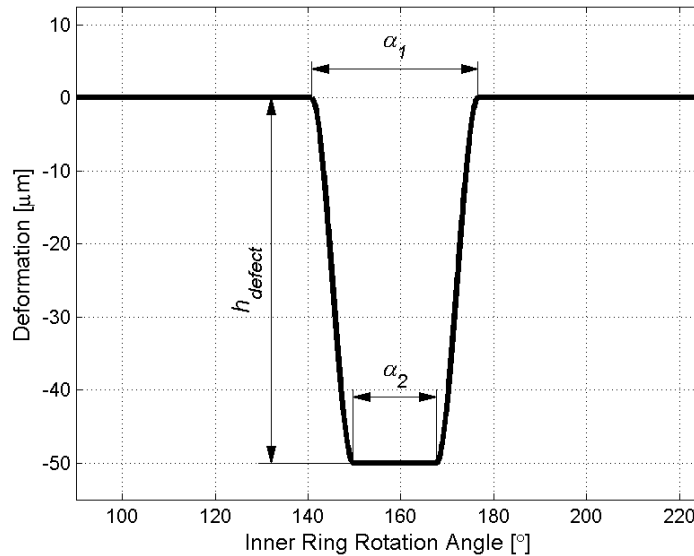


Figure 3.6 The shape of the defect in the inner ring as a function of the angle of rotation of the inner ring.

3.6 Summary

In this chapter, a dynamic simulation model of a deep groove ball bearing with number of non-idealities was presented. The non-idealities modeled here are the waviness of the rings, the localized defects in the bearing rings and misalignments. The bearing model introduced is computationally efficient due to the assumptions that are made in the modeling procedure. The cage of the bearing is assumed to be ideal, i.e. the balls move perfectly in their predefined positions. The model can be used in general multibody or rotor dynamics software as an interface element between the rotor and the support. In Chapter 4, the results of the simulation of an electric motor supported by two ball bearings is presented and discussed.

The modeling approach presented here can be applied to other rolling element bearing types by modifying the kinematical description and contact calculation of the bearing. The discussed elliptical contact theory can be applied directly to spherical roller bearings. In this case, only the kinematical description of the bearing needs to be modified. In tapered roller bearings, the contacts between the races and rollers are rectangular and, thus, the contact calculation should also be modified. Furthermore, other types of interface elements can be modeled using the multibody simulation approach; for example, a model of a plain journal bearing including journal waviness was proposed by Hannukainen *et al.* [85]. The proposed journal bearing model computes nonlinear bearing forces. Therefore, it also functions in situations where large displacements of the shaft occur.

4 CASE I: ELECTRIC MOTOR SUPPORTED WITH BALL BEARINGS

In this chapter of the thesis, an electric motor supported by two ball bearings is studied, and the numerical results of the ball bearing model proposed in Chapter 3 are presented. Bearing-induced vibrations caused by the varying compliance effect, the waviness of the rings and localized defects in the rings are analyzed. The results obtained in this chapter are compared and found to agree well with those available in literature. The non-idealities of the bearing are analyzed separately in this study. However, misalignments in the bearing, the waviness of the rings and defects in the bearing can be combined and simultaneously studied utilizing the proposed model.

The bearing model is implemented on a commercial multibody software application (MSC.ADAMS [24]) in such a way that the software application's own mathematical properties are utilized. In practice, this was done using user-defined variables that describe the elastic deformations of each ball in the bearing. These variables are used in the calculation of the bearing forces. The user interface of the multibody simulation software application used was modified in order to facilitate the composition of the proposed bearing model. The parameters of the bearing model can be entered through this interface. Using these parameters, a macro script creates the equations, geometries and coordinate systems which are required for the description of the bearing. The user interface speeds up the modeling and modification of the bearing.

4.1 Studied Structure

An electric motor supported by two 6010 type ball bearings is studied as an example application of the proposed ball bearing model. The test rotor can be seen in Figure 4.1. The inner rings of both bearings (B_1 and B_2 in Figure 4.1) are rigidly connected to the shafts of the rotor, while the outer rings are rigidly connected to the bearing housings (mass m_h). For reasons of simplicity, the bearing housings have only two degrees of freedom, namely translations in the global X - and Y -directions. The housings are connected to the ground with linear spring-dampers in these directions. The dimensions of the motor are shown in Table 4.1 and the properties of the used bearings are shown in Table 4.2. A gravity load is applied to the system in the negative Y -direction. Unbalance masses are added to the rotor (UB_1) and to the disk (UB_2). Unbalance mass UB_1 is located at the middle of the rotor at an angle of 90° from the positive X -axis and at a distance of 87.5 mm from the rotation axis. Unbalance mass UB_2 , for its part, is located at the middle of the disk at an angle of 180° from the positive X -axis and at a distance of 150.0 mm from the rotation axis.

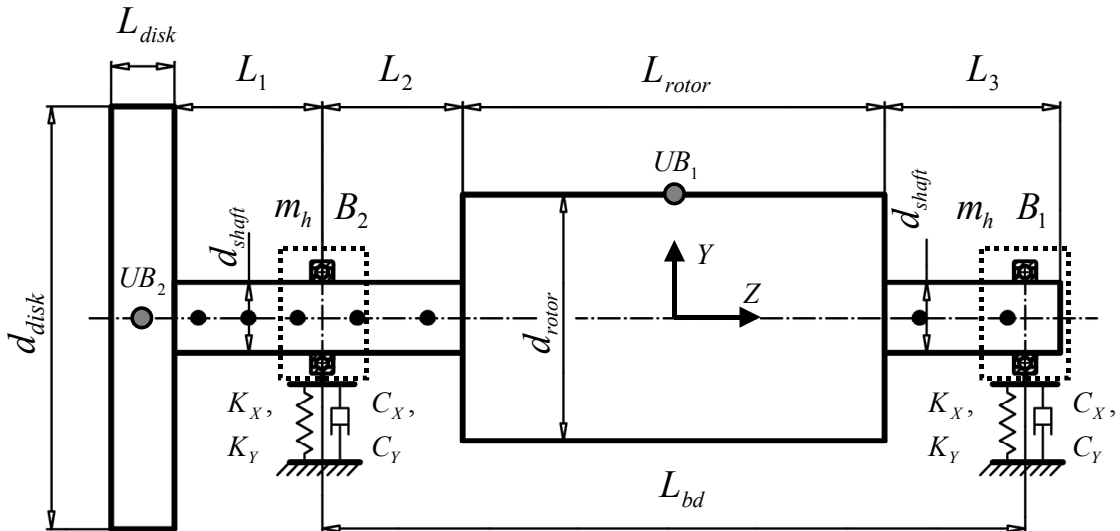


Figure 4.1 A diagram of the electric motor under investigation.

A commercial multibody simulation software application is used in the solution of the bearing equations as well as of the dynamics of the rotor and the supporting structure. Both shafts of the motor are modeled as flexible bodies. The flexibility of a body can be modeled in the used software application by using the floating frame of reference approach or the finite segments approach; the latter technique is used in this example. Both methods give similar results when beam structures are considered. However, the same results can be obtained with fewer degrees of freedom using the floating frame of reference formulation. On the other hand, the parameterization of the model is difficult when using this approach, since a finite element solution is needed to obtain a new set of modes when the dimensions of the body are modified. In the finite segments approach, parameterization can be performed within the multibody software alone. For this reason, the finite segments approach was selected for this example. In the finite segments approach, the shaft is divided into discrete mass points, represented as dots in Figure 4.1. The mass points are connected to each other by spring-damper elements. The spring elements are based on the Timoshenko beam theory that takes shear deformation into account. The connector forces are calculated from the relative displacements and velocities of the mass points. The damping elements are obtained by multiplying the stiffness matrix, which represents the spring forces, by a damping ratio of 0.01. The shafts and rotor of the motor are made of steel (Young's Modulus, $E = 206000$ MPa, material density, $\rho = 7801$ kg/m³ and Poisson's ratio, $\nu = 0.3$).

In the simulations, the motor rotates around the Z-axis in the counterclockwise direction. The translational displacements are measured from both the bearings and the rotor and disk. The simulations are performed at a constant speed and the calculated displacements are analyzed using FFT (Fast Fourier Transform). The simulation data is recorded at a frequency of 2000 Hz. The following signal processing procedures are applied to the time domain data after a sample of 16384 points (8.192 seconds) is extracted

- Hanning-window averaging for time domain signal
- FFT
- The multiplication of the amplitude by 2 (Hanning correction)

The numerical integrator used here is Gear stiff with an error tolerance of $1.0 \cdot 10^{-4}$ and a maximum time step of $2.0 \cdot 10^{-4}$ seconds. The model of the electric motor has 61 degrees of freedom. The calculation times vary depending on the number of non-idealities included in

the bearings and the rotation speed of the motor. Using a Pentium 4 1.7 GHz processor, the ratio between the CPU time and simulated time (i.e. the real-time ratio) varies between 187 and 560 in the simulations presented here. It must be noted that the calculation times are model-dependent and it is difficult to draw general conclusion as to the CPU time. Furthermore, the ball bearing model could easily be implemented as a subroutine, and in this way, more computational efficiency could be achieved.

Table 4.1 The dimensions and parameters of the studied electric motor.

Diameter of the shaft	d_{shaft}	50.0 mm
Diameter of the rotor	d_{rotor}	175.0 mm
Diameter of the disk	d_{disk}	300.0 mm
Length of the shaft 1	L_1	105.0 mm
Length of the shaft 2	L_2	100.0 mm
Length of the rotor	L_{rotor}	300.0 mm
Length of the shaft 3	L_3	125.0 mm
Width of the disk	L_{disk}	45.0 mm
Bearing distance	L_{bd}	500.0 mm
Horizontal support stiffness	K_X	100 kN/mm
Vertical support stiffness	K_Y	100 kN/mm
Horizontal support damping	C_X	10.0 Ns/mm
Vertical support damping	C_Y	10.0 Ns/mm
Mass of the bearing housing	m_h	3.17 kg
Mass of the disk	m_{disk}	20.0 kg
Rotational inertias of the disk	$\{J_{xx}, J_{yy}, J_{zz}\}$	$\{1.1, 1.1, 2.0\}$ kgm ²
Gravity constant (-Y)		9.80665 m/s ²

Table 4.2 The dimensions of the type 6010 deep groove ball bearing.

Bore diameter	d_1	50.0 mm
Outer diameter	D	80.0 mm
Pitch diameter	d_m	65.0 mm
Ball diameter	d	8.73 mm
Number of balls	z	14
Diametral clearance C2	c_d	5.5 μ m
Diametral clearance C5	c_d	59.0 μ m
Bearing damping coefficient	c_b	0.55 Ns/mm
Inner and outer race conformity	R_r	0.52
Static load rating	C_0	16000 N
Modulus of elasticity	E	206000 MPa
Poisson's ratio	ν	0.3
Viscosity parameter	α	0.023 mm ² /N
Viscosity parameter	η_0	0.04 \cdot 10 ⁻⁶ Ns/mm ²

4.2 Simulation Results

4.2.1 Effect of Diametral Clearance

In this section, the vibrations of the bearings are studied for different values of diametral clearance. The unbalance masses, UB_1 and UB_2 , are 2.0 g and 1.0 g, respectively. Two different values of the diametral clearances (C2 and C5 shown in Table 4.2) are studied. The rotational frequency of the shaft is chosen to be 100 Hz, which leads to a varying

compliance frequency, i.e. a ball passage outer ring frequency of 605.89 Hz. The calculation of the bearing defect frequencies is shown in Appendix B.

The natural frequencies and modal damping ratios of the rotor-bearing system are solved by linearizing the nonlinear equations of motion in a static equilibrium state [86]. In the static case, only gravity forces are applied to the motor. The comparisons of natural frequencies with the different values of the diametral clearance are shown in Tables 4.3 and 4.4. In Table 4.3, the balls are set in such a way that one ball was at an angle of 0° from the positive X -axis and other balls were evenly distributed around the circumference. In Table 4.4, one ball was at an angle of 270° from the positive X -axis. These two cases represent the extreme positions of the ball set. It is important to note that these natural frequencies are for a non-rotating rotor, and thus, gyroscopic effects have been neglected. It can be seen from Tables 4.3 and 4.4 that the stiffness of the bearing decreases as its clearance increases. This phenomenon was also noted by Tiwari *et al.* [61]. An increase in clearance decreases, in particular, the horizontal stiffness of the bearing. The position of the ball set has some effect on the natural frequencies, but not as much as does the bearing clearance.

Table 4.3 The natural frequencies of the motor for different values of diametral clearance when one ball is at an angle of 0° from the positive X -axis.

Mode Type	Diametral clearance C2 $c_d = 5.5 \mu\text{m}$		Diametral clearance C5 $c_d = 59.0 \mu\text{m}$	
	Damping [%]	Frequency [Hz]	Damping [%]	Frequency [Hz]
Axial	3.82	28.176	4.02	26.814
Horizontal	3.13	128.26	3.60	58.318
Horizontal	3.32	148.54	1.89	82.930
Vertical	4.42	154.19	4.15	149.58
Vertical	5.90	218.09	5.03	200.40
Horizontal	25.2	941.01	28.1	839.73
Horizontal	22.4	1067.1	26.2	905.21
Vertical	20.3	1174.6	21.9	1088.5
Vertical	18.9	1272.5	19.6	1224.2

Table 4.4 The natural frequencies of the motor for different values of diametral clearance when one ball is at an angle of 270° from the positive X -axis.

Mode Type	Diametral clearance C2 $c_d = 5.5 \mu\text{m}$		Diametral clearance C5 $c_d = 59.0 \mu\text{m}$	
	Damping [%]	Frequency [Hz]	Damping [%]	Frequency [Hz]
Axial	3.82	28.198	4.01	26.881
Horizontal	3.24	131.13	1.83	70.272
Horizontal	3.74	165.15	2.89	88.530
Vertical	4.43	154.43	4.06	147.99
Vertical	6.01	220.13	5.39	208.17
Horizontal	24.3	976.85	27.4	860.65
Horizontal	22.0	1083.8	26.9	880.23
Vertical	20.1	1186.5	21.2	1122.8
Vertical	18.8	1275.3	19.8	1209.2

Spectrums of the horizontal and vertical displacements of Bearing 2 are shown in Figure 4.2. Due to unbalance excitation, the vibration at rotational frequency (1X) is predominant. The harmonics of the rotation speed can be seen clearly in Figure 4.2. Further excitation is caused by the varying compliance (VC) effect. These two forms of excitation produce sum

and difference frequencies, such as $VC \pm 1X$ as demonstrated by Tiwari *et al.* [62]. It can be seen that the vibration level is greatly increased when the bearing clearance is increased from $5.5 \mu\text{m}$ to $59.0 \mu\text{m}$.

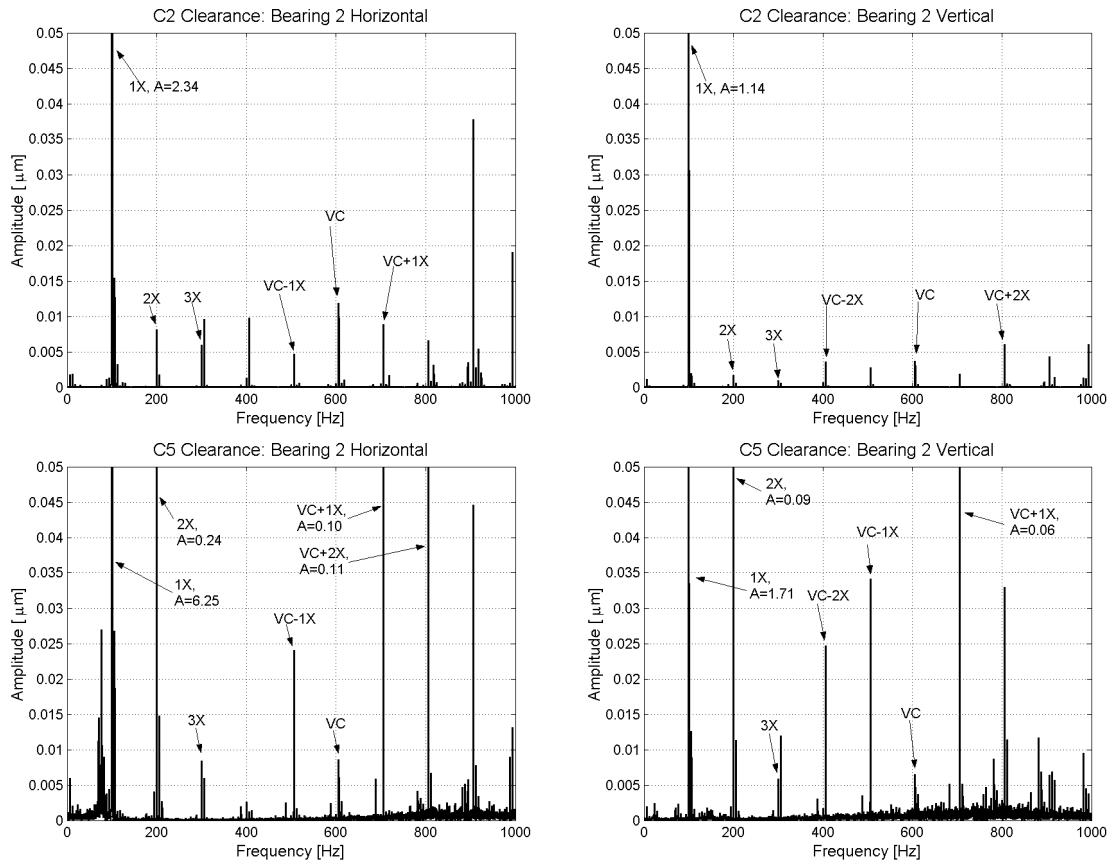


Figure 4.2 Spectrums of the bearing displacements with C2 and C5 clearances. X = rotation frequency, VC = varying compliance frequency.

4.2.2 Waviness of the Rings

Waviness in the inner and outer ring produces vibrations, the frequency of which depends on the order as well as the location (i.e. inner or outer ring) of the waviness. This section discusses both low- and high-order waviness.

Waviness Orders 2, 3, 4 and 5 Low-order waviness in a rotating ring generates vibration at the frequencies of the rotation speed multiplied by the number of waves. This may lead to subcritical superharmonic resonances when the rotation speed is a fraction of the natural frequency of the system. For this reason, orders of 2 to 5 of inner ring waviness are studied here. These waviness orders are combined, i.e. four different waves are summed. Both bearings are assumed to have the same waviness and C2 diametral clearance. The waviness amplitudes and phase angles used in this case can be seen in Table 4.5. The rotation speed range, 10 – 128 Hz, is covered by a series of constant speed steps. The increment of the speed steps is 2 Hz, which results in a total of 60 spectrum lines. Unbalance masses UB_1 and UB_2 are 2.0 g and 1.0 g, respectively.

Figure 4.3 shows a waterfall plot of the vertical displacement of the disk. The harmonics of the rotation speed are clearly visible, and superharmonic resonances occur at speeds of $1/2$, $1/3$, $1/4$ and $1/5$ times the critical speed. These resonances are evidently caused by the waviness of the inner rings of the bearings. If the motor is designed to operate under the

first critical speed, these superharmonic resonances may be harmful. However, if the phase angles of the waviness orders are not equal in both bearings, the level of excitation will not be that high. It must be noted that the spectrum contains peaks at frequencies of $1/2X$ and $3/2X$ when the rotation speed is 100 Hz. The reason for these peaks is not specifically known, and a more detailed study should be carried out to ascertain the exact cause of these peaks; however, Tiwari *et al.* [62] reported the existence of $1/2X$ vibration at some rotational frequencies.

Table 4.5 The amplitudes and phase angles of the different waviness orders.

Waviness order N_{in}	Amplitude [μm]	Phase angle [rad]
2	4.0	$\pi/2$
3	3.0	$\pi/3$
4	2.0	$\pi/4$
5	1.0	$\pi/5$

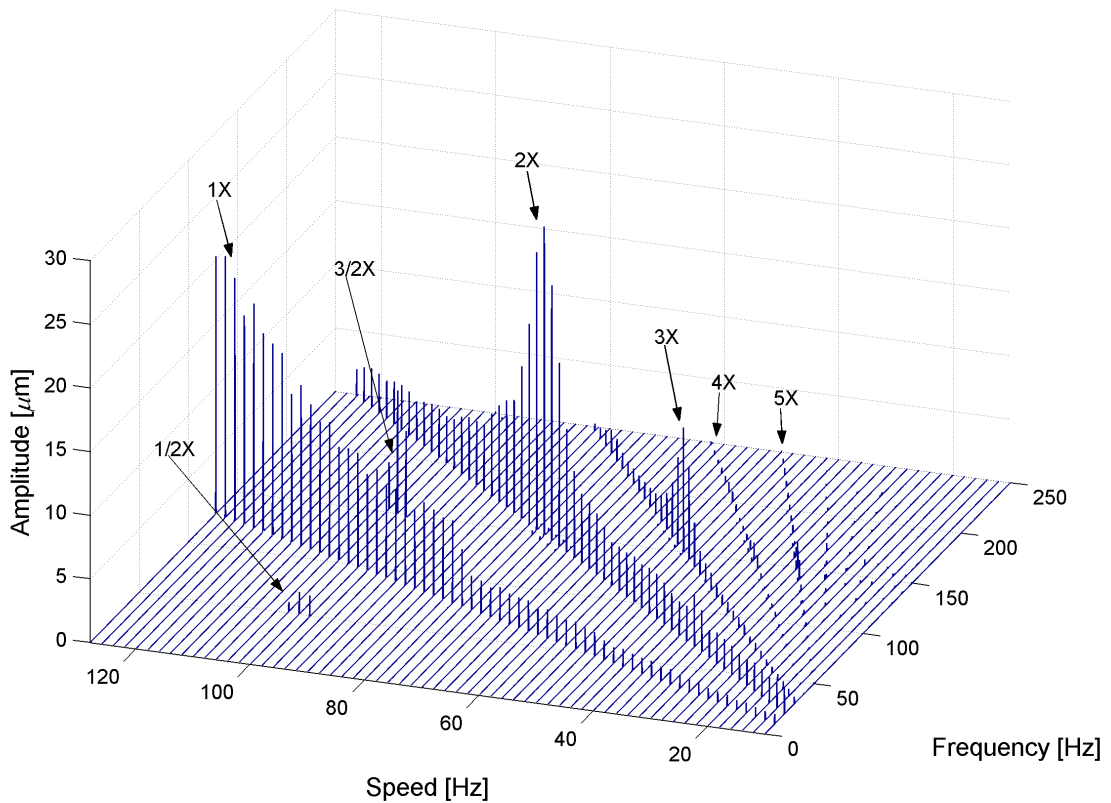


Figure 4.3 A waterfall plot of the vertical displacement of the disk.

Waviness Orders $z-1$, z and $z+1$

The number of balls, z , in the ball bearing type used here is 14. Previous researchers [65, 68] have found that waviness orders of $z-1$, z and $z+1$ produce the most severe vibrations, which is the reason why these waviness orders are investigated in this study. For these simulations, an initial axial displacement of $120 \mu\text{m}$ is assigned to Bearing 1 in order to achieve axial preloading. The axial preloading is intentionally selected in such a way that all the balls are not in contact at the same time. The diametral clearance in both bearings is $5.5 \mu\text{m}$, which corresponds to clearance C2. A total of seven cases, in which all the waviness amplitudes and phase angles are $1 \mu\text{m}$ and 0

degrees, respectively, are studied. Both bearings have the same waviness and rotate at a constant speed of 15 Hz. The unbalance masses, UB_1 and UB_2 , are set to zero. In the first three cases, inner ring waviness of orders 13, 14 and 15 are studied separately. In the next three cases, outer ring waviness of orders 13, 14 and 15 are studied separately. In the last case, the waviness orders of both the inner and outer ring are 13, 14 and 15. Since the rotation speed of the shaft, f_s , is 15 Hz, the inner ring defect frequency, f_{pbir} , is 119.1 Hz and the outer ring defect frequency, f_{bpor} , 90.9 Hz. The equations for the calculation of the bearing defect frequencies can be found in Appendix B.

The spectrums of the axial and vertical displacements of Bearing 2 for different orders of inner ring waviness are shown in Figures 4.4-4.6. The frequencies of the highest amplitudes are shown at the top of the peak. The excitations are caused by the waviness of the inner ring and the varying compliance effect. These two excitations produce sum and difference frequencies that can be calculated from the following equation

$$f(i, j, k) = i \cdot (f_{bpir} + k \cdot f_s) + j \cdot \left\{ (f_{bpir} + k \cdot f_s) - f_{bpor} \right\}, \quad (4.1)$$

where i is the integer coefficient of waviness excitation ($i = 0, 1, 2, \dots$), j the number of the sideband frequency ($j = \pm 0, 1, 2, \dots$) and k the number of waves in the inner ring minus the number of balls ($k = N_{in} - z$); for example, the frequencies shown in Figures 4.4-4.6 are calculated in Table 4.6. It can be seen that the frequencies are equivalent to those obtained using FFT within the frequency resolution of FFT ($1/8.192 \text{ s} \approx 0.122 \text{ Hz}$). The interaction between inner and outer ring waviness has been reported [65, 70] to generate sideband frequencies, but the interaction between the varying compliance effect and inner ring waviness also generate sidebands.

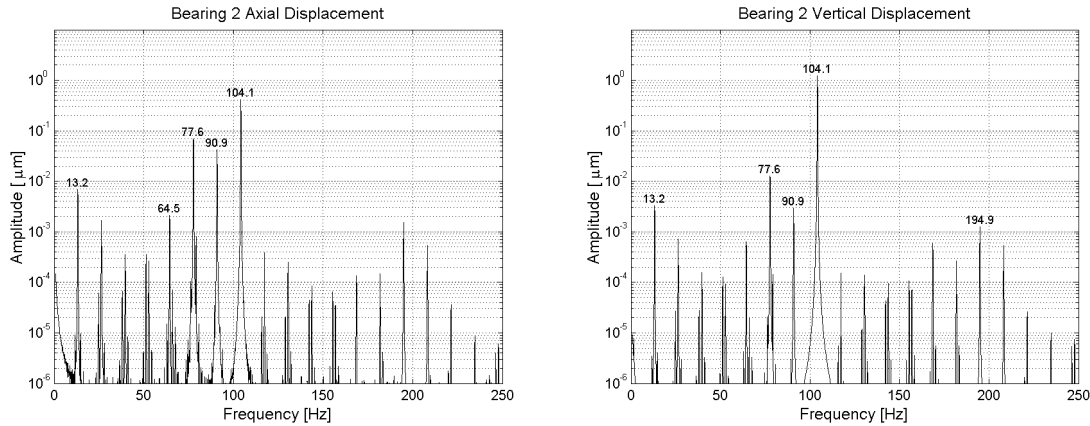


Figure 4.4 Inner ring waviness of order 13.

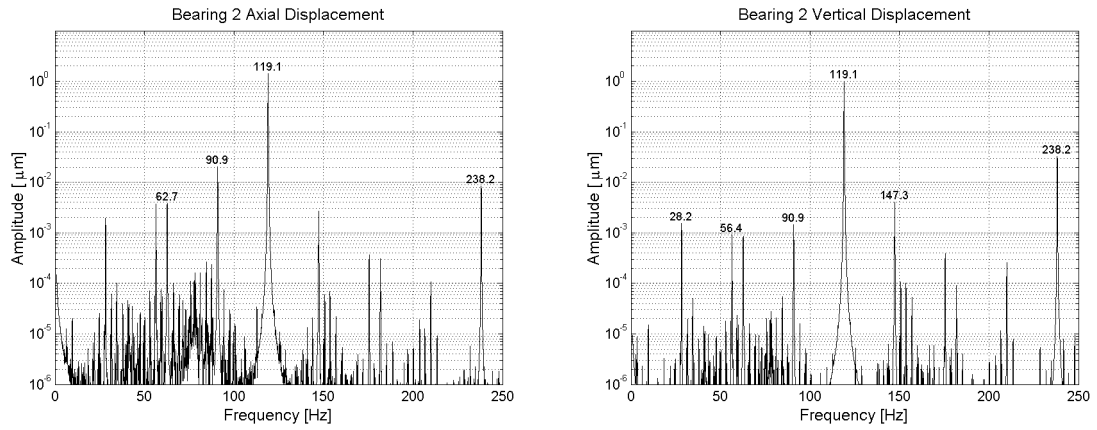


Figure 4.5 Inner ring waviness of order 14.

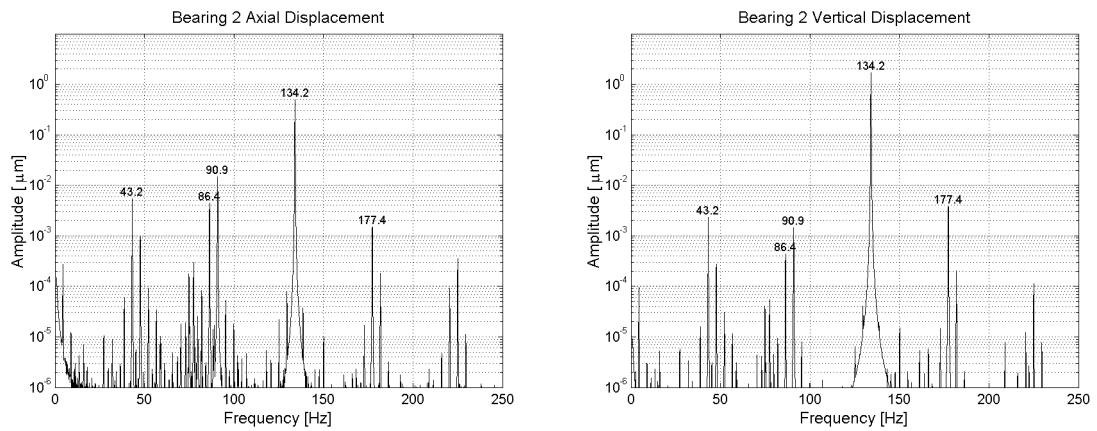


Figure 4.6 Inner ring waviness of order 15.

Table 4.6 The sum and difference frequencies calculated from Equation (4.1).

$N_{in}=13$				$N_{in}=14$				$N_{in}=15$			
i	j	k	$f(i,j,k)$ [Hz]	i	j	k	$f(i,j,k)$ [Hz]	i	j	k	$f(i,j,k)$ [Hz]
0	1	-1	13.2	0	1	0	28.2	0	1	1	43.2
1	-3	-1	64.5	0	2	0	56.4	0	2	1	86.4
1	-2	-1	77.7	1	-2	0	62.7	1	-1	1	90.9
1	-1	-1	90.9	1	-1	0	90.9	1	0	1	134.1
1	0	-1	104.1	1	0	0	119.1	1	1	1	177.3
2	-1	-1	195.0	2	0	0	238.2	-	-	-	-

Using a linear model, Wardle [65, 66] predicted that inner ring waviness of orders $z \pm 1$ generates radial vibrations at frequencies of $f_{pbir} \pm f_s$, which is confirmed by the bearing model proposed here. On the other hand, Wardle concluded that waviness of orders $z \pm 1$ does not generate any axial vibration and waviness of order z does not generate any radial vibrations, which was also confirmed by Jang and Jeong [70]. In these cases, preloaded bearings were studied, which is why the loading in the axial direction was symmetric and all the rolling elements were always in contact. Furthermore, the axial loads were heavy in comparison with the radial load, which is not the case in this study. The axial preloading is not heavy enough to maintain all the balls in contact, and the radial loading is not negligible in comparison with the axial load. For this reason, the bearing generates axial vibration when waviness orders are $z \pm 1$ (13 and 15). However, the amplitude of axial vibration is much larger when the waviness order is z . Aktürk [68] found that the most severe vibrations occur when the number of waves in the inner ring is $z \pm 1$, although other

waviness orders also produced vibrations. Aktürk's bearings were asymmetrically loaded, but he explained the differences between the results of his and Wardle's model on the basis of the nonlinearity of his model.

Outer ring waviness of orders $z-1$, z and $z+1$ produces vibrations at the outer ring defect frequency, f_{bpor} , and its multiples, as mentioned by Wardle [65, 66], Jang and Jeong [70] and Aktürk [68], which is also confirmed by the proposed model. The spectrums of the axial and radial displacements of Bearing 2 are shown in Figure 4.7 when the outer ring has 13 waves. Five harmonics of the outer ring defect frequency are clearly visible. The amplitudes of three harmonics of the outer ring defect frequency for different orders of outer ring waviness are shown in Table 4.7. It can be seen that the most severe axial vibration occurs when the number of waves is 14. However, axial vibration also occurs when the waviness orders are 13 and 15. Horizontal vibration is not generated when the number of waves is 14; this is due to the symmetry of the loading in the horizontal direction. In this case, horizontal excitation forces are cancelled out. Vertical vibration occurs when the number of waves is 14; however, the amplitude is smaller than in the cases of 13 and 15 waves.

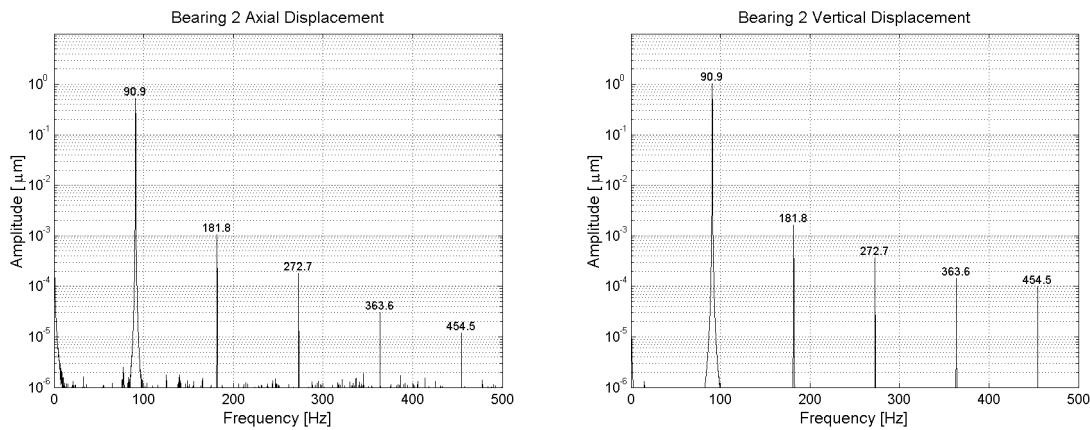


Figure 4.7 Outer ring waviness of order 13.

Table 4.7 The vibration amplitudes in the outer ring defect frequency and its 2nd and 3rd harmonics.

Axial Vibration Amplitudes [μm]				
Frequency		$N_{out}=13$	$N_{out}=14$	$N_{out}=15$
type	[Hz]			
f_{bpor}	90.9	0.524804	3.960455	0.525466
$2f_{bpor}$	181.8	0.001062	0.173064	0.000853
$3f_{bpor}$	272.7	0.000180	0.005191	0.000201
Horizontal Vibration Amplitudes [μm]				
Frequency		$N_{out}=13$	$N_{out}=14$	$N_{out}=15$
type	[Hz]			
f_{bpor}	90.9	1.085988	0.004086	1.087222
$2f_{bpor}$	181.8	0.000484	0.006838	0.002245
$3f_{bpor}$	272.7	0.000363	0.002943	0.000310
Vertical Vibration Amplitudes [μm]				
Frequency		$N_{out}=13$	$N_{out}=14$	$N_{out}=15$
type	[Hz]			
f_{bpor}	90.9	1.021127	0.300499	1.021097
$2f_{bpor}$	181.8	0.001624	0.028477	0.001035
$3f_{bpor}$	272.7	0.000364	0.005817	0.000381

Inner and outer ring waviness is combined in the last case in which both the inner and outer ring have waviness of orders 13, 14 and 15. Figure 4.8 shows the spectrums of the axial and radial displacements of Bearing 2. In this case, the level of vibration is clearly higher than in the cases in which only one waviness was considered. Different excitations produce sum and difference frequencies that can be explained mainly by Equation (4.1). However, several inner ring waviness orders produce a difference frequency of 15 Hz, which is the rotation speed of the shaft, f_s .

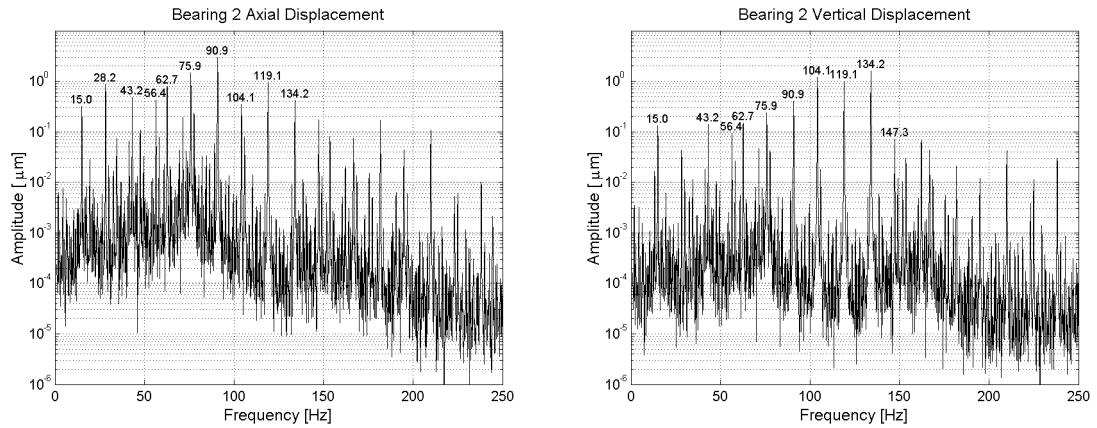


Figure 4.8 Combined waviness. Both the inner and the outer ring have waviness orders of 13, 14 and 15.

4.2.3 Localized Defects

This section discusses the localized defects of the inner and outer rings. The defects are modeled as explained in Section 3.5.2. Defects of two sizes are studied, namely large defects, where $L_{defect} = 2.0$ mm and $h_{defect} = 50.0$ μm , and small defects, where $L_{defect} = 1.0$ mm and $h_{defect} = 25.0$ μm . The defects are added to Bearing 2. The rotation speed used in these studies is 15 Hz, and both bearings have a clearance of C2. The unbalance masses, UB_1 and UB_2 , are set to zero. The inner ring defects are located at an angle of 0° and the outer ring defects at an angle of -90° from the positive X -axis.

Inner Ring Defect

The spectrums of the horizontal and vertical displacement of Bearing 2 for the case of a large inner ring defect are shown in Figure 4.9. The rotation speed and its multiples, as well as the inner ring defect frequency and its multiples, are clearly visible in the spectrums. The analytical model proposed by Tandon and Choudbury [71] could not predict the peaks at the rotation speed and its multiples. The inner ring defect frequency and its harmonics have sidebands at frequencies of $i \cdot f_{bpir} \pm j \cdot f_s$, where i and j are integers ($i, j = 1, 2, \dots$). The amplitudes at frequencies of 134.2 Hz and 149.0 Hz are larger than at f_{bpir} (119.1 Hz), because the natural frequency of the system is close to the excitation frequencies (see Table 4.3). The spectrum contains the same frequencies that are found through experimental measurements on severely damaged bearings [72]. Table 4.8 shows an amplitude comparison between the small and large defect. It can be seen that the amplitudes do not increase linearly when the size of the defect increases.

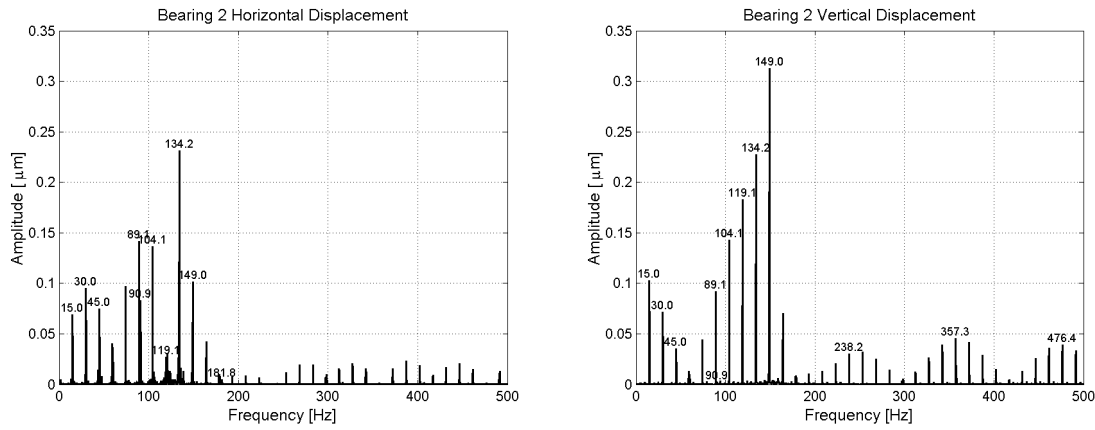


Figure 4.9 The spectrum of the horizontal and vertical displacement of the bearing. A large inner ring defect, $L_{defect}=2.0$ mm and $h_{defect}=50.0$ μm .

Table 4.8 A comparison of the vibration amplitudes at nominal bearing frequencies in the case of the inner ring defect.

Frequency		Horizontal Amplitudes [μm]			Vertical Amplitudes [μm]		
type	[Hz]	Small def.	Large def.	Change%	Small def.	Large def.	Change%
1X	15.0	0.0307	0.0689	124 %	0.0484	0.1025	112 %
2X	30.0	0.0436	0.0954	119 %	0.0338	0.0713	111 %
3X	45.0	0.0346	0.0751	117 %	0.0167	0.0352	111 %
$f_{bpir}-2X$	89.1	0.0674	0.1418	110 %	0.0432	0.0920	113 %
f_{bpor}	90.9	0.0899	0.0831	-8 %	0.0031	0.0025	-19 %
$f_{bpir}-1X$	104.1	0.0653	0.1364	109 %	0.0677	0.1432	112 %
f_{bpir}	119.1	0.0099	0.0271	174 %	0.0869	0.1830	111 %
$f_{bpir}+1X$	134.2	0.1076	0.2316	115 %	0.1081	0.2276	111 %
$f_{bpir}+2X$	149.0	0.0481	0.1017	111 %	0.1502	0.3126	108 %
$2f_{bpor}$	181.8	0.0059	0.0046	-22 %	0.0020	0.0018	-11 %
$2f_{bpir}$	238.2	0.0000	0.0000	-	0.0155	0.0304	96 %
$3f_{bpir}$	357.3	0.0000	0.0000	-	0.0272	0.0455	67 %
$4f_{bpir}$	476.4	0.0000	0.0000	-	0.0295	0.0390	32 %

Outer Ring Defect In the case of the large outer ring defect, the spectrums of the horizontal and vertical displacement of Bearing 2 are shown in Figure 4.10. The spectrum contains peaks at the outer ring defect frequency, f_{bpor} , and its harmonics that are usually found in experimental measurements in the case of severe outer ring defects [72]. In this case, no sideband frequencies are generated, because the outer ring is stationary. The reader should note that the horizontal amplitudes are much smaller than the vertical amplitudes, which is due to the fact that the defect is located at an angle of -90° from the positive X -axis in the outer ring, and thus, the horizontal excitations are negligible. Table 4.9 shows an amplitude comparison between the large and small defects. When the size of a defect is increased, the horizontal amplitudes remain small and the change in amplitude does not follow a clear pattern. The vertical amplitude at the outer ring defect frequency increases approximately by the same amount as that observed in the case of the inner ring defects. The percentile increase in amplitude is smaller in the harmonics of the outer ring defect frequency.

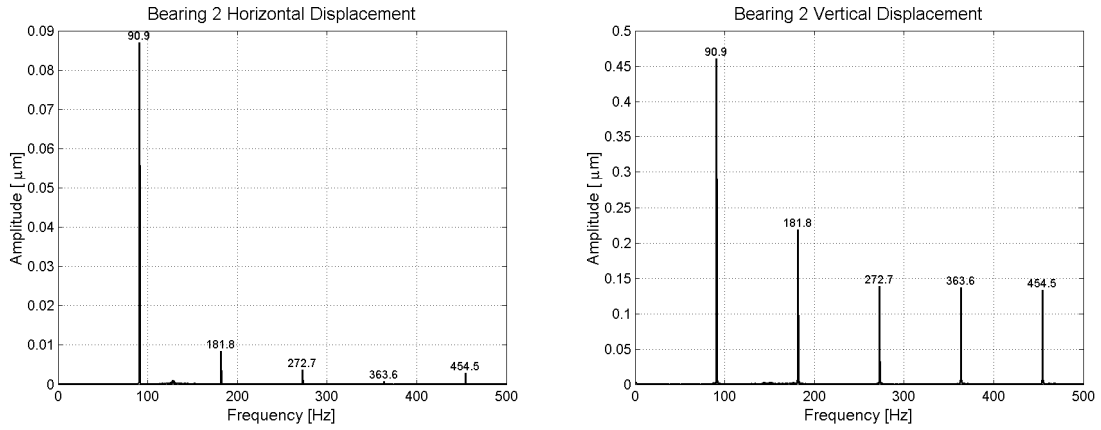


Figure 4.10 The spectrum of the horizontal and vertical displacement of the bearing in the case of an outer ring defect. A large defect, $L_{defect}=2.0$ mm and $h_{defect}=50.0$ μm .

Table 4.9 A comparison of the vibration amplitudes at nominal bearing frequencies in the case of an outer ring defect.

Frequency		Horizontal Amplitudes [μm]			Vertical Amplitudes [μm]		
type	[Hz]	Small def.	Large def.	Change%	Small def.	Large def.	Change%
f_{bpor}	90.9	0.0900	0.0870	-3 %	0.2280	0.4600	102 %
$2f_{bpor}$	181.8	0.0035	0.0085	142 %	0.1163	0.2183	88 %
$3f_{bpor}$	272.7	0.0040	0.0036	-11 %	0.0753	0.1384	84 %
$4f_{bpor}$	363.5	0.0014	0.0008	-45 %	0.0823	0.1365	66 %
$5f_{bpor}$	454.5	0.0010	0.0029	198 %	0.1027	0.1336	30 %

4.3 Summary

It was observed that the diametral clearance has a significant effect on the natural frequencies and vibration response of the system. Ball bearings with an ideal geometry generate vibration due to the varying compliance effect. Unbalance excitation and the varying compliance effect generate sum and difference frequencies. The low-order waviness (out-of-roundness) of the rotating bearing ring produces excitations at frequencies equivalent to the rotation speed multiplied by the order of waviness. These excitations may lead to superharmonic resonances, as is shown in this study. Waviness orders close to the number of balls ($z \pm 1$ and z) generate vibrations at the bearing defect frequencies. In the case of asymmetrical loading, all these waviness orders generate axial and radial vibration. Localized defects also generate vibrations at the bearing defect frequencies. The spectrums obtained by the proposed model are in accordance with reported experimental spectrums. It is important to emphasize that several non-idealities can be combined in the proposed ball bearing model; for example, in Reference [87], the inner and outer ring defects were combined.

5 CASE II: SUBCRITICAL VIBRATIONS OF A TUBE ROLL

In this chapter, the subcritical superharmonic vibrations of a paper machine tube roll are studied using the multibody simulation approach. The example application is a roller test rig that is located at the Laboratory of Machine Design at Helsinki University of Technology. The rotor system under investigation consists of the tube roll supported by a hard bearing type balancing machine. The parameters of the real structure are emulated as accurately as possible in the simulation model of the system. This is achieved by measuring the non-idealities of the real system and incorporating them into the simulation model. The measured non-idealities include the waviness of the rolling surfaces in the interface between the roll and support and the thickness variation of the shell of the roll. The simulation model is verified using the results from experimental modal analysis and the measurement results for the superharmonic response of the roll.

5.1 Studied Structure

The studied paper machine tube roll is shown in Figure 5.1. The roll has been used in the development of measurement and analysis methods for rotor dynamics. The measurement equipment consists of a PC-based data collection system, six laser sensors fitted with amplifiers, a connection panel and a guide trail in which the sensors are installed.

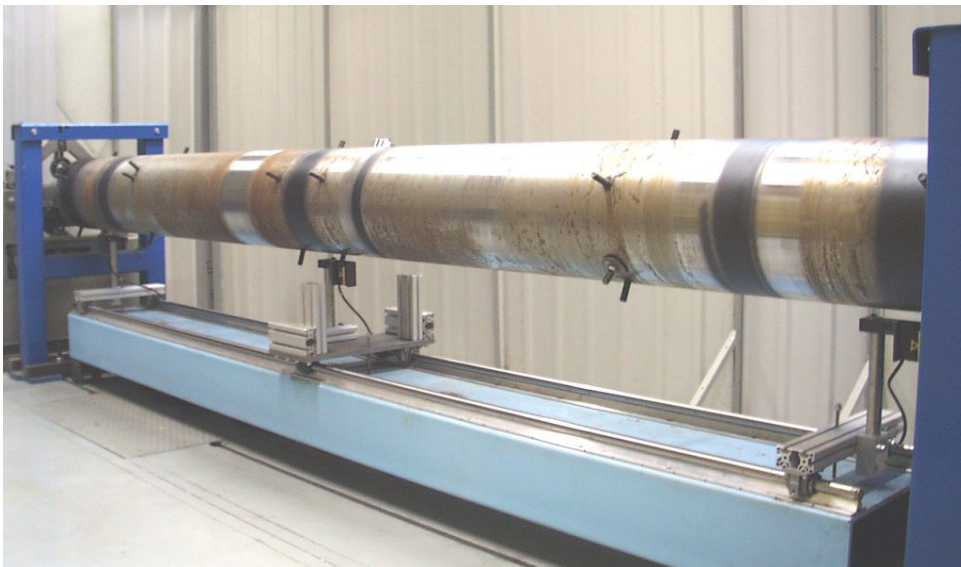


Figure 5.1 The studied paper machine tube roll. The photo is taken prior the installation of laser sensors that measure the throw in horizontal direction.

Although the throw of the roll is measured in three sections, only the measurement results for the middle of the roll in the vertical and horizontal directions are considered in this study; the locations of the measurement points are shown in Figure 5.2. The angular velocity of the rotor is obtained using a pulse sensor. The measurement equipment in the test rig is similar to that used in active damping tests performed on the same structure [88]. The measurements were performed by the staff of the Laboratory of Machine Design as a part of the PyöriVÄRE –project. The measurement results are reported in Reference [89].

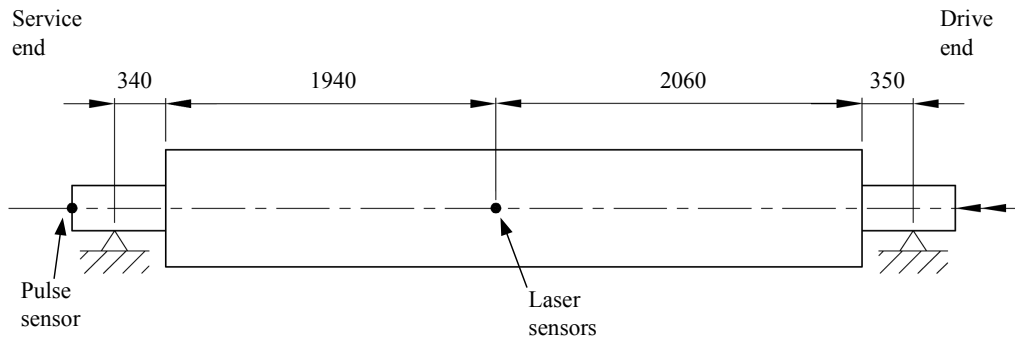


Figure 5.2 The locations of the measurement points in millimeters [85].

5.2 Simulation Model

The roller test rig is modeled in a commercial multibody simulation software application, MSC.ADAMS [24]. The simulation model, shown in Figure 5.3, includes a flexible non-ideal tube roll, the support of the roll and nonlinear contact forces between the roll and the support. The simulation model is briefly described in the following sections, while a more detailed description of the model can be found in Reference [90].

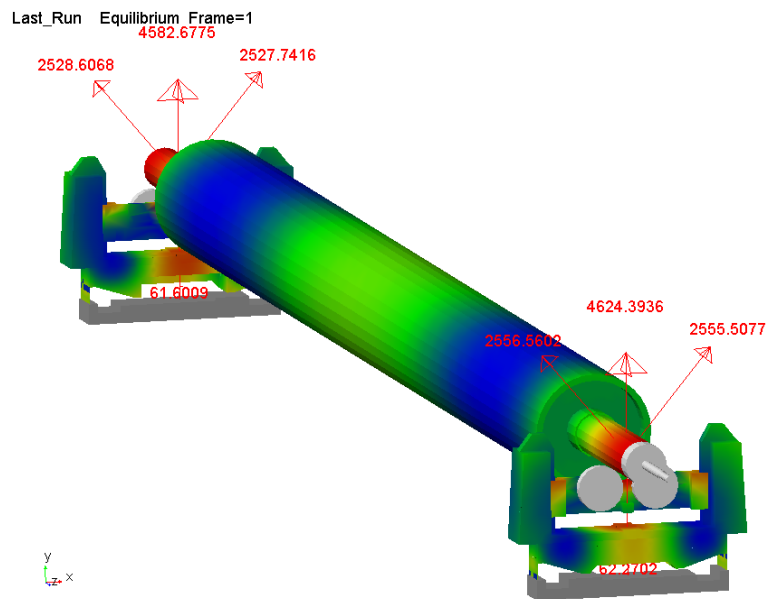


Figure 5.3 The simulation model of the roller test rig.

5.2.1 Flexible Tube Roll

The flexibility of the tube roll is modeled using the floating frame of reference formulation. As explained in Chapter 2, the linear deformations of a body can be described in this method using the vibration modes and frequencies of the body. The modes can be obtained by, for instance, employing the finite element method. In this study, the tube roll is modeled in a commercial finite element code, ANSYS [36], using eight-node brick-shaped solid elements with rotational degrees-of-freedom (SOLID 73). Figure 5.4 shows the coordinate system and mesh of the FE model. More detailed information about the dimensions and the coordinate system of the roll can be found in Appendix C. The finite element mesh of the roll is fine, as can be seen in Figure 5.4. It is important to note that the modes and frequencies are solved using the lumped mass approach, which does not lead to

an exact representation of the inertia of the body. However, the use of a fine finite element mesh makes it possible to obtain an accurate approximation for the inertia properties of the flexible body.

Number of nodes	8744
Number of elements	5536
<i>Material properties:</i>	
Young's Modulus	$2.07 \cdot 10^{11}$ N/m ²
Mass Density	7801 kg/m ³
Poisson's ratio	0.3
<i>Dimensions of the rotor:</i>	
Total length of the rotor	5000 mm
Length of the shell	4000 mm
Diameter of the shell	322.5 mm

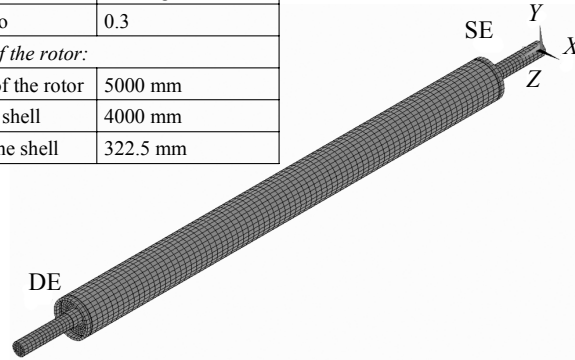


Figure 5.4 The FE model of the roll [85].

The thickness of the shell of the tube roll is based on measurements carried out on the real structure. According to the results of these measurements, the thickness of the shell of the roll varies between 17.86–19.59 mm, while the average thickness is 18.72 mm. The measured shell thickness is shown graphically in Appendix E. The variation in shell thickness is taken into account in the FE model by moving nodes at the inner surface of the shell, since, in general, the variation of the shell thickness in tube rolls occurs on the inner surface of the shell. This approach differs from that used in the previous study [91], where the shell of the roll was modeled using shell elements. The thickness variation in the shell elements is symmetric with respect to the mid-surface of the element. Therefore, by using solid elements, the variation in shell thickness can be modeled more realistically. Since the shell thickness is not constant, the roll has a non-ideal mass and stiffness distribution. The non-ideal mass distribution causes unbalance excitations, while the non-ideal stiffness distribution causes a twice-running-speed (2X) resonance in which the variation in bending stiffness, together with gravity, excites the symmetrical modes. This resonance condition occurs when the rotating speed is one half of the frequency of the symmetrical mode.

In order to study the effect of the variation in the stiffness of the roll on the twice-running-speed resonance, two kinds of roll models were built: one in which the shell thickness is based on the measurements and another in which the variation in shell thickness is amplified by two in compared to the measurements. In the latter case, the thickness of the shell at node i is calculated as follows:

$$t'_i = 18.72 \text{ mm} + 2 \cdot (t_i - 18.72 \text{ mm}), \quad (5.1)$$

where t_i is the measured thickness at the node i .

By applying a technique described in Section 2.2.2, the Craig-Bampton modes are solved using the FE models of the rolls. The Craig-Bampton representation of one roll consists of 56 fixed interface modes and 12 static correction modes. This set of modes is orthogonalized, and a set of approximate free-free modes and boundary modes is obtained.

For the dynamic analysis, a set of bending and longitudinal modes is selected. The torsion modes, as well as the shell vibration modes, i.e. local vibration modes, are disabled. The mass properties and frequencies of the selected modes of the roll models are shown in Appendix D.

Comparison with the Experimental Modal Analysis The natural frequencies of the test roll were measured using the experimental modal analysis [92]. The roll was hoisted up using lifting belts and a flexible spring set between the belts and the crane. The frequencies of the measured rigid body modes were close to zero. The results of the experimental modal analysis are shown in Table 5.1. The incorrect damping ratios for modes 2, 3 and 6 are due to the hoisting belts that increased the damping in the vertical direction. For this reason, the lower damping values are used for each mode pair in the simulation model.

Table 5.1 The results of the experimental modal analysis of the roll.

Mode #	Freq. [Hz]	Damping ratio [%]	Comments
1	78.048	0.018	
2	78.285	0.138	Damping incorrect
3	196.67	0.035	Damping incorrect
4	196.93	0.016	
5	270.27	0.023	
6	270.35	0.034	Damping incorrect

As the roll is non-ideal, the frequencies of the two perpendicular bending modes in each pair of modes are not equal to each other. A Figure 5.5 shows a comparison between the measured modes and those obtained analytically from the model that includes the measured shell thickness variation; it can be seen that the directions of the two lowest bending modes differ from each other, which indicates that the attitude angles of the lowest and the highest bending stiffnesses given by the model differ from those given by the measurements performed on the real roll; these same discrepancies in direction can be also seen in the other two bending mode pairs. Figure 5.5 shows that good correspondence is obtained between the measured and calculated natural frequencies.

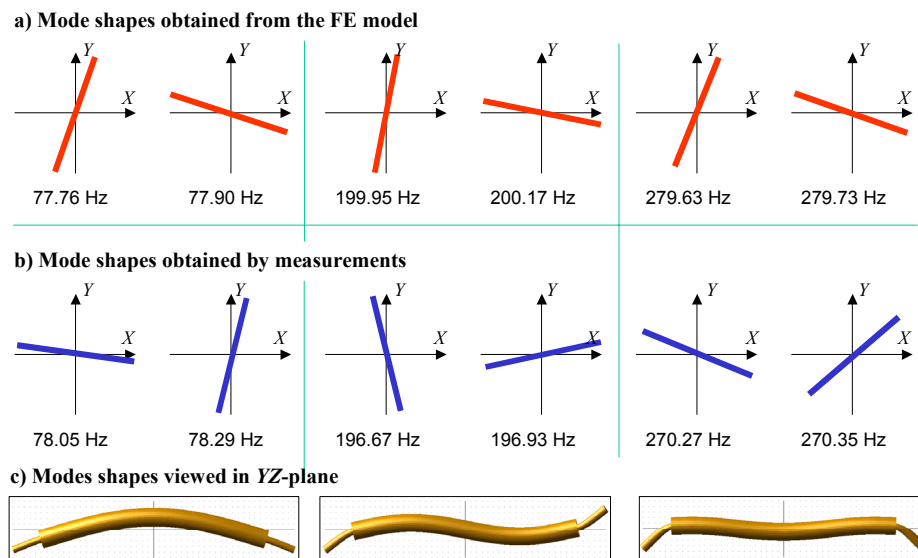


Figure 5.5 A comparison between the measured and calculated mode shapes of the roll.

5.2.2 Roll Support

The roll support is the pedestal of a balancing machine. In the simulation model, the support is modeled using two flexible and three rigid parts, as shown in Figure 5.6. These parts are connected to each other by spring-damper forces and kinematical constraints. The flexibility of the frame part and the attachment plate is described using the same approach as that used for the roll. A total of 34 vibration modes of the frame part section were selected for the dynamic simulation, while the bandwidth of the selected modes varies between 226 Hz and 34.6 kHz. Respectively, a total of 24 vibration modes of the attachment plate were selected, while the bandwidth of these modes varies between 349 Hz and 43.9 kHz. The support is modeled as accurately as possible using the available information. Unknown parameters, such as the damping coefficients, were determined using an optimization procedure, as will be discussed in Section 5.2.4. A more detailed description of the modeling of the support is given in Reference [90].

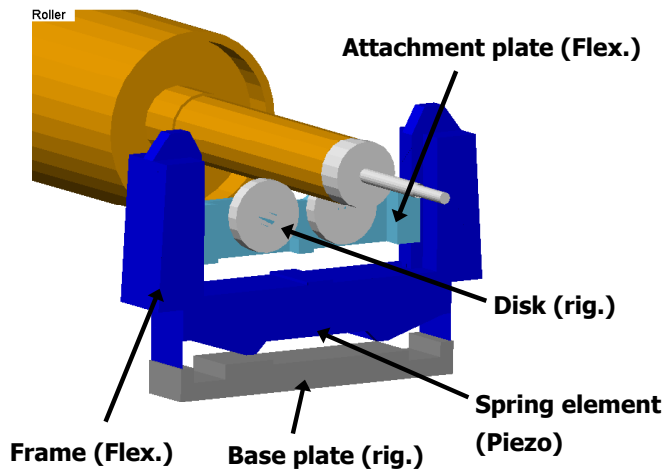


Figure 5.6 The model of the roll support.

5.2.3 Interface between the Roll and Support

The roll is supported by two disks in the balancing machine, as can be seen in Figure 5.7. Neither linear springs nor constraint equations can be used to model this kind of support, because the roll can be lifted off the support freely. For this reason, the interface between the roll and the support is described using nonlinear contact forces. In order to study the superharmonic vibrations of the roll, the waviness of the rolling surfaces must be taken into account in the simulation model. The waviness of the rolling surfaces can be modeled as described in Section 3.5.1 in the case of ball bearings.

Contact Force The contact force can be expressed as a function of the contact penetration and penetration velocity as follows [24]:

$$F = \begin{cases} k_c (x_{c0} - x_c)^{e_c} - STEP(x_c, x_{c0} - d_c, c_c^{\max}, x_{c0}, 0) \cdot \dot{x}_c & , x_c < x_{c0} \\ 0 & , x_c \geq x_{c0} \end{cases} \quad (5.2)$$

where k_c is the stiffness coefficient, e_c the exponent of the force-deflection relationship, x_{c0} the contact distance and x_c the distance between contacting bodies. To avoid discontinuities in the contact force, the velocity-dependent terms are smoothed using the *STEP* function, which is defined by Equation (3.45). Parameter d_c is the penetration, when the maximum

damping constant, c_c^{\max} , is achieved. As shown in Figure 5.7, the disks are connected to the attachment plate by needle roller bearings. In order to calculate the stiffness coefficient, k_c , the flexibility of the roll-disk contact, as well as the flexibility of the needle roller bearing, must be taken into account. These two nonlinear springs are connected in series.

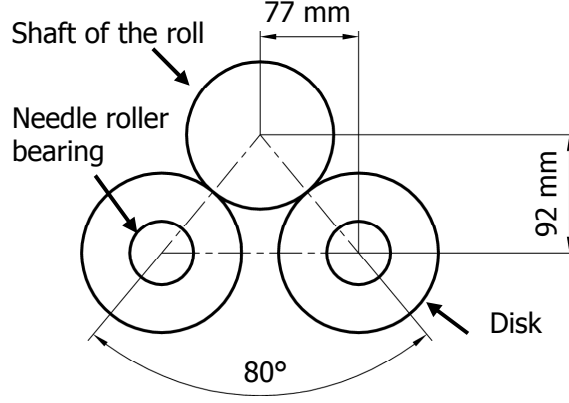


Figure 5.7 The interface between the support and the roll.

The contact between the shaft and the disk can be solved using the Hertzian contact theory [74]. In this case, the type of contact is cylinder-cylinder, the contact area is rectangular and the force-deflection relationship can be solved from Equations (5.3) and (5.4). The semi-width of contact, b_c , can be calculated as follows:

$$b_c = \sqrt{\frac{4F(1-\nu^2)}{\pi L_1 E} \left(\frac{1}{D_1} + \frac{1}{D_2} \right)^{-1}}, \quad (5.3)$$

where F is the contact force, L_1 is the length of the cylinder, ν and E are the Poisson's ratio and the modulus of elasticity of the material, respectively, and D_1 and D_2 are the diameters of the cylinders. The total deflection between the cylinders can be calculated as follows:

$$\delta_{cc} = \frac{2(1-\nu^2)F}{\pi L_1 E} \left(\frac{2}{3} + \ln \frac{4D_1 D_2}{b_c^2} \right). \quad (5.4)$$

In a needle roller bearing, the total load is carried by the contact forces between needles and the races. The number of contacting needles depends on the diametral clearance and deformation of the bearing. The stiffness coefficient for the contact between one needle and both the inner and outer races of a typical roller bearing can be approximated as follows [93]:

$$k_{needle} = 26200 \cdot l_r^{0.92}, \quad (5.5)$$

where l_r is the length of the needle in millimeters and k_{needle} is obtained in N/mm. The elastic deformation of needle i can be calculated from the radial displacement, δ_r , between the inner and the outer race as follows

$$\delta_i = \delta_r \cos \phi_i - \frac{c_d}{2}, \quad (5.6)$$

where ϕ_i is the attitude angle of needle i and c_d is the diametral clearance as shown in Figure 5.8. The total force of the needle roller bearing, F_{nr} , can be calculated from the following equation:

$$F_{nr} = \sum_{i=1}^z k_{needle} \delta_i^{1.08} \cos \phi_i, \quad (5.7)$$

where z is the number of needles and the summation includes only those needles in which δ_i is greater than zero.

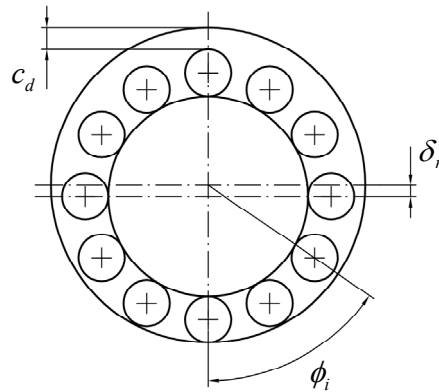


Figure 5.8 The elastic deformation in a needle roller bearing.

Both of the above-mentioned contacts have nonlinear force-deflection relationships. The force-deflection relationship between two cylinders can be solved for a given force without iteration, while the corresponding relationship for a needle roller bearing can be solved for a given displacement. The unknown contact parameters in Equation (5.2) can be determined through the use of curve fitting methods. The numerical values used in the calculation are shown in Table 5.2. The disks and bearings are made of steel, the Young's modulus of which is 206000 N/mm^2 and Poisson's ratio 0.3. The least squares fitting method [94] gives the following values: contact stiffness coefficient, $k_c = 0.2146 \text{ kN}/\mu\text{m}^{1.2173}$, and exponent $e_c = 1.2173$. The contact damping coefficient is selected to be $c_c^{\text{max}} = 2.5 \cdot 10^{-5} \cdot k_c$ on the basis of Equation (3.41). The penetration depth, d_c , is selected to be $5.0 \mu\text{m}$.

Table 5.2 The numerical values used in the contact parameter calculation.

Cylinder-Cylinder contact		Needle Roller Bearing	
Length L_1	25.0 mm	Length of the needle l_r	24.0 mm
Diameter D_1	115.0 mm	Diametral play c_d	$50.0 \mu\text{m}$
Diameter D_2	125.0 mm	Number of needles z	26

Waviness of the Shafts and Disks The measured roundness profiles of the shafts and disks are analyzed using the Fast Fourier Transform (FFT), which gives the amplitudes and

phase angles of the harmonic waviness components. The roundness profile can be expressed in the form of a Fourier cosine series as follows:

$$R(\alpha) = \sum_{k=1}^n c_k \cos(k\alpha + \phi_k), \quad (5.8)$$

where c_k is the amplitude, ϕ_k the phase angle of the k^{th} harmonics and α the attitude angle of the roll. In the simulation model, attention is paid to the harmonic components of 1st to 4th orders only, because the amplitudes of higher components are insignificantly small. The measured amplitudes and phase angles are shown in Table 5.3, and the waviness of the shafts is shown graphically in Appendix E.

Table 5.3 The measured roundness errors of the shafts and disks.

Shaft of the Roll					
Drive end			Service end		
k	Amplitude c_k [μm]	Phase ϕ_k [rad]	k	Amplitude c_k [μm]	Phase ϕ_k [rad]
1	31.89	0.6021	1	43.38	5.2360
2	2.75	0.0349	2	4.05	0.0873
3	0.50	1.4312	3	0.35	1.1170
4	0.20	1.3963	4	0.25	0.2443
Disks					
Drive end			Service end		
k	Amplitude c_k [μm]		k	Amplitude c_k [μm]	
	Front	Rear		Front	Rear
1	2.50	4.00	1	2.00	2.00
2	0.20	0.25	2	0.15	0.15
3	0.10	-	3	-	-

The roundness errors of the disks are distinctly smaller than those of the shafts. Furthermore, the impulses, which come from them, are not repeated similarly on every rotation of the roll because the diameter of the shaft is 125 mm and the diameter of the disks 115 mm. The waviness of the disks is difficult to model precisely, because the rotation angle of one disk may not change in the same relation with the other disks and the rotation angle of the roll. Therefore, it was decided to model the roundness error of the disks without the phase angles. The measuring accuracy of roundness is $\pm 1 \mu\text{m}$ for the shaft and $\pm 0.2 \mu\text{m}$ for the disks.

5.2.4 Comparison with Experimental Modal Analysis and Optimization

The results of the experimental modal analysis of the roller test rig [92] are compared with the natural frequencies and damping ratios obtained from the simulation model. In the simulation model, the natural frequencies, damping ratios and mode shapes can be solved by linearizing the nonlinear equations of motion at static equilibrium state as described in [86]. However, the simulation model contains many unknown parameters, such as damping coefficients, that affect the modal parameters. In order to improve the accuracy of the simulation model, the unknown model parameters are determined using an optimization algorithm. This study employs a Differential Evolution (DE) algorithm. Differential Evolution is a recently developed optimization algorithm for stochastic nonlinear optimization [95]. Optimization is performed by using the *Optimize* program, which is described in Reference [96].

In this case, the optimization problem can be summarized as follows: Find the optimum vector of the input parameters such that the error between the modal parameters in the simulation model and measurement is minimal. The simulation model can be considered to be a “black box” that receives the input vector and returns an output. The objective of optimization is to find input parameters that result in similar damping ratios and frequencies of 10 modes. The stiffness and damping coefficients of the spring-damper forces in the support structure as well as the modal damping ratios of the flexible parts are selected as the input parameters. The results of the optimization are shown in Table 5.4, while the description of the input parameters and the target function can be found in Appendix F. As can be seen in Table 5.4, the accuracy of the model can be improved by using optimization.

Table 5.4 The optimization results. (h = horizontal mode, v = vertical mode).

Mode #	Measured		Simulated			
			Before Optimization		After Optimization	
	Damp. [%]	Freq. [Hz]	Damp. [%]	Freq. [Hz]	Damp. [%]	Freq. [Hz]
1 (h)	0.61	29.83	0.34	29.43	0.58	29.83
2 (v)	1.06	32.16	0.29	32.02	1.14	32.08
3 (h)	1.33	65.34	1.52	63.79	1.39	65.68
4 (v)	1.68	82.23	1.41	79.95	1.85	81.09
5 (h)	1.59	111.59	1.89	108.43	1.75	110.93
6 (v)	1.85	140.00	1.55	138.82	1.41	140.15
7 (h)	2.10	179.04	1.93	182.40	2.28	185.27
8 (h)	2.03	206.62	1.41	224.18	1.88	226.35
9 (v)	1.54	267.00	1.55	258.21	1.69	259.24
10 (h)	1.12	282.78	0.68	307.97	1.01	308.41

5.3 Simulation Results

The simulation results were compared with those obtained by measuring the existing structure. The horizontal and vertical displacements were measured from the middle of the roll. The results were compared in the frequency domain by analyzing the displacements with FFT. The same signal processing procedures as described in Section 4.1 were applied to both the measured and simulated time domain data. In the simulations, the half critical rotation speed region is studied in detail. The results are plotted using amplitude vs. rotation speed charts and spectrum maps.

The numerical integrator used here is Gear stiff with an error tolerance of $1.0 \cdot 10^{-5}$ and a maximum time step of $2.5 \cdot 10^{-4}$ seconds. The model of the roller test rig has 113 degrees of freedom. All the simulations presented in this section were analyzed using a Pentium 4 1.7 GHz processor. In the simulations, the ratio between CPU time and simulated time (i.e. the real-time ratio) varied between 140 and 268, while the average ratio was 196.

5.3.1 Sensitivity Analysis

The superharmonic responses depend on very small non-idealities of the roller test rig. These non-idealities are difficult to accurately measure. For this reason, a sensitivity analysis was performed by varying the parameters that affect the superharmonic responses. In particular, the vertical twice-running-speed response depends on these parameter

variations. A total of seven cases were analyzed. The parameter variations in the simulation cases are described in Table 5.5.

Table 5.5 The parameter variations in the simulation cases.

Simulation Case #	Description
1	Model parameters before optimization.
2	Model parameters after optimization.
3	The phase angles of the second harmonics in the waviness of the shaft are increased by 220 degrees in both ends. This makes the phase angle of the minimum stiffness and that of the second-order waviness approximately same in the model and in the existing roll. Model parameters after optimization are used.
4	Optimization is performed with slightly different target values; the modal damping of the first vertical bending mode of the system is decreased to 0.90 %. The optimization results are shown in Appendix F. The other parameters are same as in Case 3.
5	The shell thickness variation of the roll is two-fold. The other parameters are the same as in Case 3.
6	The amplitude of the second harmonics in the waviness of the shaft is increased by +1 μm in both ends. This variation is within the error tolerance of the waviness measurement. The other parameters are the same as in Case 3.
7	The variations of Cases 4 – 6 are combined; the other parameters are the same as in Case 3.

Figures 5.9 and 5.10 show the amplitudes of the twice-running-speed response for different simulation cases. The simulated horizontal amplitudes correspond very well to the measured ones. Variations in the simulation cases do not affect the horizontal amplitude significantly. The measured maximum amplitude occurs at a rotation speed of 14.6 Hz, which means that the first horizontal natural frequency is, in reality, nearer to 29.2 Hz than 29.8 Hz, which was measured using experimental modal analysis.

The simulated vertical amplitudes vary in different simulation cases, which was expected. Variations to the relative phase angle between the stiffness variation of the roll and the phase angle of second-order waviness change the amplitudes significantly. According to the simulation results, the excitations caused by the second order waviness of the shaft and stiffness variation of the roll are in the same phase when the upper phase of the second-order waviness is coincident with the minimum stiffness direction. In Case 2, these two excitations act against each other and in Case 3 they act in the same phase. Therefore, from Case 2 to Case 3, the maximum amplitude of the vertical twice-running-speed resonance is increased by 30 μm .

The maximum amplitudes in Cases 4 to 6 are practically same. It seems that a decrease in the damping of the first vertical bending mode (Case 4), an increase in the stiffness variation (Case 5) and an increase in the amplitude of the second-order waviness (Case 6) lead to a similar increase in the response. The increase in the maximum amplitude is about 15 μm in each case. In Case 7, all the above-mentioned variations are combined and the maximum amplitude is very near to the measured one.

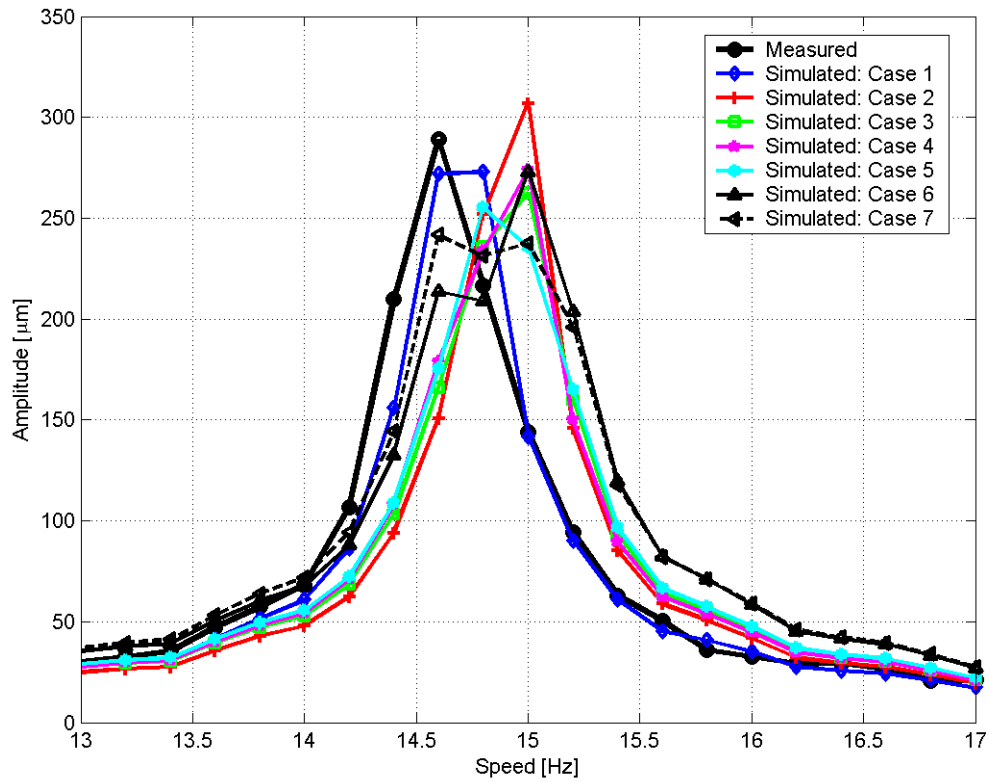


Figure 5.9 The amplitudes of the horizontal twice-running-speed response in the middle.

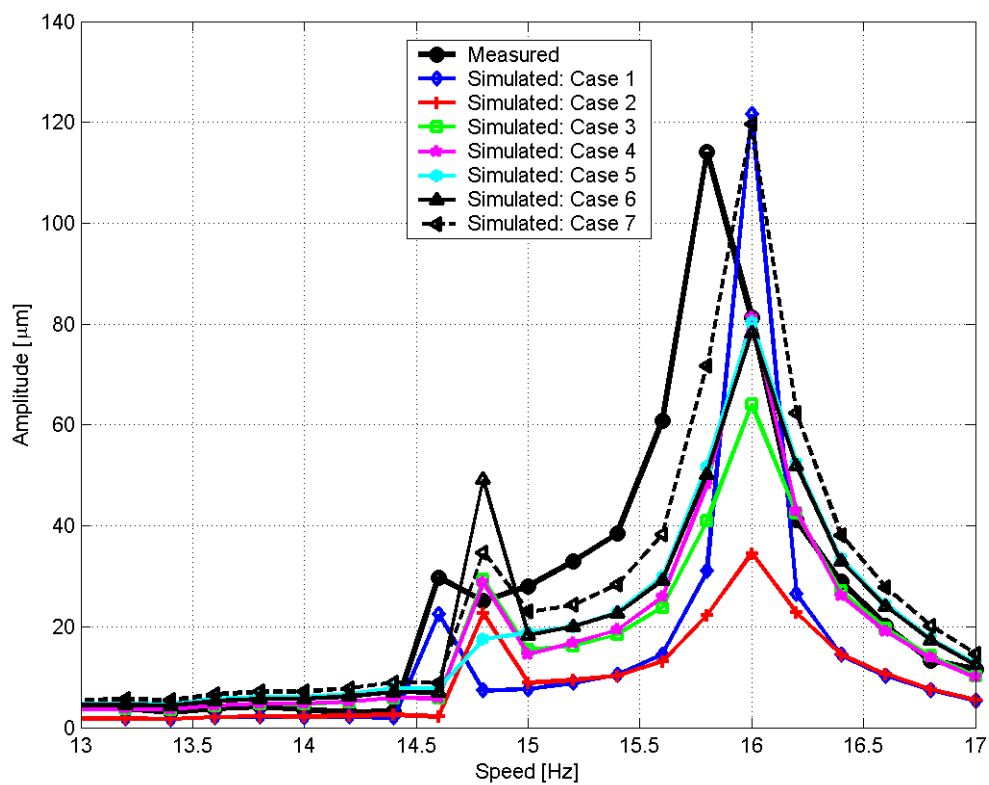


Figure 5.10 The amplitudes of the vertical twice-running-speed response in the middle.

It can be said that the simulation model can accurately predict the twice-running-speed resonances. Variations in different simulation cases are within the error limit of the measured input data. In particular, the stiffness variation of the roll can be larger than in the simulation model, which means that shell thickness is not the only non-ideality of the roll. There can be other non-idealities in the existing roll, such as an uneven modulus of elasticity or welds which affect the stiffness variation of the roll.

The simulation results are compared to measurements using spectrum maps of the displacements. Figures 5.11 and 5.13 show the measured spectrum maps of the vertical and horizontal displacements. The corresponding spectrum maps in simulation Case 3 are shown in Figures 5.12 and 5.14.

All the modeled excitations can be seen in the simulated spectrum maps. The roll in the simulation model is not balanced, as can be seen from the first harmonic component of the displacement. However, the amount of unbalance does not affect the higher harmonic components, and thus, unbalance is not considered in this study. The amplitudes of the horizontal second harmonics are greater than those of the vertical ones in all the simulation cases as well as in the measurements. This is caused by the support of the roll and the second order waviness of the shaft. Figure 5.7 shows that the angle between the disks is 80° . When the elliptical shaft rotates on this kind of a support, the first contact is in the upper phase and the second one in the lower phase of waviness, which causes larger excitation in the horizontal than in the vertical direction; furthermore, the support is more flexible in horizontal direction. The horizontal twice-running-speed resonance can also be seen from the spectrum maps of the vertical displacements as a disturbance in the spectrum.

Three-times-running-speed resonance (3X-resonance) is not visible in the measured spectrum. On the other hand, this resonance can be seen clearly in the simulated spectrums. The simulated resonance amplitudes are quite large in comparison to the twice-running-speed resonance, because the third-order amplitudes of the waviness are less than $1\ \mu\text{m}$, whereas the second-order amplitudes are $2\text{-}4\ \mu\text{m}$. It is possible that in reality the third-order amplitude is zero, because the error estimate in the measurement is $\pm 1\ \mu\text{m}$. The reason for the relatively high response in the simulation results is probably caused by the type of support of the roll. When the triangular shaft rotates on this kind of a support, both contacts are near the upper phases of waviness. After the roll has rotated 30° , both contacts of the roll are in the lower phases waviness, respectively. This causes a larger movement in the vertical direction than does equal-sized second-order waviness.

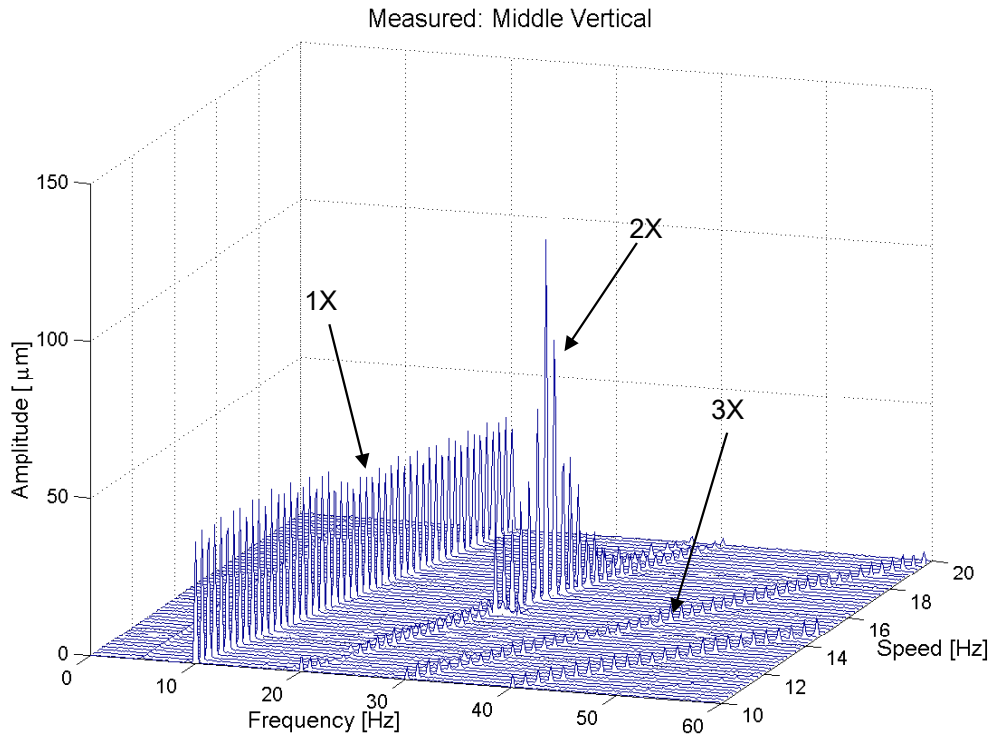


Figure 5.11 The measured spectrum map of the vertical throw in the middle of the roll.

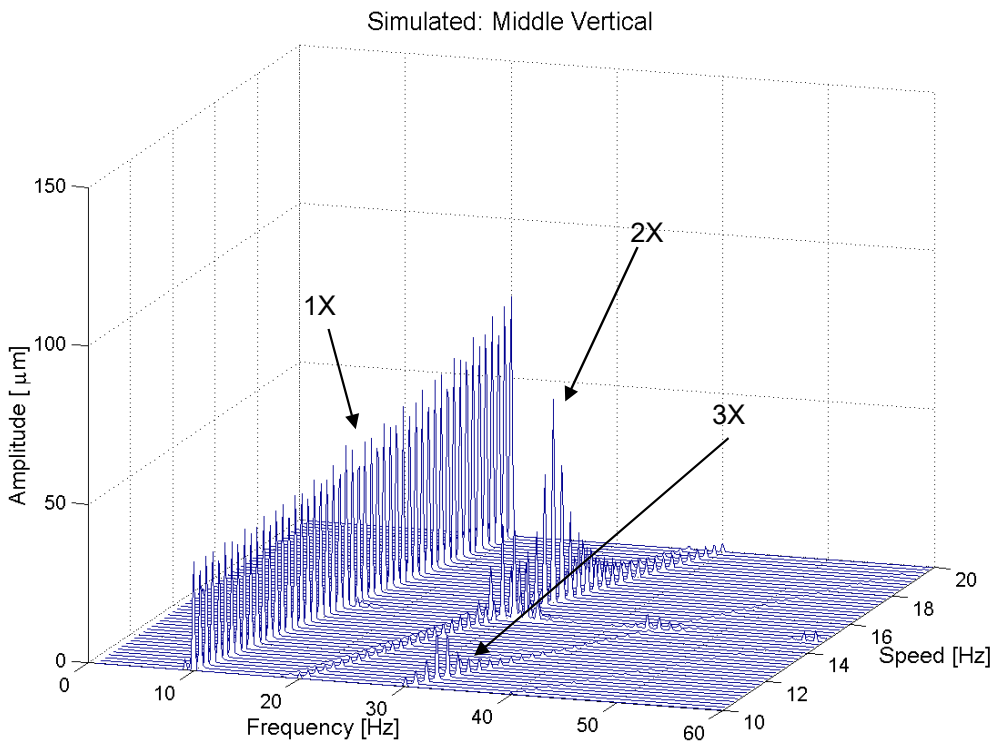


Figure 5.12 The simulated (Case 3) spectrum map of the vertical throw in the middle of the roll.

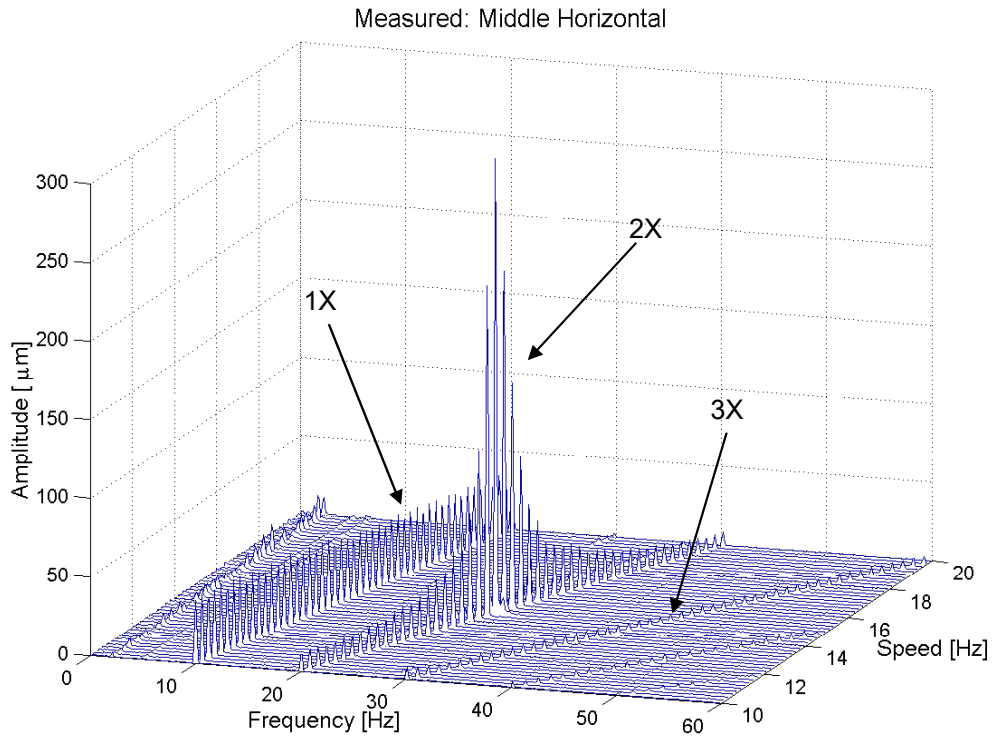


Figure 5.13 The measured spectrum map of the horizontal throw in the middle of the roll.

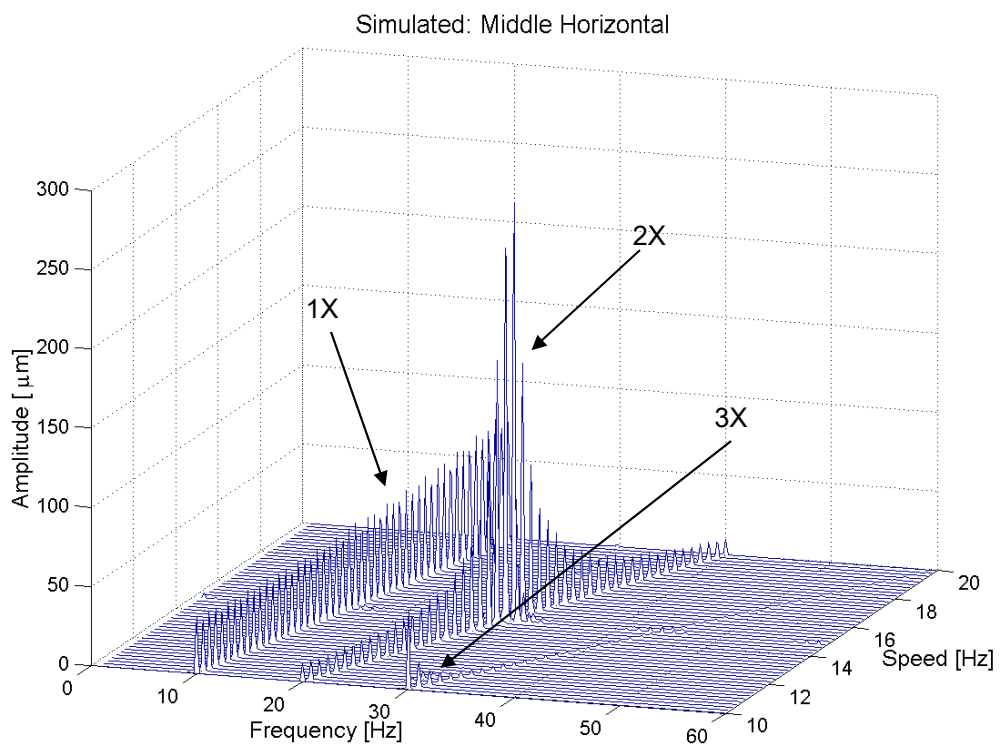


Figure 5.14 The simulated (Case 3) spectrum map of the horizontal throw in the middle of the roll.

5.3.2 Effect of Inertia Modeling of Roll

The mass matrix of a flexible body is a highly nonlinear function of the generalized coordinates of the body reference frame as well as of the deformation of the body. Some of the inertia invariants, which are described in Section 2.2.3, can be disabled and, in this way, the computational effort reduced. All the previous cases were run with all the invariants in the roll enabled. However, invariants \mathbf{I}^5 and \mathbf{I}^9 are computationally the most expensive, but their contribution to the results is negligible in some applications. For these reasons, Case 3 is re-analyzed by disabling invariants \mathbf{I}^5 and \mathbf{I}^9 . Invariant \mathbf{I}^5 is a second-order correction for the cross-coupling between the deformation and rotation of the body, while invariant \mathbf{I}^9 is a second-order correction for the inertia tensor of the body due to deformation. The spectrum map of the vertical displacement is shown in Figure 5.15. The spectrum map differs significantly from the measured one (Figure 5.11) as well as from that in Case 3 (Figure 5.12). A very strong unreal cross-coupling between the vertical and the horizontal direction was observed. In [90], it was shown that disabling invariant \mathbf{I}^9 did not affect the response of the roll significantly, and therefore, it can be said that invariant \mathbf{I}^5 is important in the analysis of the superharmonic vibrations of rotors. Furthermore, this example demonstrates that the coupling terms between the reference motion and deformation of a body cannot be neglected in the floating frame of reference formulation without compromising accuracy.

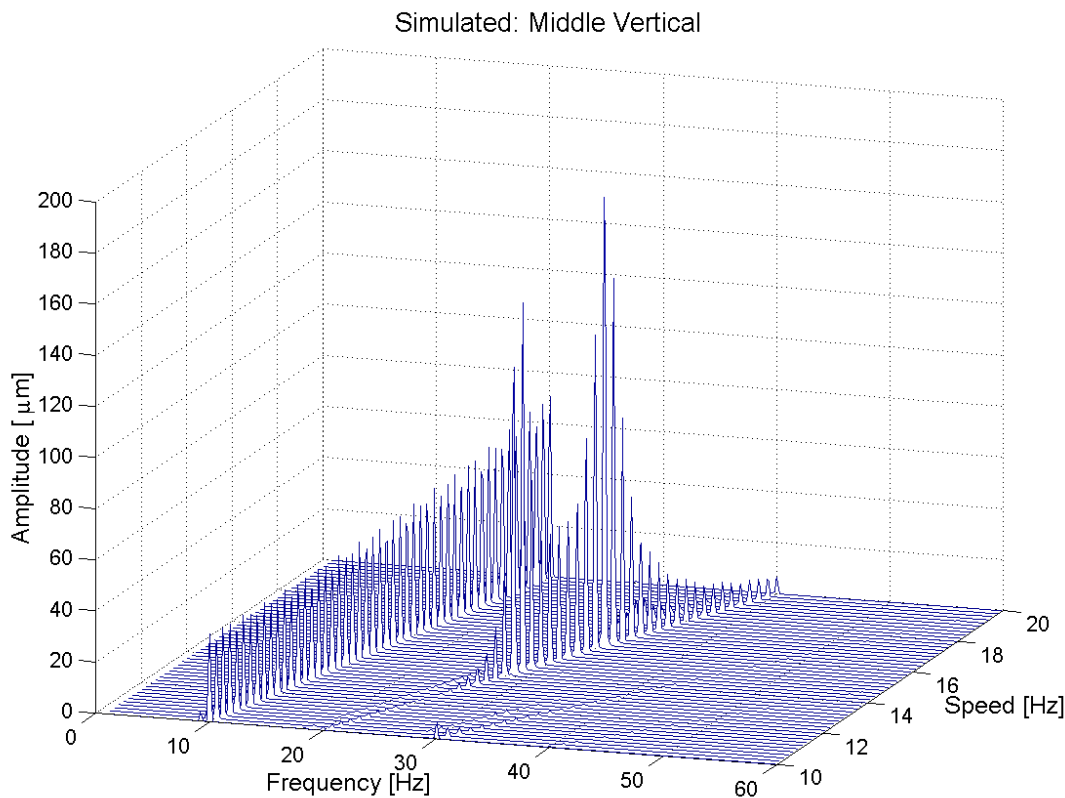


Figure 5.15 The simulated (Case 3) spectrum map of the vertical throw in the middle of the roll, when invariants \mathbf{I}^5 and \mathbf{I}^9 are disabled.

6 CONCLUSIONS

This thesis studied the dynamics of rotor-bearing systems through the use of a multibody simulation approach. The multibody simulation approach uses a general methodology that can describe the bodies that undergo large relative translational and rotational displacements. Accordingly, the multibody simulation approach does not make any assumptions regarding externally or internally applied forces. For these reasons, the multibody simulation can be used to describe the non-idealities of the rotor-bearing systems. It was shown that the superharmonic vibrations of complex rotor-bearing systems can be studied accurately by combining a detailed rotor model and bearing model in a multibody simulation approach.

The existing multibody formulations that can be used for the analysis of flexible rotors were discussed in the thesis. Geometrically nonlinear effects, such as centrifugal stiffening, may arise in high-speed rotor dynamics applications. However, the multibody formulations that are currently generally available are suitable for linear deformation analysis only. For these reasons, the nonlinear finite element formulations were discussed. In this work, the description of elastic forces in the absolute nodal coordinate formulation was improved by utilizing the exact displacement field. The absolute nodal coordinate formulation is a potential method for nonlinear geometrical analysis when considering high-speed rotor-bearing systems. A dynamic simulation model of a deep groove ball bearing, which includes distributed and localized defects, was developed in this study. The model includes descriptions of nonlinear Hertzian contact deformation and the elastohydrodynamic fluid film. The geometry, material properties and diametral clearance of the bearing are given as the input to the proposed model. The bearing force and torque components are calculated from the relative displacements and velocities between the bearing rings. The proposed ball bearing model can be used in a general multibody or rotor dynamics computer code as an interface element between the rotor and the housing.

The developed simulation approaches and models were applied in the analysis of two rotor-bearing systems. The first example was an electric motor supported by two ball bearings. Here, the bearings were modeled with the proposed ball bearing model. The bearing equations were solved simultaneously with the dynamic equations of the rotor system using a commercial multibody dynamics software application. The effect of the diametral clearance of the bearing on the natural frequencies and vibration response of the rotor-bearing system was studied. The diametral clearance was found to have a significant effect on the level of vibration as well as on the natural frequencies of the rotor-bearing system. Low-order waviness, also known as out-of-roundness, was found to generate vibration at frequencies of the waviness order multiplied by the rotation speed. The waviness orders close to the number of balls in the bearing ($z \pm 1$ and z) were found to generate vibrations at the ball passage inner ring and ball passage outer ring frequencies. Localized defects in the inner and outer rings were found to generate vibrations at the bearing defect frequencies. The simulated results were compared to the analytical results as well as to measurements reported in literature, and the above results were found to be in good agreement with each other.

The second practical example was a roller test rig that consists of a paper machine tube roll supported by a hard bearing type balancing machine. The modeled non-idealities were the variation in the shell thickness of the roll and the waviness of the rolling surfaces in the interface between the roll and support. These non-idealities were measured on the existing structure. The accuracy of the simulation model was improved through the use of the

results of the experimental modal analysis and optimization. The simulation model showed that the superharmonic vibrations are caused by these non-idealities. The simulation results were compared to those obtained by measuring the real structure. The comparison shows that the simulation model provides very good accuracy. Vibration responses are due to very small non-idealities in the physical structure and these non-idealities are difficult or even impossible to measure. Several simulation cases were run in such a way that the values of the input parameters of the model were varied. These variations were within the estimated error limits of the measured input data. The simulation results showed that the use of the multibody simulation approach allows equivalent responses to be achieved within the error limit of the input parameters. In addition, the use of the simulation model showed that the coupling terms in the mass matrix of the flexible body are important in rotor applications when using the floating frame of reference formulation.

The proposed simulation approach proved to a suitable method in nonlinear dynamic analysis and, in particular, for the superharmonic vibration analysis of rotor-bearing systems. The multibody simulation approach can be used to model non-ideal rotors; furthermore, the bearing forces can be non-linear functions of the system parameters. This work presented a model of a ball bearing, although other rolling element bearing types can also be modeled using the method developed in this work for ball bearings. The developed ball bearing model can be extended to include the centrifugal forces of the balls, in which case the accuracy of the model can be improved in high-speed applications. In some applications, such as in the backup bearings of the magnetic bearings, the assumption that no sliding between bearing components occurs might not be reasonable. Therefore, the accuracy of the model could be improved using a more detailed description of the bearing friction and lubrication.

The simulation approaches developed in this work can be applied to the research and product development of general rotor-bearing systems. As was shown in this study, rolling element bearings have a significant effect on the natural frequencies and the vibration characteristics of a rotor-bearing system. In order to take into account the effect of the bearings on the design process, a component library of various bearing types should be created. Using the component library, a design engineer could easily investigate the effect of bearing selection on the dynamical characteristics of a rotor system. The simulated vibration responses caused by various bearing defects could be used in the training of the condition monitoring software that recognizes the bearing failures. Simulation models, which include the waviness of the contacting surfaces, could be used to determine suitable manufacturing tolerances for the components of rotating machines. It is important to point out, that the computer simulation cannot totally eliminate the need for physical prototypes, since not all the non-idealities of a physical system can be identified. However, the simulation approach can be used to investigate the effect of individual parameters on the vibration response of a rotor-bearing system.

The absolute nodal coordinate formulation is a novel method for the analysis of flexible multibody systems. The absolute nodal coordinate formulation must be further developed in order to accurately simulate flexible rotors. Further areas of research include the development of three dimensional beam and shell elements, internal damping modeling, constraint modeling and efficient time-integration methods. Nevertheless, the absolute nodal coordinate formulation is a very promising method for the analysis of nonlinear deformation in multibody systems.

REFERENCES

- [1] Childs, D., 1993, *Turbomachinery Rotordynamics, Phenomena, Modeling, & Analysis*, John Wiley & Sons, New York.
- [2] Krämer, E., 1993, *Dynamics of Rotors and Foundations*, Springer-Verlag, Berlin.
- [3] Lalanne, M., and Ferraris, G., 1998, *Rotordynamics Prediction in Engineering, 2nd Edition*, John Wiley & Sons, West Sussex.
- [4] Rao, J. S., 1983, *Rotor Dynamics*, Wiley Eastern Limited, New Delhi.
- [5] Ishida, Y., and Inoue, T., 2001, “Internal Resonance of the Jeffcott Rotor with Nonlinear Spring Characteristic”, *Proceedings of DETC’01, ASME Design Engineering Technical Conferences and Computers and Information in Engineering Conference*, Pittsburgh, Pennsylvania, September 9-12.
- [6] Özgüven, H. N., and Özkan, Z., 1984, “Whirl Speeds and Unbalance Response of Multibearing Rotors Using Finite Elements”, *Journal of Vibration, Acoustics, Stress, and Reliability in Design*, **106**, pp. 72-79.
- [7] Kang, Y., Shih, Y.-P., and Lee, A.-C., 1992, “Investigation on the Steady-State Responses of Asymmetric Rotors”, *Journal of Vibration and Acoustics*, **114**, pp. 194-208.
- [8] Khulief, Y. A., and Mohiuddin, M. A., 1997, “On the Dynamic Analysis of Rotors Using Modal Reduction”, *Finite Elements in Analysis and Design*, **26**, pp. 41-55.
- [9] Zou, C.-P., Hua, H.-X., and Chen, D.-S., 2002, “Modal Synthesis Method of Lateral Vibration Analysis for Rotor-Bearing System”, *Computers and Structures*, **80**, pp. 2537-2549.
- [10] Ganesan, R., 2000, “Effects of Bearing and Shaft Asymmetries on the Instability of Rotors Operating at Near-Critical Speeds”, *Mechanism and Machine Theory*, **35**, pp. 737-752.
- [11] Childs, D. W., 2003, “Twice-Running-Speed Response Due to Elliptical Bearing Clearances”, *Journal of Vibration and Acoustics*, **125**, pp. 64-67.
- [12] Ehrich, F., 1992, “Observations of Subcritical Superharmonic and Chaotic Response in Rotordynamics”, *Journal of Vibration and Acoustics*, **93**, pp. 93-100.
- [13] Childs, D. W., 1982, “Fractional-Frequency Rotor Motion due to Non-Symmetric Clearance Effects”, *Journal of Engineering for Power*, **104**, pp. 533-541.
- [14] Ehrich, F. F., 1988, “High Order Subharmonic Response of High Speed Rotors in Bearing Clearance”, *Journal of Vibration, Acoustics, Stress, and Reliability in Design*, **110**, pp. 9-16.

- [15] El-Saeidy, F. M. A., 2000, "Finite-Element Dynamic Analysis of a Rotating Shaft with or without Nonlinear Boundary Conditions Subject to a Moving Load", *Nonlinear Dynamics*, **21**, pp. 377-408.
- [16] Hu, K., Mourelatos, Z. P., and Vlahopoulos, N., 2003, "Computational Analysis for Dynamic Response of a Rotating Shaft on Flexible Support Structure with Clearances", *Journal of Sound and Vibration*, **267**, pp. 1-28.
- [17] Brown, M. A., and Shabana, A. A., 1997, "Application of Multibody Methodology to Rotating Shaft Problems", *Journal of Sound and Vibration*, **204**, pp. 439-457.
- [18] Al-Bedoor, B. O., 2001, "Modeling the Coupled Torsional and Lateral Vibrations of Unbalanced Rotors", *Computer Methods in Applied Mechanics and Engineering*, **190**, pp. 5999-6008.
- [19] Keskiniva, M., 1997, Simulation and Balancing of Flexible Rotors in Terms of Semidefinite Modal Coordinates, Doctoral Thesis, Tampere University of Technology.
- [20] El-Absy, H., and Shabana, A. A., 1996, "Coupling Between Rigid Body and Deformation Modes", *Journal of Sound and Vibration*, **198**, pp. 617-637.
- [21] Shabana, A. A., 1998, *Dynamics of Multibody Systems, 2nd Edition*, John Wiley & Sons, New York.
- [22] Mayo, J., Dominguez, J., and Shabana, A. A., 1995, "Geometrically Nonlinear Formulations of Beams in Flexible Multibody Dynamics", *Journal of Vibration and Acoustics*, **117**, pp. 501-509.
- [23] Shabana, A. A., 2001, *Computational Dynamics, 2nd Edition*, John Wiley & Sons, New York.
- [24] ADAMS Online Documentation, 2001, version 12.0, Mechanical Dynamics, Inc, Ann Arbor, Michigan, USA.
- [25] Yeh, H.-F., and Dopker, B., 1990, "Deformation Mode Selection and Mode Orthonormalization for Flexible Body System Dynamics", *Computers & Structures*, **34**, pp. 615-627.
- [26] Friberg, O., 1991, "A Method for Selecting Deformation Modes in Flexible Multibody Dynamics", *International Journal for Numerical Methods in Engineering*, **32**, pp. 1637-1655.
- [27] Yoo, W. S., and Haug, E. J., 1986, "Dynamics of Mechanical Systems Using Vibration and Static Correction Modes", *Journal of Mechanisms, Transmissions, and Automation in Design*, **108**, pp. 315-322.
- [28] Craig, R. R., and Bampton, M. C. C., 1968, "Coupling of Substructures for Dynamic Analyses", *AIAA Journal*, **6**, pp. 1313-1319.
- [29] Schwertassek, R., Wallrapp, O., and Shabana, A. A., 1999, "Flexible Multibody Dynamics and Choice of Shape Functions", *Nonlinear Dynamics*, **20**, pp. 361-380.

- [30] Agrawal, O. P., and Shabana, A. A., 1985, "Dynamic Analysis of Multibody Systems Using Component Modes", *Computers & Structures*, **21**, pp. 1303-1312.
- [31] Shabana, A. A., 1996, "Resonance Conditions and Deformable Body Co-Ordinate Systems", *Journal of Sound and Vibration*, **192**, pp. 389-398.
- [32] Ambrósio, J. A. C., 1996, "Dynamics of Structures Undergoing Gross Motion and Nonlinear Deformations: a Multibody Approach", *Computers & Structures*, **59**, pp. 1001-1012.
- [33] Belytschko, T., and Hsieh, B. J., 1973, "Nonlinear Transient Finite Element Analysis with Convected Coordinates", *International Journal for Numerical Methods in Engineering*, **7**, pp. 255-271.
- [34] Rankin, C. C., and Brogan, F. A., 1986, "An Independent Corotational Procedure for the Treatment of Large Rotations", *ASME Journal of Pressure Vessel Technology*, **108**, pp. 165-174.
- [35] Campanelli, M., Berzeri, M., and Shabana, A. A., 2000, "Performance of the Incremental and Non-Incremental Finite Element Formulations in Flexible Multibody Problems", *Journal of Mechanical Design*, **122**, pp. 1-10.
- [36] ANSYS User's Manual, 2001, Theory, Twelfth Edition, SAS IP, Inc. ©.
- [37] Shabana, A. A., 1996, "Finite Element Incremental Approach and Exact Rigid Body Inertia", *Journal of Mechanical Design*, **118**, pp. 171-178.
- [38] Shabana, A. A., 1997, "Flexible Multibody Dynamics: Review of Past and Recent Developments", *Multibody System Dynamics*, **1**, pp. 189-222.
- [39] Wasfy, T. M., and Noor, A. K., 2003, "Computational Strategies for Flexible Multibody Dynamics", *Applied Mechanics Reviews*, **56**, pp. 553-613.
- [40] Simo, J. C., 1985, "A Finite Strain Beam Formulation. The Three-Dimensional Dynamic Problem. Part I", *Computer Methods in Applied Mechanics and Engineering*, **49**, pp. 55-70.
- [41] Simo, J. C., and Vu-Quoc, L., 1986, "A Three-Dimensional Finite-Strain Rod Model. Part II: Computational Aspects", *Computer Methods in Applied Mechanics and Engineering*, **58**, pp. 79-116.
- [42] Cardona, A., and Geradin, M., 1988, "A Beam Finite Element Non-Linear Theory with Finite Rotations", *International Journal for Numerical Methods in Engineering*, **26**, pp. 2403-2438.
- [43] Avello, A., and García de Jalón, J., 1991, "Dynamics of Flexible Multibody Systems Using Cartesian Co-ordinates and Large Displacement Theory", *International Journal for Numerical Methods in Engineering*, **32**, pp. 1543-1563.
- [44] Jelenić, G., and Saje, M., 1995, "A Kinematically Exact Space Finite Strain Beam Model – Finite Element Formulation by Generalized Virtual Work Principle", *Computer Methods in Applied Mechanics and Engineering*, **120**, pp. 131-161.

- [45] Ibrahimbegović, A., 1995, "On the Finite Element Implementation of Geometrically Nonlinear Reissner's Beam Theory: Three-Dimensional Curved Beam Elements", *Computer Methods in Applied Mechanics and Engineering*, **122**, pp. 11-26.
- [46] Jelenić, G., and Crisfield, M. A., 1998, "Interpolation of Rotational Variables in Nonlinear Dynamics of 3D Beams", *International Journal for Numerical Methods in Engineering*, **43**, pp. 1193-1222.
- [47] Jelenić, G., and Crisfield, M. A., 1999, "Geometrically Exact 3D Beam Theory: Implementation of a Strain-Invariant Finite Elements for Statics and Dynamics", *Computer Methods in Applied Mechanics and Engineering*, **171**, pp. 141-171.
- [48] Géradin, M., and Cardona, A., 2001, *Flexible Multibody Dynamics: A Finite Element Approach*, John Wiley & Sons, West Sussex.
- [49] Shabana, A.A., and Yakoub, R.Y., 2001, "Three Dimensional Absolute Nodal Coordinate Formulation for Beam Elements: Theory", *Journal of Mechanical Design*, **123**, pp. 606-613.
- [50] Yakoub, R.Y., and Shabana, A.A., 2001, "Three Dimensional Absolute Nodal Coordinate Formulation for Beam Elements: Implementation and Application", *Journal of Mechanical Design*, **123**, pp. 614-621.
- [51] Mikkola, A. M., and Shabana, A. A., 2003, "A Non-Incremental Finite Element Procedure for the Analysis of Large Deformations of Plates and Shells in Mechanical System Applications", *Multibody System Dynamics*, **9**, pp. 283-309.
- [52] Choi, S. H., Pierre, C., and Ulsoy, A. G., 1992, "Consistent Modeling of Rotating Timoshenko Shafts Subject to Axial Loads", *Journal of Vibration and Acoustics*, **114**, pp. 249-259.
- [53] Sapanen, J., and Mikkola, A., 2003, "Description of Elastic Forces in Absolute Nodal Coordinate Formulation", *Nonlinear Dynamics*, **34**, pp. 53-74.
- [54] Sapanen, J. T., and Mikkola, A. M., 2003, "Studies on the Stiffness Properties of the Absolute Nodal Coordinate Formulation for Three-Dimensional Beams", *Proceedings of DETC'03, ASME Design Engineering Technical Conferences and Computers and Information in Engineering Conference*, Chicago, Illinois, DETC2003/VIB-48325.
- [55] Omar, M.A., and Shabana, A.A., 2001, "A Two-Dimensional Shear Deformation Beam for Large Rotation and Deformation", *Journal of Sound and Vibration*, **243**, pp. 565-576.
- [56] Sugiyama, H., Escalona, J. L., and Shabana, A. A., 2003, "Formulation of Three-Dimensional Joint Constraints Using the Absolute Nodal Coordinates", *Nonlinear Dynamics*, **31**, pp. 167-195.
- [57] Berzeri, M., and Shabana, A. A., 2000, "Development of Simple Models for the Elastic Forces in the Absolute Nodal Coordinate Formulation", *Journal of Sound and Vibration*, **235**, pp. 539-565.

- [58] Hauptmann, R., Doll, S., Harnau, M., and Schweizerhof, K., 2001, "Solid-Shell Elements with Linear and Quadratic Shape Functions at Large Deformations with Nearly Incompressible Materials", *Computers and Structures*, **79**, pp. 1671-1685.
- [59] Dufva, K., Sapanen, J., and Mikkola, A. "A Two-Dimensional Shear Deformable Beam Element Based on the Absolute Nodal Coordinate Formulation", *Journal of Sound and Vibration*, In Press.
- [60] Aktürk, N., Uneeb, M., and Gohar, R., 1997, "The Effects of Number of Balls and Preload on Vibrations Associated With Ball Bearings", *Journal of Tribology*, **119**, pp. 747-753.
- [61] Tiwari, M., Gupta, K., and Prakash, O., 2000, "Effect of Radial Internal Clearance of a Ball Bearing on the Dynamics of a Balanced Horizontal Rotor", *Journal of Sound and Vibration*, **238**, pp. 723-756.
- [62] Tiwari, M., Gupta, K., and Prakash, O., 2000, "Dynamic Response of an Unbalanced Rotor Supported on Ball Bearings", *Journal of Sound and Vibration*, **238**, pp. 757-779.
- [63] Tandon, N., and Choudhury, A., 1999, "A Review of Vibration and Acoustic Measurement Methods for the Detection of Defects in Rolling Element Bearings", *Tribology International*, **32**, pp. 469-480.
- [64] Gupta, P. K., 1988, "On the Geometrical Imperfections in Ball Bearings", *Journal of Tribology*, **110**, pp. 19-25.
- [65] Wardle, F. P., 1988, "Vibration Forces Produced by Waviness of the Rolling Surfaces of Trust Loaded Ball Bearing, Part 1: Theory", *Proceedings of the Institution of Mechanical Engineers, Journal of Mechanical Engineering Science*, **202(C)**, pp. 305-312.
- [66] Wardle, F. P., 1988, "Vibration Forces Produced by Waviness of the Rolling Surfaces of Trust Loaded Ball Bearing, Part 2: Experimental Validation", *Proceedings of the Institution of Mechanical Engineers, Journal of Mechanical Engineering Science*, **202(C)**, pp. 313-319.
- [67] Yhland, E., 1992, "A Linear Theory of Vibration Caused by Ball Bearings With Form Errors Operating at Moderate Speed", *Journal of Tribology*, **114**, pp. 348-359.
- [68] Aktürk, N., 1999, "The Effect of Waviness on Vibrations Associated With Ball Bearings", *Journal of Tribology*, **121**, pp. 667-677.
- [69] Lyhagh, N., Rahnejat, H., Ebrahimi, M., and Aini, R., 2000, "Bearing induced Vibration in Precision High Speed Spindles", *International Journal of Machine Tools & Manufacture*, **40**, pp. 561-577.
- [70] Jang, G. H., and Jeong, S. W., 2002, "Nonlinear Excitation Model of Ball Bearing Waviness in a Rigid Rotor Supported by Two or More Ball Bearings Considering Five Degrees of Freedom", *Journal of Tribology*, **124**, pp. 82-90.

- [71] Tandon, N., and Choudhury, A., 1997, "An Analytical Model for The Prediction of the Vibration Response of Rolling Element Bearings Due to a Localized Defect", *Journal of Sound and Vibration*, **205**, pp. 275-292.
- [72] Taylor, J. I., 1994, *The Vibration Analysis Handbook, First Edition*, Vibration Consultants Inc., Tampa.
- [73] Lee, Y.-S., and Lee, C.-W., 1999, "Modelling and Vibration Analysis of Misaligned Rotor-Ball Bearing Systems", *Journal of Sound and Vibration*, **224**, pp. 17-32.
- [74] Hamrock, B. J., 1994, *Fundamentals of Fluid Film Lubrication*, McGraw-Hill, New York.
- [75] Hamrock, B. J., and Dowson, D., 1976, "Isothermal Elastohydrodynamic Lubrication of Point Contacts. Part I—Theoretical Formulation", *Journal of Lubrication Technology*, **98**, pp. 223-229.
- [76] Brewe, D. E., and Hamrock, B. J., 1977, "Simplified Solution for Elliptical-Contact Deformation Between Two Elastic Solids", *Journal of Lubrication Technology*, **99**, pp. 485-487.
- [77] Hamrock, B. J., and Dowson, D., 1977, "Isothermal Elastohydrodynamic Lubrication of Point Contacts. Part III—Fully Flooded Results", *Journal of Lubrication Technology*, **99**, pp. 264-276.
- [78] Harris, T. A., 1990, *Rolling Bearing Analysis, Third Edition*, John Wiley & Sons, New York.
- [79] Hamrock, B. J., and Dowson, D., 1981, *Ball Bearing Lubrication*, John-Wiley & Sons, New York.
- [80] SKF Bearing Handbook, 1991, Turin.
- [81] Sapanen, J. and Mikkola, A., 2003, "Dynamic Model of a Deep Groove Ball Bearing Including Localized and Distributed Defects, Part 1: Theory", *Proceedings of the Institution of Mechanical Engineers, Journal of Multi-body Dynamics*, **217(K)**, pp. 201-211.
- [82] Dietl, P., Wensing, J., and van Nijen, G. C., 2000, "Rolling Bearing Damping for Dynamic Analysis of Multi-body Systems – Experimental and Theoretical Results", *Proceedings of the Institution of Mechanical Engineers, Journal of Multi-Body Dynamics*, **214(K)**, pp. 33-43.
- [83] Mitsuya, Y., Sawai, H., Shimizu, M., and Aono, Y., 1998, "Damping in Vibration Transfer Through Deep-Groove Ball Bearings", *Journal of Tribology*, **120**, pp. 413-420.
- [84] Aini, R., Rahnejat, H., and Gohar, R., 2002, "Vibration Modeling of Rotating Spindles Supported by Lubricated Bearings", *Journal of Tribology*, **124**, pp. 158-165.

- [85] Hannukainen, P., Sopenan, J., and Mikkola A., 2003, "Subharmonic Vibrations of a Roll Tube Supported by Plain Journal Bearings", *Proceedings of the Institution of Mechanical Engineers, Journal of Multi-body Dynamics*, **217**(K), pp. 301-312.
- [86] Sohoni, W. E., and Whitesell, J., 1986, "Automatic Linearization of Constrained Dynamical Models", *Journal of Mechanisms, Transmission and Automation in Design*, **108**, pp. 300-304.
- [87] Sopenan, J. and Mikkola, A., 2003, "Dynamic Model of a Deep Groove Ball Bearing Including Localized and Distributed Defects, Part 2: Implementation and Results", *Proceedings of the Institution of Mechanical Engineers, Journal of Multi-body Dynamics*, **217**(K), pp. 213-223.
- [88] Kuosmanen, P., Juhanko, J., Porkka, E., Valkonen, A., and Järviluoma, M., 2002, Active Vibration Control of Large-Scale Rotors, ICMA'02 Conference, Tampere, Finland, pp. 411-417.
- [89] Juhanko, J., and Porkka, E., 2001, "PyöriVÄRE – Telakoelaitteen verifiointimittaukset – roottori tukirullilla [PyöriVÄRE – Verification Measurements of the Roller Test Rig – Balancing Machine Support]", Helsinki University of Technology Reports in Machine Design 2/2001.
- [90] Sopenan, J., 2003, "Multibody Simulation Model of the Roller Test Rig", *Research Report 46*, Department of Mechanical Engineering, Lappeenranta University of Technology.
- [91] Sopenan, J., and Mikkola, A., 2000, "Study of sub-harmonic vibration of a tube roll using simulation model", *2nd Triennial International Symposium on Multi-body Dynamics: Monitoring & Simulation Techniques*, June 26 – 27, Bradford, UK, pp. 57-68.
- [92] Kantola, K., 2000, "Paperitelan Moodianalyysi [Modal analysis of the test roll]", Measurement report, Helsinki University of Technology, Laboratory of Mechanics of Materials.
- [93] Eschmann, P., Hasbargen, L., and Brändlein, J., 1986, *Ball and Roller Bearings, Theory, Design and Application, 2nd edition*, John Wiley and Sons, New York.
- [94] Råde, L., and Westergren, B., 1995, *Beta - Mathematics Handbook for Science and Engineering*, Studentlitteratur, Lund, Sweden.
- [95] Lampinen, J., 1999, "Differential Evolution – New Naturally Parallel Approach for Engineering Design Optimization", In: *Barry H.V. Topping (ed.), 1999, Developments in Computational Mechanics with High Performance Computing*, Civil-Comp Press, Edinburgh (Scotland), pp. 217-228.
- [96] Kilkki, J., 2002, Automated Formulation of Optimisation Models for Steel Structures, Doctoral Thesis, Lappeenranta University of Technology.

In the finite segments approach, the local forces and torques affecting body i can be written as follows:

$$\begin{bmatrix} \bar{\mathbf{F}}^{ij} \\ \bar{\mathbf{T}}^{ij} \end{bmatrix} = -\mathbf{K}_b \begin{bmatrix} \mathbf{d}_b \\ \boldsymbol{\theta}_b \end{bmatrix} - \mathbf{D}_b \begin{bmatrix} \dot{\mathbf{d}}_b \\ \dot{\boldsymbol{\theta}}_b \end{bmatrix}, \quad (\text{A.1})$$

where $\bar{\mathbf{F}}^{ij} = [\bar{F}_x^{ij} \ \bar{F}_y^{ij} \ \bar{F}_z^{ij}]^T$, $\bar{\mathbf{T}}^{ij} = [\bar{T}_x^{ij} \ \bar{T}_y^{ij} \ \bar{T}_z^{ij}]^T$, $\mathbf{d}_b = [d_x - l \ d_y \ d_z]^T$ and $\boldsymbol{\theta}_b = [\theta_x \ \theta_y \ \theta_z]^T$. The stiffness matrix can be written as follows:

$$\mathbf{K}_b = \begin{bmatrix} k_{11} & 0 & 0 & 0 & 0 & 0 \\ & k_{22} & 0 & 0 & 0 & k_{26} \\ & & k_{33} & 0 & k_{35} & 0 \\ & & & k_{44} & 0 & 0 \\ & \text{symm.} & & & k_{55} & 0 \\ & & & & & k_{66} \end{bmatrix}, \quad (\text{A.2})$$

whose non-zero elements can be expressed as follows:

$$\begin{aligned} k_{11} &= \frac{EA}{l}, & k_{22} &= \frac{12EI_{zz}}{l^3(1+\phi_y)}, & k_{26} &= \frac{6EI_{zz}}{l^2(1+\phi_y)}, & k_{33} &= \frac{12EI_{yy}}{l^3(1+\phi_z)}, \\ k_{35} &= \frac{6EI_{yy}}{l^2(1+\phi_z)}, & k_{44} &= \frac{GJ}{l}, & k_{55} &= \frac{(4+\phi_z)EI_{yy}}{l(1+\phi_z)}, & k_{55} &= \frac{(4+\phi_y)EI_{zz}}{l(1+\phi_y)} \end{aligned}$$

$$\text{and } \phi_z = \frac{12EI_{yy}}{k_{sy}GAl^2}, \quad \phi_y = \frac{12EI_{zz}}{k_{sz}GAl^2}$$

In the above equations, A is the area of the cross-section of the beam, E and G are the modulus of elasticity and rigidity of the material, respectively, I_{yy} and I_{zz} are the second moments of the area, k_{sy} and k_{sz} are the shear correction factors, J is the torsion constant and l is the undeformed length of the beam, as shown in Figure A.1.

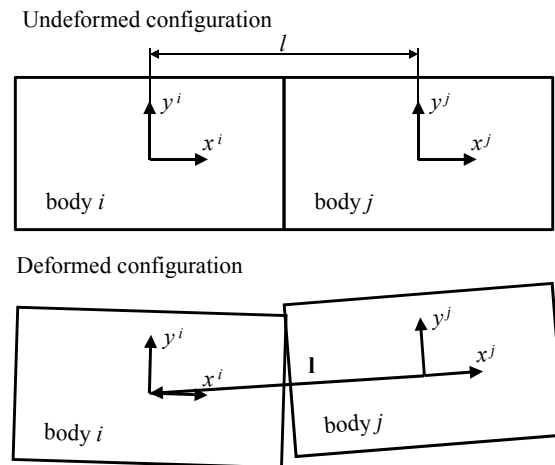


Figure A.1 The undeformed and deformed configuration of bodies i and j .

The frequency domain or spectral analysis of a vibration signal is widely used in the detection of bearing defects. Each element in a rolling element bearing has a characteristic rotational frequency, and a defect in that particular element increases the vibration energy at that nominal frequency. Bearing defect frequencies are widely known and can be calculated from the rotational frequency and bearing dimensions. The following equations apply for a bearing in which the outer ring is fixed and no skidding or slipping occurs [78].

The rotational frequency of the cage is

$$f_c = \frac{f_s}{2} \left(1 - \frac{d}{d_m} \cos \phi \right) \quad (\text{B.1})$$

The inner ring defect frequency (ball-pass-inner-ring frequency) is

$$f_{bpir} = \frac{zf_s}{2} \left(1 + \frac{d}{d_m} \cos \phi \right) \quad (\text{B.2})$$

The outer ring defect frequency (ball-pass-outer-ring frequency) is

$$f_{bpor} = zf_c \quad (\text{B.3})$$

The rolling element defect frequency (the rotational speed of the rolling element around its own axis) is

$$f_{re} = \frac{f_s d_m}{2d} \left(1 - \left(\frac{d}{d_m} \cos \phi \right)^2 \right), \quad (\text{B.4})$$

where f_s is the rotational speed of the inner ring and ϕ the contact angle. It has been reported that skidding and ball slipping slightly alter these frequencies [63].

The dimensions of studied paper machine tube roll are shown in Figure C.1.

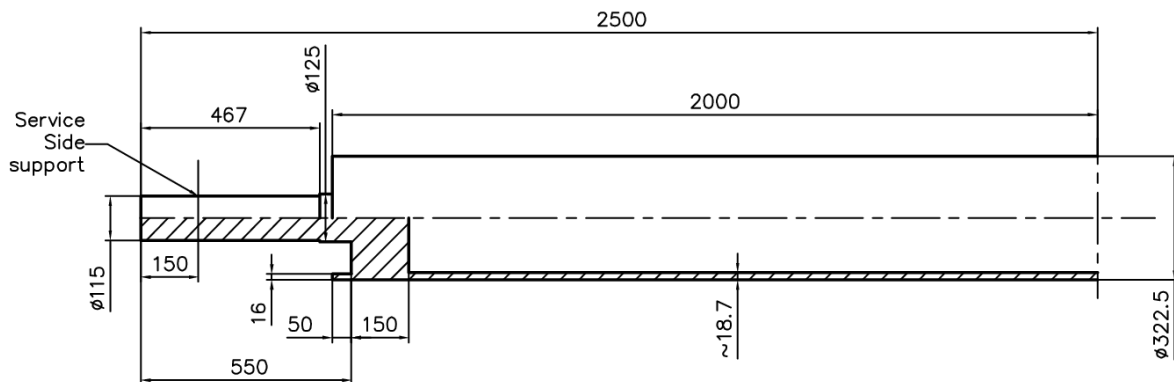


Figure C.1 The dimensions of the roll.

The coordinate system shown in Figure C.2 is used in the simulation model of the roll.

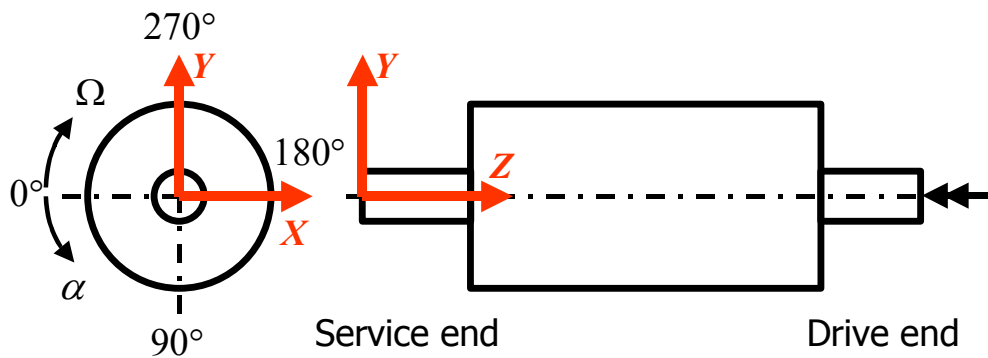


Figure C.2 The right-handed coordinate system is at the service side end of the roll and the attitude angle, α , increases counterclockwise. The rotation direction is negative around the Z-axis.

The non-ideality of two roll models can be seen in the mass properties and the natural frequencies shown in Table D.1. The locations of the center of mass are not in the neutral axis and the cross-products of inertia are not equal to zero. The frequencies of the bending mode pairs are not equal as they would be in the case of an ideal roll.

Table D.1 The mass properties and selected modes of two roll models.

	Measured shell thickness variation	Two-fold shell thickness variation
Mass of the roll [kg]	791.11	791.18
Center of mass relative to service end [mm, mm, mm]	[-0.010, -0.053, 2499.705]	[-0.019, -0.106, 2499.416]
Inertia tensor relative to service end [kgm ²]	$\begin{bmatrix} 6649.99 & 0.005 & 0.024 \\ & 6650.01 & 0.070 \\ \text{symm.} & & 14.53 \end{bmatrix}$	$\begin{bmatrix} 6648.11 & 0.010 & 0.047 \\ & 6648.15 & 0.141 \\ \text{symm.} & & 14.53 \end{bmatrix}$
Frequencies of the selected modes [Hz] (b) = bending mode pair, (l) = longitudinal mode, (s) = boundary mode pair	77.76 / 77.90 (b)	77.69 / 77.97 (b)
	199.95 / 200.17 (b)	199.80 / 200.24 (b)
	279.64 / 279.74 (b)	279.54 / 279.74 (b)
	348.53 / 348.65 (b)	348.43 / 348.68 (b)
	464.54 (l)	464.82 (l)
	523.26 / 523.54 (b)	522.83 / 523.40 (b)
	778.75 / 779.04 (b)	778.48 / 779.09 (b)
	982.45 (l)	981.13 (l)
	1054.41 / 1054.60 (b)	1053.66 / 1054.04 (b)
	1301.37 / 1301.65 (b)	1301.17 / 1301.70 (b)
	1460.24 / 1460.94 (b)	1457.36 / 1459.85 (b)
	1595.25 / 1596.37 (b)	1594.53 / 1596.75 (b)
	11941.95 / 11982.07 (s)	11886.71 / 11965.07 (s)

The measured shell thickness of the roll is shown in Figure E.1. Since the finite element mesh used in the model is not of the same size as the grid used in the measurement, a cubic interpolation method is used to obtain the shell thickness at the nodal points.

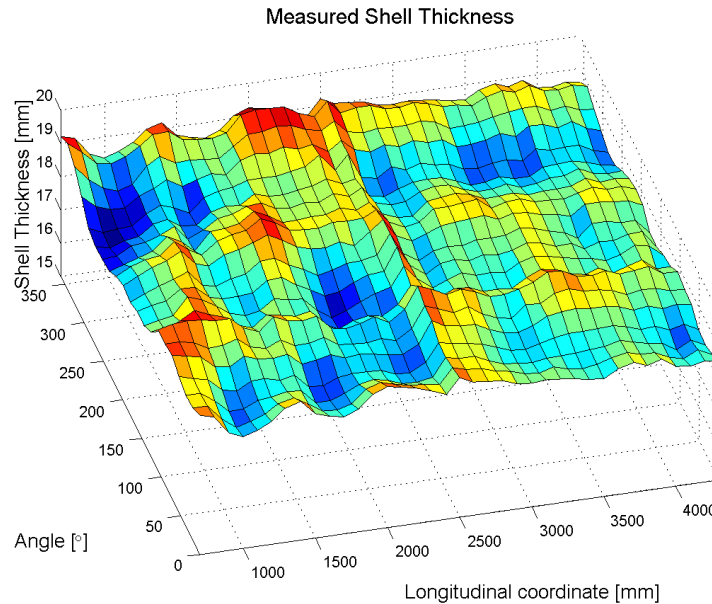


Figure E.1 The measured shell thickness of the roll. The shell thickness is measured at 740 points. The number of evenly distributed measurement points in the circumferential direction is 20 and 37 in the longitudinal direction.

Figure E.2 shows the measured waviness components of the rolling surfaces of the shafts of the roll.

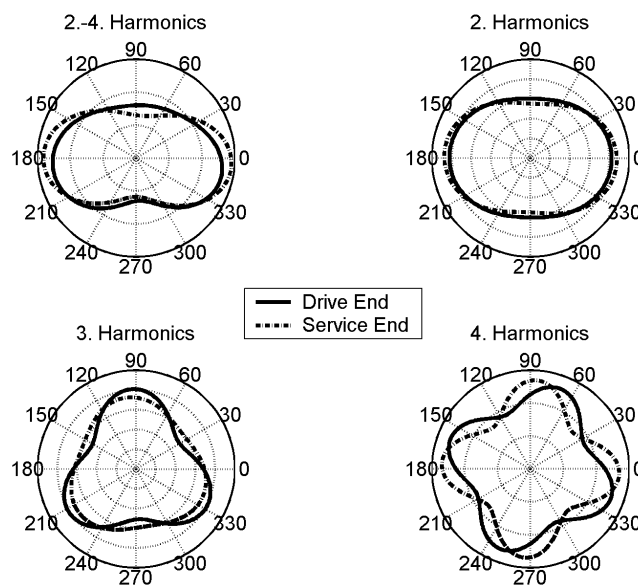


Figure E.2 A graphical representation of the waviness of the shaft.

The selected target function for the optimization, Y_{opt} , can be written as

$$Y_{opt} = \sum_{i=1}^{10} y_i, \text{ where} \quad (F.1)$$

$$y_i = \begin{cases} C_i \cdot |f_i - f_{mea i}|, & \left| 1 - \frac{c_i}{c_{mea i}} \right| \leq 0.10 \\ C_i \cdot \left[10 \cdot |c_i - c_{mea i}| + |f_i - f_{mea i}| \right], & \left| 1 - \frac{c_i}{c_{mea i}} \right| > 0.10 \end{cases}$$

where y_i is the target function value for mode i , C_i is the weighting factor of mode i , c_i is the modal damping ratio in the model, $c_{mea i}$ is the measured damping ratio and f_i and $f_{mea i}$ are the calculated and measured frequencies, respectively. The error estimate for the measured damping is $\pm 10\%$ as a result of which the damping error is neglected if it is less than 10% . Because the absolute error is used, the damping error is multiplied by a factor of 10 in order to increase its significance.

The selection of the optimization design variables, i.e. the input parameters is not a trivial task. The design variables should have a significant effect on the target function. Furthermore, they should be unambiguous, unlike the serial-connected spring coefficient, where the combined spring constant is achieved with an infinite number of solutions. The selected design variables, shown in Figure F.1, are the stiffness and damping coefficients of the spring-damper forces and the modal damping ratios of the flexible parts. The modal damping ratios are defined according to the frequency of the modes. The modes, the frequency of which is higher than that shown in Figure F.1, are critically damped, i.e. the damping ratio is set to 100% .

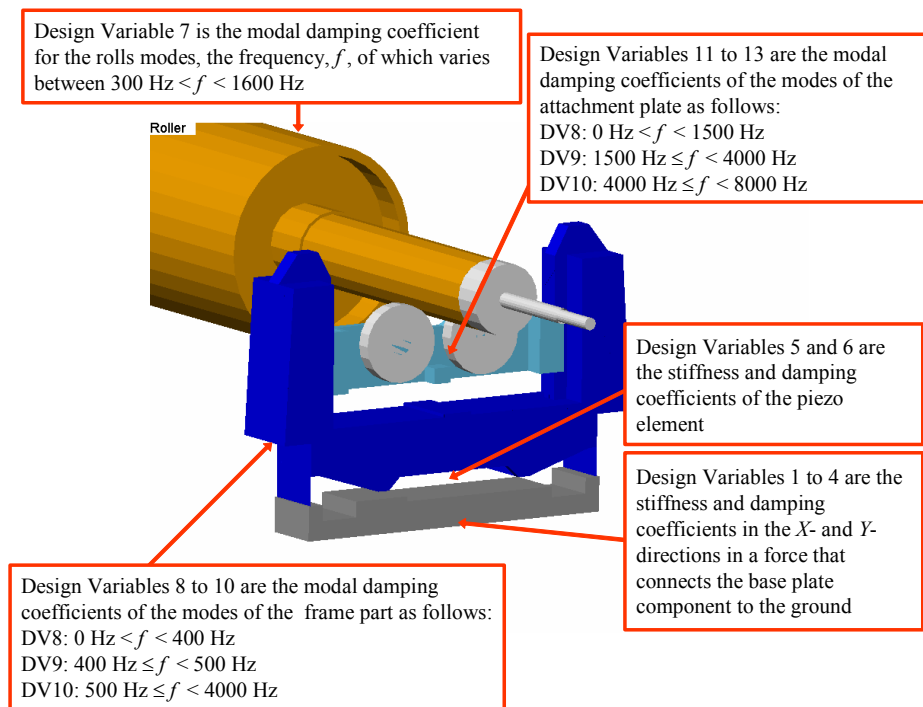


Figure F.1 The design variables used in the optimization.

The optimization results that are used in simulation cases 1 - 3 and 5 – 6 are shown in Table F.1, and the values of the optimized design variables are shown in Table F.2. Correspondingly, the optimization results used in simulation cases 4 and 7 are shown in Table F.3, and the values of the optimized design variables are shown in Table F.4.

Table F.1 The optimization results used in simulation cases 1-3 and 5-6.

Mode	Measured		Simulated								Weight. factor	Target function (absolute error)	
	Damp. %	Freq. [Hz]	Before Optimization				After Optimization					C	Before
			Damp. %	Error %	Freq. [Hz]	Error %	Damp. %	Error %	Freq. [Hz]	Error %			
1 (h)	0.608	29.83	0.344	43.4%	29.43	1.4%	0.580	4.6%	29.83	0.0%	10	30.432	0.021
2 (v)	1.060	32.16	0.286	73.0%	32.02	0.4%	1.137	-7.3%	32.08	0.2%	10	78.841	0.787
3 (h)	1.330	65.34	1.515	-13.9%	63.79	2.4%	1.388	-4.4%	65.68	-0.5%	5	16.977	1.681
4 (v)	1.680	82.23	1.406	16.3%	79.95	2.8%	1.847	-9.9%	81.09	1.4%	2	10.034	2.278
5 (h)	1.590	111.59	1.893	-19.1%	108.43	2.8%	1.748	-9.9%	110.93	0.6%	5	30.963	3.284
6 (v)	1.850	140.00	1.553	16.1%	138.82	0.8%	1.408	23.9%	140.15	-0.1%	2	8.300	9.143
7 (h)	2.100	179.04	1.927	8.2%	182.40	-1.9%	2.278	-8.5%	185.27	-3.5%	1.25	4.201	7.783
8 (h)	2.030	206.62	1.413	30.4%	224.18	-8.5%	1.884	7.2%	226.35	-9.6%	1.25	29.668	24.666
9 (v)	1.540	267.00	1.551	-0.7%	258.21	3.3%	1.694	-10.0%	259.24	2.9%	0.625	5.493	4.853
10 (h)	1.120	282.78	0.682	39.1%	307.97	-8.9%	1.011	9.7%	308.41	-9.1%	0.625	18.481	16.017
h = horizontal mode v = vertical mode			Mean:	26.0%	Mean:	3.3%	Mean:	9.5%	Mean:	2.8%	Sum:	233.39	70.51
												Improvement:	69.8%

Table F.2 The values of the optimized design variables used in simulation cases 1-3 and 5-6.

Desing Variable		Range min - max	Initial Value	Optimal Value
#	Type and Units			
1	Stiffness coefficient [MN/m]	100 - 2500	700	108.67
2	Stiffness coefficient [MN/m]	100 - 2500	700	302.74
3	Damping coefficient [Ns/mm]	1 - 100000	1000	8873.62
4	Damping coefficient [Ns/mm]	1 - 100000	1000	2238.97
5	Stiffness coefficient [MN/m]	60 - 80	70	75.69
6	Damping coefficient [Ns/mm]	1 - 100	5	9.32
7	Damping ratio [%]	0.01 - 10.00	0.50	0.72
8	Damping ratio [%]	0.05 - 20.00	0.50	10.61
9	Damping ratio [%]	0.05 - 20.00	0.50	6.61
10	Damping ratio [%]	0.05 - 20.00	0.50	20.00
11	Damping ratio [%]	0.05 - 20.00	0.50	18.78
12	Damping ratio [%]	0.05 - 20.00	0.50	16.77
13	Damping ratio [%]	0.05 - 20.00	0.50	18.11

Table F.3 The optimization results used in simulation cases 4 and 7.

Mode	Measured		Simulated								Weight. factor	Target function (absolute error)	
	Damp. %	Freq. [Hz]	Before Optimization				After Optimization					C	Before
			Damp. %	Error %	Freq. [Hz]	Error %	Damp. %	Error %	Freq. [Hz]	Error %			
1 (h)	0.608	29.83	0.344	43.4%	29.43	1.4%	0.556	8.6%	29.79	0.1%	10	30.432	0.420
2 (v)	0.900	32.16	0.286	68.2%	32.02	0.4%	0.901	-0.1%	32.03	0.4%	10	62.841	1.331
3 (h)	1.330	65.34	1.515	-13.9%	63.79	2.4%	1.361	-2.3%	65.46	-0.2%	5	16.977	0.613
4 (v)	1.680	82.23	1.406	16.3%	79.95	2.8%	1.845	-9.8%	80.88	1.6%	2	10.034	2.698
5 (h)	1.590	111.59	1.893	-19.1%	108.43	2.8%	1.731	-8.9%	110.58	0.9%	5	30.963	5.025
6 (v)	1.850	140.00	1.553	16.1%	138.82	0.8%	1.382	25.3%	140.01	0.0%	2	8.300	9.375
7 (h)	2.100	179.04	1.927	8.2%	182.40	-1.9%	2.246	-7.0%	184.75	-3.2%	1.25	4.201	7.132
8 (h)	2.030	206.62	1.413	30.4%	224.18	-8.5%	1.851	8.8%	225.92	-9.3%	1.25	29.668	24.120
9 (v)	1.540	267.00	1.551	-0.7%	258.21	3.3%	1.414	8.2%	259.15	2.9%	0.625	5.493	4.905
10 (h)	1.120	282.78	0.682	39.1%	307.97	-8.9%	0.800	28.6%	308.32	-9.0%	0.625	18.481	17.960
h = horizontal mode			Mean:	25.5%	Mean:	3.3%	Mean:	10.8%	Mean:	2.8%	Sum:	217.39	73.58
v = vertical mode											Improvement:		66.2%

Table F.4 The values of the optimized design variables used in simulation cases 4 and 7.

#	Desing Variable	Range min - max	Initial Value	Optimal Value
	Type and Units			
1	Stiffness coefficient [MN/m]	100 - 2500	700	119.74
2	Stiffness coefficient [MN/m]	100 - 2500	700	410.20
3	Damping coefficient [Ns/mm]	1 - 100000	1000	9673.37
4	Damping coefficient [Ns/mm]	1 - 100000	1000	1960.04
5	Stiffness coefficient [MN/m]	60 - 80	70	73.93
6	Damping coefficient [Ns/mm]	1 - 100	5	8.52
7	Damping ratio [%]	0.01 - 10.00	0.50	0.45
8	Damping ratio [%]	0.05 - 20.00	0.50	3.99
9	Damping ratio [%]	0.05 - 20.00	0.50	19.72
10	Damping ratio [%]	0.05 - 20.00	0.50	19.78
11	Damping ratio [%]	0.05 - 20.00	0.50	19.56
12	Damping ratio [%]	0.05 - 20.00	0.50	0.63
13	Damping ratio [%]	0.05 - 20.00	0.50	18.04

ACTA UNIVERSITATIS LAPPEENRANTAENSIS

132. TORKKELI, MARKO. Technology selection and group decision support systems: Case studies on supporting strategic technology selection processes. 2002. U.s. Diss.
133. KYRKI, VILLE. Local and global feature extraction for invariant object recognition. 2002. 115 s. Diss.
134. HEIKKILÄ, TANJA. Permanent magnet synchronous motor for industrial inverter applications- analysis and design. 2002. 109 s. Diss.
135. HUTTUNEN, PENTTI. Data-parallel computation in parallel and distributed environments. 2002. U.s. Diss.
136. LIU, YONG. On sliding mode control of hydraulic servo systems and a manipulator. 2002. U.s. Diss.
137. JUHANTILA, OLLI-PEKKA. Establishing intercompany relationships: Motives and methods for successful collaborative engagement. 2002. 281 s. Diss.
138. PREIS, SERGEI. Practical applications of a systematic approach to the chemical abatement of pollutants in water and air. 2002. 234 s. Diss.
139. TIIHONEN, JARI. Influence of stationary phase and eluent properties on chromatographic separation of carbohydrates. 2002. U.s. Diss.
140. KILKKI, JUHA. Automated formulation of optimisation models for steel beam structures. 2002. 85 s., liitt. Diss.
141. LENSU, LASSE. Photoelectric properties of bacteriorhodopsin films for photosensing and information processing. 2002. 114 s. Diss.
142. KAURANNE, TUOMO. Introducing parallel computers into operational weather forecasting. 2002. U.s. Diss.
143. PUUMALAINEN, KAISU. Global diffusion of innovations in telecommunications: Effects of data aggregation and market environment. 2002. 153 s. Diss.
144. SARRETTE, CHRISTINE. Effect of noncondensable gases on circulation of primary coolant in nuclear power plants in abnormal situations. 2003. 114 s. Diss.
145. SAARENKETO, SAMI. Born globals – internationalization of small and medium-sized knowledge-intensive firms. 2002. 247 s. Diss.
146. IKONEN, KIRSI. Metal surface and subsurface inspection using nondestructive optical methods. 2002. U.s. Diss.
147. OLLIKAINEN, Mikael. Origins of production errors and significance of employee empowerment in reducing production error amount in sheet metal fabricating industry. 2003. 153 s. Diss.
148. KOUVO, PETRI. Formation and control of trace metal emissions in co-firing of biomass, peat and wastes in fluidised bed combustors. 2003. U.s. Diss.
149. MOOSAVI, ALI. Transport properties of multi-phase composite materials. 2003. U.s. Diss.
150. SMOLANDER, KARI. On the role of architecture in systems development. 2003. U.s. Diss.
151. VERENICH, SVETLANA. Wet oxidation of concentrated wastewaters: process combination and reaction kinetic modeling. 2003. U.s. Diss.
152. STÄHLE, PIRJO, STÄHLE, STEN & PÖYHÖNEN, AINO. Analyzing dynamic intellectual capital: System-based theory and application. 2003. 191 s.

153. HAATAJA, JORMA. A comparative performance study of four-pole induction motors and synchronous reluctance motors in variable speed drives. 2003. 135 s. Diss.
154. KURRONEN, PANU. Torque vibration model of axial-flux surface-mounted permanent magnet synchronous machine. 2003. 123 s. Diss.
156. KUIVALAINEN, OLLI. Knowledge-based view of internationalisation – studies on small and medium-sized information and communication technology firms. 2003. U.s. Diss.
157. AHOLA, JERO. Applicability of power-line communications to data transfer of on-line condition monitoring of electrical drives. 2003. 141 s. Diss.
158. 1st Workshop on Applications of Wireless Communications. Edited by Jari Porras, Jouni Ikonen and Pekka Jäppinen. 2003. 67 s.
159. TUUTTI, VEIKKO. Ikkunoiden lasirakenteet ja niiden valintaan vaikuttavat tekijät. 2003. 294 s. Diss.
160. METSÄMUURONEN, SARI. Critical flux and fouling in ultrafiltration of proteins. 2003. U.s. Diss.
161. TUIMALA, JARNO. Aiding the strategic purchasing benchmarking process by decision support systems. 2003. U.s. Diss.
162. SORSA, TIA. The interaction of the calcium sensitiser levosimendan with cardiac troponin C. 2003. U.s. Diss.
163. KOVANEN, JANNE. Improving dynamic characteristics of open-loop controlled log crane. 2003. 97 s. Diss.
164. KURTTILA, HEIKKI. Isentropic exergy and pressure of the shock wave caused by the explosion of a pressure vessel. 2003. 114 s., liitt. Diss.
165. KÄMÄRÄINEN, JONI-KRISTIAN. Feature extraction using Gabor filters. 2003. U.s. Diss.
167. MIELIKÄINEN, JARNO. Lossless compression of hyperspectral images. 2003. U.s. Diss.
168. LI, XIAOYAN. Effect of mechanical and geometric mismatching on fatigue and damage of welded joints. 2003. U.s. Diss.
169. OJANEN, VILLE. R&D performance analysis: case studies on the challenges and promotion of the evaluation and measurement of R&D. 2003. U.s. Diss.
170. PÖLLÄNEN, RIKU. Converter-flux-based current control of voltage source PWM rectifiers – analysis and implementation. 2003. 165 s. Diss.
171. FRANK, LAURI. Mobile communications within the European Union: the role of location in the evolution and forecasting of the diffusion process. 2003. U.s. Diss.
172. KOISTINEN, PETRI. Development and use of organizational memory in close and long-term cooperation between organizations. 2003. 170 s. Diss.
173. HALLIKAS, JUKKA. Managing risk in supplier networks: case studies in inter-firm collaboration. 2003. U.s. Diss.
174. LINDH, TUOMO. On the condition monitoring of induction machines. 2003. 146 s. Diss.
175. NIKKANEN, MARKKU. Railcarrier in intermodal freight transportation network. 2003. 217 s. Diss.
176. HUIKONEN, JANNE. Supply chain integration: studies on linking customer responsiveness and operational efficiency in logistics policy planning. 2004. 151 s. Diss.